FRIEDRICH-SCHILLER-
UNIVERSITÄT
JENA

Towards a relational scalar field correlation function in spin foams

Physikalisch-Astronomische-Fakultät
Arbeit zur Erlangung des akademischen Grades
Master of Science (M.Sc.) in theoretischer Physik

Thesis submitted in accordance with the requirements for the degree
Master of Science (M.Sc.) in theoretical physics

submitted by:
Pedro de Dios Cruz

1st Referee: Prof. Dr. Holger Gies
2nd Referee: Dr. Sebastian Steinhaus (*supervisor*)

Jena, 18.08.2025

1st Referee: Prof. Dr. Holger Gies
2nd Referee: Dr. Sebastian Steinhaus (*supervisor*)

A mis padres

Zusammenfassung

Wir untersuchen die Kopplung eines freien massiven Skalarfeldes an ein eingeschränktes EPRL–FK Spin Foam Modell im semiklassischen Limes. Zur Beschreibung der Materie verwenden wir die Methode *discrete exterior calculus*, um das freie Feld auf irregulären Gittern zu definieren. Zur Beschreibung der Geometrie beschränken wir die Zustandsumme des Spin Foam Modells auf sogenannte *quantum cuboid* intertwiner, was zu einer *superposition* flacher quaderförmiger Gitter mit einer stark reduzierten Anzahl an Freiheitsgraden führt. Dieses Versuchsdesign ermöglicht die Berechnung geometrischer Observablen wie des 4-Volumens des gesamten Systems und der Längenverteilungen. Als Materieobservablen führen wir erstmals eine *relationale* Korrelationsfunktion $\langle\phi\phi(R)\rangle$ ein und werten diese sie aus, sie ist invariant unter Diffeomorphismen, denn sie misst die Korrelationen des Skalarfeldes in Relation zur geodätischen Distanz R. Dazu integrieren wir über alle Realisierungen dieser Distanz R. Diese Definition erfasst somit sowohl die Materiekorrelationen als auch die statistische Wahrscheinlichkeit, mit der bestimmte Distanzen in der Zustandssumme realisiert werden. Monte Carlo Simulationen zeigen, dass sich das gekoppelte System in guter Näherung wie ein Skalarfeld auf einem effektiven regulären Gitter mit dynamischer Gitterkonstante verhält, während $\langle\phi\phi(R)\rangle$ einen charakteristischen Abfall mit R aufweist, der sowohl durch die Felddynamik als auch durch die Geometriestatistik geprägt ist.

Um das Verständnis der *relationalen* Korrelationsfunktion zu vertiefen, entwickeln wir ein eindimensionales *Toy Model* in Form eines freien massiven Skalarfeldes auf einem unregelmäßigen, dynamischen Gitter. Darin führen wir explizite Auswertungen geometrischer Observablen und der vorgeschlagenen *relationalen* Korrelationsfunktion durch. Zudem testen wir die Methode des Importance Sampling zur Auswertung des Systems. In diesem *Toy Model* rekonstruieren wir die skalare Zweipunkt-Korrelationsfunktion der bekannten Gitterfeldtheorie aus unserer *relationalen* Korrelationsfunktion im Limes konstanter Gitterabstände. Darüber hinaus zeigen wir, dass beide numerischen Ansätze, explizite Auswertungen und Importance Sampling, zu ähnlichen Ergebnissen führen.

Unsere Ergebnisse und Methoden belegen die Anwendbarkeit *relationaler* Observablen über ihre rein formale Definition hinaus als diffeomorphismusinvariante Größen in hintergrundunabhängigen Szenarien. Die Auswertungen und die Konsistenz dieser *relationalen* Observablen eröffnen den Weg zur Untersuchung ähnlicher Größen in allgemeineren, materiegekoppelten Spin Foam Modellen mit allgemeineren und höherdimensionalen Geometrien.

Abstract

We investigate the coupling of a free massive scalar field to a restricted EPRL–FK spin foam model in the semiclassical limit. On the matter side, we use discrete exterior calculus to define the free field on irregular lattices. On the geometric side, we restrict the spin foam state sum to quantum cuboid intertwiners, yielding a superposition of flat hypercuboidal lattices with greatly reduced degrees of freedom. This setup enables the computation of geometric observables such as the total 4-volume and length distributions. As matter observable, we introduce, and evaluate for the first time, a *relational* correlation function $\langle\phi\phi(R)\rangle$, a diffeomorphism-invariant object that measures the scalar field correlations in *relation* to the geodesic distance R, by integration over all possible realizations of R. As a result, this definition captures both matter correlations and the statistical likelihood of distances being realized in the partition function. Monte Carlo simulations reveal that the coupled system closely follows the behavior of a scalar field on an effective regular lattice with a dynamical spacing, while $\langle\phi\phi(R)\rangle$ displays a distinctive decay with R, shaped by both field dynamics and geometry statistics. To deepen our understanding of the *relational* correlation function, we develop a one-dimensional *toy model* as a free massive scalar field defined on an irregular, dynamical lattice, where we perform explicit evaluations of geometric observables and the proposed *relational* correlation function. In addition, we test the importance sampling method to evaluate the system. In this toy model, we recover the two-point correlation function from our *relational* correlation function in the limit of constant lattice spacing. Additionally, we show that both numerical methods, explicit evaluations and importance sampling yield similar results.

Our results and methods demonstrate the viability of *relational* observables beyond a pure formal definition as a diffeomorphism-invariant object in background-independent settings. The evaluations and consistency of this *relational* observable open the path to study similar objects in more general matter-coupled spin foam models with richer geometries and higher-dimensional extensions.

Acknowledgements

First and foremost, I wish to express my deepest gratitude to Dr. Sebastian Steinhaus for his diligent guidance throughout this work, and during the extensive working sessions that shaped much of this thesis. His devotion and commitment to his research endeavors created an inspiring environment that allowed me to sharpen my skills and refine my scientific thinking growth that would not have been possible otherwise. I am also sincerely grateful to Prof. Dr. Holger Gies for his support during my time in this Master's program in Jena, and for supervising this work. My thanks also go to Dr. Seth Asante and Dr. José Diogo de Figueiredo for the enlightening discussions that deepened my understanding of spin foam models. Special thanks to Kevin Rudolf Siebert for helping me set up the Draco cluster environment, where the simulations for this work were carried out, and to Malte Benjamin Arps for his expertise in optimizing Julia numerical codes and for his crucial suggestions on properly binning data in the importance sampling procedure. I am equally thankful to Björn Borgolte for his comments on the formatting of this thesis. I am indebted to Dr. Jose Antonio Zapata for first introducing me to spin foam models and the quantum gravity community.

As no one lives by dreams alone, I owe heartfelt thanks to my parents, Elena and Pedro, for their unconditional support in all my goals. Without their love and belief in me, this journey in a foreign land would never have been possible. I am equally grateful to my brothers, Jose Manuel and Juan Pablo, for always trusting in me and their continuous encouragement.

Last but not least, I would like to thank my friends, Jose Medina and Fabian Obert, for making me feel at home in a new land. Finally, to Natalia Ferrari, for sharing long hours of study in the library and keeping my heart warm. Thank you all.

Contents

Introduction

In our current understanding of physics, the fundamental forces governing all interactions in nature are the electromagnetic, weak, strong, and gravitational forces. Although quantum theory (QT) has successfully described the first three, incorporating gravity into this framework remains a profound challenge. These difficulties arise primarily from two fronts. Experimentally, the absence of observations where quantum gravitational effects are dominant makes difficult to identify new physical principles that could guide theory development in this regime. Conceptually, the challenge stems from the contrasting foundations of the underlying theories: General Relativity (GR) and QT. QT is formulated on a fixed, non-dynamical background where space and time act as mere parameters, whereas GR describes gravity as a smooth, deterministic dynamical field encoded in the Riemannian geometry of spacetime. Yet, QT demands that all dynamical fields be quantized. Moreover, QT reveals that the fundamental properties of these fields are governed by probabilistic laws.
Early attempts to quantize GR using conventional field theory methods revealed its non-renormalizability, manifesting the need for new approaches. In this context, contemporary efforts to develop a quantum theory of gravity are guided by the robust mathematical structures of both GR and QT, which are believed to be closely connected at the Planck scale [1] (Planck length $\sim 10^{-35}$ m; Planck energy $\sim 10^{28}$ eV).

Although the regimes in which quantum gravity is expected to be applicable are beyond the reach of conceivable experimental exploration, there are compelling theoretical reasons to pursue a compatible framework for both theories. For instance, classical GR predicts the existence of singularities in realistic physical scenarios, such as those involving black holes and cosmology. Near such spacetime singularities, the classical description of gravitational degrees of freedom breaks down, as the curvature of spacetime diverges to infinity. These scenarios highlight the need for a theory of quantum gravity that addresses questions related to the resolution of such singularities and potential information paradoxes [2], in which the classical description fails to provide answers to these phenomena. Furthermore, at the classical level, the dynamics of gravity and matter are deeply intertwined, suggesting a similar complexity in the quantum

regime. Thus, a quantum understanding of gravity could elucidate the nature of matter at the Planck scale and its connection to observable physics, including a deeper understanding of elementary particles and related open issues such as the hierarchy problem [3], the cosmological constant problem [4], or a deeper understanding of renormalization [5] in Quantum Field Theories (QFT). Understanding the mutual influence between quantum matter and gravity is also central to many quantum gravity programs, as their interplay could yield novel phenomena. For instance, in the Asymptotic Safety scenario [6], indications suggest that the quantum consistency of the theory may impose constraints on the allowed matter content, potentially affecting the existence of a UV fixed point [7]. Therefore, all approaches to quantum gravity must incorporate matter in a consistent framework.

Numerous approaches to quantizing gravity have been proposed in the past [8], each guided by different physical principles. Among these, spin foams are a manifestly non-perturbative approach which assigns probability amplitudes to quantum geometries. In modern formulations, spin foam models originate from the Plebanski-Holst formulation of general relativity [9], which recasts gravity as a constrained topological BF theory [10]. Since four-dimensional gravity is not topological, the so-called *simplicity constraints* are introduced to incorporate local degrees of freedom. The spin foam approach seeks to give meaning to the formal partition function of this constrained BF theory by introducing a lattice regulator: the continuum spacetime is replaced by a triangulation, truncating the degrees of freedom. The dual 2-complex of this triangulation (composed of vertices v, edges e, and faces f) is then eventually *colored* with group-theoretic data: each face f carries an irreducible representation ρ_f of the symmetry group, and each edge e carries an intertwiner i_e. Imposing the simplicity constraints at the quantum level restricts the allowed representation labels, with different implementations leading to distinct models [11]. Among these, the EPRL–FK model [12, 13, 14] is one of the most studied. This model enforces a linear version of the simplicity constraints on simplicial triangulations, and its boundary states connect to loop quantum gravity spin networks via projected spin network techniques [15, 16]. Additionally, the semiclassical limit of this model has also been extensively investigated [17].

Spin foam models were originally conceived to describe pure gravity in the quantum regime, in the absence of any gauge or matter fields. Therefore, the EPRL-FK model lacks a treatment of the matter sector. Understanding this coupling is essential in these models, as it may significantly impact the classical limit of the theory, which is not yet completely understood [18]. Moreover, this coupling is crucial for distinguishing between the various conceivable spin foam models [11].This aspect of the theory has barely been explored, as there is currently no

clear strategy to quantize a full model of quantum gravity coupled to matter. Indeed, quantizing pure gravity has been a daunting task. In the case of spin foam models, one of the difficulties lies in computing their fundamental amplitudes. While there has been progress in understanding a single vertex amplitude [19] [20] [21], very little is known about the behavior of the entire path integral. Currently, amplitude computations mainly rely on semi-classical approximations for which closed expressions are manageable. Nonetheless, these computations are still expensive, as convergence requires summing over a large set of variables, causing the computational complexity to grow exponentially. As a result, these computations require significant computational resources, such as high-performance computing, for their evaluation.

Different scenarios for including matter have been explored in spin foams. For instance, unification scenarios in which a large symmetry group encodes both gravity and matter [22] have been explored. Other approaches have explored scenarios in which matter degrees of freedom are used to deparameterize the system at the classical level and then perform the quantization of the full system [23, 24, 25, 26]. More direct proposals have also been considered, such as adding matter fields "on top" of the pure quantum gravity theory. The main idea in these studies is to employ the geometry encoded in a spin foam as the spacetime on which matter degrees of freedom and their interactions are defined. These models include studies of gauge fields [27, 28, 29, 30], fermions [31, 32], and scalar fields [33]. A primary motivation behind these studies is to develop models that are accessible for investigation in regimes where an effective theory can be recovered and understood as a quantum field defined on a fixed background geometry, thereby providing a consistency check.

Within this framework, the goal of the present thesis is to explore a matter coupling in spin foam models. We focus on a simplified, yet sufficiently rich, system: a free quantum scalar field coupled to a restricted semiclassical spin foam model. On the geometric side, the EPRL-FK state sum is restricted to a particular set of intertwiners, namely, *quantum cuboid* intertwiners [34]. This restriction yields a superposition of flat, hypercuboidal lattices weighted by spin foam amplitudes. The resulting model has far fewer degrees of freedom and substantial symmetry, making the state sum significantly more tractable. On the matter side, the scalar field is then treated as a lattice field theory [35] defined on a cuboid spin foam geometry. Using discrete exterior calculus [36, 37, 38], the field couples minimally[1] to the geometry: the spin foam amplitudes remain unaffected, while the field dynamics depend only on the underlying geometry. As a result, this setup is accessible for numerical simulations and its amplitude can be computed in the semiclassical regime.

[1] As defined in [36].

The model enables the study of both geometric and matter observables. Geometric quantities include the total 4-volume V and edge lengths l_i. The observables of the matter sector are at the core of this work. Given that the two-point correlation function from the lattice field theory function lacks a meaningful interpretation in a background independent setting, we instead propose and evaluate, for the first time, a *relational* correlation function $\langle\phi\phi(R)\rangle$, where R is the geodesic distance between any two points. Thus, our relational correlation function is defined in the same spirit as relational observables [39, 40, 41, 42] and offers a diffeomorphism invariant interpretation.

Given the non-oscillatory nature of the amplitude of the coupled system in the semiclassical limit, we can employ a Markov Chain Monte Carlo algorithm to evaluate the system. In this approach, Monte Carlo integration approximates expectation values by the sample means of fields and lengths generated as random variables [43], allowing us to compute all the observables discussed above.

To further probe the properties of the proposed relational correlation function, we also investigate a simplified *toy model*: a free massive scalar field defined on a one-dimensional irregular, dynamical lattice. This setup mirrors the coupled system of a scalar field interacting with our restricted spin foam model in the semiclassical regime, but with drastically reduced number of degrees of freedom. The simplifications turn the *toy model* into a computational laboratory where we can better understand our proposed observable, and where explicit evaluations are feasible. In addition, alternative numerical strategies, such as importance sampling, can be systematically tested. Thus, this framework enables a detailed study of both geometric and matter observables and, in particular, offers a clearer interpretation of the relational correlation function introduced in this work.

The structure of this work is as follows: Chapter 1 introduces the discrete exterior calculus framework used to define a free massive scalar field on irregular lattices. Chapter 2 presents the restricted EPRL-FK spin foam model with quantum cuboid intertwiners and derives its semiclassical amplitude. Chapter 3 describes the coupling between this restricted spin foam model and the free massive scalar field, including the numerical evaluation of geometric and matter observables. Chapter 4 introduces a simplified *toy model*, a free massive scalar field defined on an irregular, dynamical lattice, and examines its geometric and matter expectation values. Next, the Conclusions and Outlook section contains insights for future research. The Appendix contains four sections. The first one gives a brief review of intertwiners, as mathematical tools that take part in spin foams models. The second, third and forth sections, contain plots of the two-point correlation function, distribution of R and the *relational* correlation function, respectively.

Chapter 1

Free Field on Irregular Settings

This chapter aims to give a short review of the free quantum field defined on the continuum and the subsequent discrete description defined as a lattice field theory. In a next step, we review the discrete exterior calculus tools that will allow us to define the free field action on general discrete settings. This in turn will serve to describe the matter sector on our restricted spin foam model (introduced later on this work) coupled to a free scalar field.

1.1 Lattice field theory

Lattice quantum field theories (LQFT) are fundamentally quantum field theories which are not defined on the continuum spacetime, but rather in a finite discrete volume on a set of points that discretize space-time [35]. In this sense, LQFT can be taken in a precise manner as an approximation of the ordinary continuum version. Thus, the finite number of degrees of freedom makes LQFT an optimal test scenario for computing quantities of interest in particle physics, like expectation values, mass spectra, correlation functions, etc. [44]. This constitutes one of the main reasons to employ LQFT techniques on this project, as it is possible to define a discretized version of matter fields akin to how models of quantum gravity such as spin foams are defined on discretized settings like a triangulation, which serves as a regulator of the underlying manifold. Thus, fields defined on similar settings can be coupled[1] to spin foam models. Furthermore, under further assumptions (which will be fully covered in next chapters), this coupling can be accessible to numerical evaluations.

[1] Although this could be also done in different approaches [27, 28, 30, 31, 33], not necessarily in the same way as it will be presented in this work.

1.2 Free field on the continuum

As an introduction to lattice field theory, we start by briefly reviewing the free, massive scalar field defined in the continuum. We start from the Euclidean (Wick-rotated) action:

$$S[\phi] = \int d^4x \left(\frac{1}{2}(\partial_\mu \phi)(\partial^\mu \phi) + \frac{M^2}{2}\phi^2 \right) \quad , \tag{1.1}$$

where M is the mass of the field. We define the partition function as:

$$Z = \int \mathcal{D}\,\phi\, e^{-S[\phi]} \quad . \tag{1.2}$$

The expression for the n-point correlation functions is then given by:

$$\langle \phi(x_1) \dots \phi(x_n) \rangle = \int \mathcal{D}\phi\, \phi(x_1) \dots \phi(x_n)\, e^{-S[\phi]} \quad . \tag{1.3}$$

The case $n = 2$ is of particular interest for this project, as it defines the two-point correlation function. For the free field theory, all n-point correlation functions can be completely constructed from the two-point function using Wick's theorem. The two-point correlation function is defined as:

$$\langle \phi(x_1)\phi(x_2) \rangle = \int \mathcal{D}\phi\, \phi(x_1)\phi(x_2)\, e^{-S[\phi]} \quad . \tag{1.4}$$

The two-point correlation function of the scalar field decays exponentially with the distance $d(x_1, x_2)$, where $d(x_1, x_2)$ represents the distance between points with coordinates x_1 and x_2, i.e., $\langle \phi(x_1)\phi(x_2) \rangle \sim \exp(-\frac{d(x_1,x_2)}{\xi})$, where ξ denotes the correlation length [45]. For the massive scalar field, this correlation length is inversely proportional to the mass M of the scalar field, $\xi = \frac{1}{M}$, i.e., the larger the mass, the faster the correlations die off as distance increases. Conversely, it is possible to estimate the mass of the scalar field from the exponential decay of its correlations.

However, in the present work, expression (1.4) deserves more attention. In conventional field theories, correlation functions like (1.4) explicitly depend on coordinate labels, as for practical applications field theories are typically defined on a fixed background. In this context, coordinate labels represent points on the manifold of a specific spacetime, often the Minkowski spacetime. Although (1.4) is well-defined in this framework, complications arise in more general scenarios involving the dynamics of spacetimes itself, such as in quantum gravity models,

where the background spacetime is no longer fixed (as in spin foam models). In such scenarios, it makes little sense to talk about the behavior of $\langle\phi(x_1)\phi(x_2)\rangle$ as function of the *coordinate* distance $d(x_1, x_2)$, as this would just tell us how the fields are correlated at coordinates x_1 and x_2. Furthermore, since (1.4) is related to a physical observable, it should be in general a diffeomorphism-invariant quantity, which (1.4) is not. As, expected, defining such quantities rigorously taking into account these observations is a challenging task [42, 41, 39], nonetheless correlation functions (and any physical observable) should be then defined in a more precise way in broader contexts where the background spacetime is not fixed. Therefore, the goal of this present work is to take a step in this direction, where the definition of meaningful observables is central to our exploration. As mentioned in the introductory section, we will postpone the discussion on the definition of meaningful observables to Chapter 4, where we further investigate a more suitable expression for correlation functions defined without a fixed spacetime that also offers a diffeomorphism-invariant interpretation.

1.3 Free field on the lattice

We now move to the description of the discretized version of the free field defined on a hypercubic (regular) lattice with periodic boundary conditions and lattice spacing a. In the lattice, the continuum scalar field $\phi(x)$ is replaced by the field ϕ_x located at the coordinates x of the vertices of the regular lattice. Derivatives are replaced by their approximation as the difference of fields sharing the same edges. However, this definition is not unique, as derivatives can be approximated by forward, backward, and midpoint differences. Although in the limit $a \to 0$ all approximations are equivalent, they may introduce discretization artifacts of order $\mathcal{O}(a)$. To circumvent this issue, we consider the unique Laplacian [37] (by performing an integration by parts and dropping boundary terms due to periodic boundary conditions):

$$\partial^2\phi \to \sum_{\pm\mu} \frac{\phi(x + a\, e_\mu) + \phi(x - a\, e_\mu) - 2\phi(x)}{a^2} \quad , \tag{1.5}$$

where in $4D$, μ runs from 1 to 4 (in the Euclidean case) and e_u denotes a unit vector in direction μ. $\pm\mu$ implies a sum over all positive and negative directions.
Likewise, in 4D, an integral as a Riemann sum takes the form:

$$\int d^4\phi(x) \to a^4 \sum_x \phi_x \quad , \tag{1.6}$$

and functional integrals become a product of normal integrals:

$$\int \mathcal{D}(x) \to \prod_x \int d\phi_x \quad , \tag{1.7}$$

where x is just a counting variable in this context.
Using these prescriptions, the discretized scalar field action (in 4D) on a regular hypercubic lattice becomes:

$$S^{(d)}[\phi] = -\frac{a^2}{2} \sum_{x,\mu} \phi_x \phi_{x+\mu} + \frac{a^2}{2}(8 + a^2 M^2) \sum_x \phi_x^2 \quad , \tag{1.8}$$

where we have used the periodicity of the lattice to rewrite the kinetic part of the action. This action can be written in a compact form by enumarating the vertices of the lattice by a single master index n, defined in $4D$ as:

$$n = x_1 + N_1 + N_1 N_2 x_3 + N_1 N_2 N_3 x_4 \quad , \tag{1.9}$$

where N_i are the number of vertices in each dimension, and $N = \prod_{i=1}^{4} N_i$. In this way ϕ_n represents the value of the field at the vertex n and we can write all values of the field in the lattice as an N-dimensional vector $\vec{\phi}$. Then, the action of the scalar field can be expressed as the contraction of a matrix K by two vectors of field configurations:

$$S^{(d)}[\phi] = \frac{1}{2} \phi_n K_{nm} \phi_m \ , \tag{1.10}$$

$$K_{nm} = -a^2 \sum_\mu (\delta_{n+e_\mu,m} + \delta_{n-e_\mu,m} - 2\delta_{n,m}) + a^4 M^2 \delta_{nm} \quad , \tag{1.11}$$

where repeated indices indicate a summation. Furthermore, the 2-point correlation can be computed explicitly, following (1.4):

$$\langle \phi_i \phi_j \rangle = \int \prod_k d\phi_k \, \phi_i \phi_j \, e^{-\frac{1}{2}\phi_n K_{nm} \phi_m} \quad . \tag{1.12}$$

Performing a multi-dimensional Gaussian integration on the above expression reduces the two-point correlation to simply:

$$\langle \phi_n \phi_m \rangle = K^{-1}_{nm} \quad . \tag{1.13}$$

The matrix K then plays a main role, as all the information about the two-point correlations of the free field on the lattice is contained in this object.

1.3.1 Taking the continuum limit

For the free, massive scalar field, the continuum limit is easy to obtain. In this system, the lattice spacing a determines the dimension of analytical operations, so it is possible to rescale to dimensionful quantities employing powers of a. This turns both the fields and coupling constants into dimensionless quantities. In 4D, we can define the dimensionless fields $\varphi = \frac{\phi}{a}$, and the scalar field action is written then in terms of a new matrix $\tilde{K}$:

$$S^{(d)}[\phi] = \frac{1}{2}\varphi_n \tilde{K}_{nm}\varphi_m \quad , \tag{1.14}$$

$$\tilde{K}_{nm} = -\sum_{\mu}(\delta_{n+e_\mu,m} + \delta_{n-e_\mu,m} - 2\delta_{n,m}) + \tilde{M}^2\delta_{nm} \quad , \tag{1.15}$$

where we have defined the lattice mass $\tilde{M}(a) = aM$. Thus, the scalar field action only contains a dependence on the lattice mass $\tilde{M}$, showing explicitly that this action is independent of the lattice spacing a. Taking the continuum limit corresponds to taking the lattice mass $\tilde{M} \to 0$, while keeping $M = \frac{\tilde{M}}{a}$ constant. As $\tilde{M} \to 0$, the correlation length (in units of a) diverges; therefore, one can take the continuum limit trivially, recovering the continuum action (1.1) while showing that the massive scalar field theory has only one free parameter, the mass M of the scalar field. Hence, this theory is a suitable test case for coupling matter to our discrete approach to quantum gravity.

1.4 Discrete exterior calculus

As previously mentioned at the beginning of this chapter, one of our goals in this work is to define the free field theory within a discrete framework similar to that used in spin foam models. This approach will provide a direct path[2] to couple both theories. In spin foam models it is customary to discretize the spacetime manifold via a triangulation[3]. In particular, for the present project we will explore (in subsequent chapters) a spin foam model defined over a cubilation. It is here that the techniques of discrete exterior calculus come in handy to our aforementioned goal. In standard exterior calculus [47] the concepts of p-forms (and their duals), exterior derivatives and operators such as the gradient, divergence and Laplacians are well known quantities. Consequently, we can write the action (1.1) in this language and

[2] Our approach will be thoroughly discussed in subsequent chapters.

[3] Although, spin foam models can be also defined in a general cellular complex [46].

subsequently apply the discrete version of the exterior calculus objects to define the action over general discretizations. Therefore, in this section we will first review the discrete exterior calculus techniques, primarily following the presentation in [37, 48, 38]. In a nutshell, in the discrete framework, the main building blocks are p-forms, which must now be smeared over p-simplices, where a p-simplex[4] is the convex hull of $p+1$ affinely independent points (vertices) in $\mathbb{R}^n$. Following this prescription will allow us, in turn, to construct the rest of the exterior calculus objects.

We start then by writing (1.1) in the exterior calculus language: On a manifold $\mathcal{M}$ a real scalar field ϕ with mass M is a 0-form ($\phi \in \Omega^0(\mathcal{M})$), then the action for the free field on the continuum can be written as:

$$S = \frac{1}{2}\int_{\mathcal{M}} d\phi \wedge *d\phi + M^2\phi * \phi \quad , \tag{1.16}$$

where $d\phi$ is the exterior derivative of ϕ and $*$ denotes the Hodge dual. The goal is then to rewrite the above action in a general discretized setting. Therefore, we need to introduce the concepts of discretized p-forms and their duals $(d-p)$-forms, as well as the discrete analog of exterior derivatives.

1.4.1 Exterior forms on simplicial complexes

To start with the review of the discrete exterior calculus, we need to define a discrete setting. Usually, this is defined as a finite abstract simplicial complex [49]. A finite abstract simplicial complex K (in the following, *simplicial complex* for short) is a multiset of ordered subsets σ of the set of vertices $K_0 = \{v_1, v_2, \ldots, v_{N_0}\}$ such that if $\sigma \in K$ and $\sigma' \subset \sigma$, also $\sigma' \in K$ [37]. In general, $\sigma' \subset \sigma$ is called a face of σ. All subsets of cardinality $p+1$ are called p-simplices $\sigma_p \in K_p$ and the dimension d of K is defined as the maximal cardinality of simplices in K. Thus, K consists of 0-simplices to d-simplices, $K = \bigcup_{p=0}^{d} K_p$, and is also referred as a simplicial d-complex. The ordering of the sets $\sigma_p = (v_{i_1}, \ldots, v_{i_p}) =: (i_1 \ldots i_p)$ defines an orientation on the complex.

In addition, for the rest of this review, we will work with simplicial manifolds. Thus, we briefly outline the fundamental properties of these structures: a finite abstract simplicial d-manifold is defined as a finite abstract simplicial d-complex that satisfies the following properties: it is *non-branching*. That is, each $(d-1)$-simplex is face of exactly two d-simplices (unless it is on the boundary). In addition, a finite abstract simplicial pseudo d-manifold is *strongly connected*, this means that any two d-simplices have a strong chain of d-simplices neighboring pairwise

[4]Formally, a p-simplex σ_p can be defined as: $\sigma_p = \{\sum_{i=0}^{p} \lambda_i v_i \mid \sum_{i=0}^{p} \lambda_i = 1,\ \lambda_i \geq 0\}$ where $v_0, v_1, \ldots, v_p$ are the vertices of the simplex, and λ_i are non-negative coefficients . p is called the dimension of the simplex [48].

by $(d-1)$-faces. Lastly, our simplicial complex should satisfy *dimensional homogeneity*, which means that every simplex is the face of some d-simplex. These conditions ensure that our simplicial complex is locally homemorphic to $\mathbb{R}^n$.

Returning to our simplicial complex K, we define *p-chains* as formal linear combinations of p-simplices. These generate a finite-dimensional vector space, denoted by $C_p(K)$. A generic p-chain is represented by $c \in C_p(K)$. Introducing a bra-ket notation, a p-chain can be written as:

$$|c\rangle = \sum_{\sigma_p \in K_p} c_{\sigma_p} |\sigma_p\rangle = \sum_{\sigma_p \in K_p} \langle \sigma_p | c \rangle |\sigma_p\rangle \quad .$$

Accordingly, linear forms on chains are called p-cochains $\tilde{c} \in C^p(K)$. A cochain $\tilde{c}$ can can be expanded in the dual basis $\{\langle \sigma_p |\}$, defined by the pairing $\langle \sigma_p | \sigma'_p \rangle = \delta_{\sigma\sigma'}$. The cochain $\tilde{c}$ dual to c can be written as the bra:

$$\langle \tilde{c}| \equiv \langle c| = \sum_{\sigma_p \in K_p} c^*_{\sigma_p} \langle \sigma_p| = \sum_{\sigma_p \in K_p} \langle c|\sigma_p\rangle \langle \sigma_p| \quad .$$

Therefore, there exists a natural duality between chains and cochains on the simplicial complex K [49].

Consider now a finite triangulation of a Riemannian manifold (M, g) with combinatorial structure K, then the p-cochains can be naturally interpreted as discretized p-forms $\omega \in \Omega^p(K) \cong C_p(K)$ by smearing the continuous form $\omega_{\text{cont}} \in \Omega^p(M)$ over p-surfaces $S \subset |K| \subset M$ represented by chains $|S\rangle = \sum_i V_{\sigma_i^p} |\sigma_i^p\rangle \in C_p(K)$ in the triangulation [48] :

$$\omega(S) := \langle \omega | S \rangle = \sum_i V_{\sigma_p^i} \langle \omega | \sigma_p^i \rangle = \sum_i \int_{\sigma_p^i} \omega_{\text{cont}} \quad ,$$

where V_{σ_p} denotes the p-volume of σ_p in $|K|$. In particular, for the surface of a single p-simplex σ_p represented by $V_{\sigma_p}|\sigma_p\rangle$, we obtain:

$$\omega(\sigma_p) = V_{\sigma_p} \langle \omega | \sigma_p \rangle = V_{\sigma_p} \phi_{\sigma_p} = \int_{\sigma_p} \omega_{\text{cont}} \quad ,$$

therefore, the coefficient ω_{σ_p} has the interpretation as the averaged field value of ω_{cont} over σ_p. With this definition, the scalar field can be discretized by smearing it on 0-simplices (σ_0) as:

$$\phi(\sigma_0) := \langle \phi | \sigma_0 \rangle = \phi_{\sigma_0} \quad ,$$

where the vertex volumes are assumed to be trivial in the last equality and the coefficients ϕ_{σ_0} are the discrete components of the field.

1.4.2 Discrete Hodge duality

Equation (1.16) makes use of the Hodge duality in the continuum. Here, we briefly review the main properties of this duality. On a continuum Riemannian manifold (M, g) the Hodge duality maps p–forms $\omega \in \Omega^p(M)$ to $(d-p)$–forms $*\omega \in \Omega^{d-p}(M)$ [50],

$$\omega = \omega_{i_1 \dots i_p} dx^{i_1} \wedge \dots \wedge dx^{i_p} \quad \longleftrightarrow \quad *\omega = (*\omega)_{i_{p+1} \dots i_d} dx^{i_{p+1}} \wedge \dots \wedge dx^{i_d} \quad , \tag{1.17}$$

with coefficients:

$$\omega_{i_1 \dots i_p} \quad \longleftrightarrow \quad (*\omega)_{i_{p+1} \dots i_d} = \frac{\sqrt{g}}{d!} \epsilon_{i_1 \dots i_d} g^{i_1 j_1} \dots g^{i_p j_p} \omega_{j_1 \dots j_p} \quad . \tag{1.18}$$

This duality holds in general up to a sign $**\omega = (-1)^{p(d-p)}\omega$. The hodge dual also allows us to define a natural inner product of p-forms as an integration over a manifold $\mathcal{M}$ by pairing a form (ω) and a dual form (μ) :

$$(\omega, \mu) = \int_{\mathcal{M}} \omega \wedge *\mu = \int_{\mathcal{M}} (\omega_{i_1 \dots i_p})_x [*(\mu)_{i_{p+1} \dots i_d}]_x \sqrt{g_x}\, dx^{i_1} \wedge \dots \wedge dx^{i_d} \quad , \tag{1.19}$$

so, the action (1.16) can be written as:

$$S_D = \frac{1}{2} \left[(d\phi, d\phi) + M^2(\phi, \phi) \right] , \tag{1.20}$$

which gives us a hint on how to rewrite the above action on a discrete setting.

We now turn to the description of the discrete Hodge dual. To understand this duality in the discrete, we first need to introduce the concept of the combinatorial *dual complex*, as this will provide the scenario in which the discrete dual forms habit: in a simplicial d-manifold K, we can naturally define a combinatorial dual complex $\star K$ consisting of $(d-p)$-cells $\star\sigma_p$ dual to the primal p-simplices σ_p, with orientation induced from the orientation of K and cellular structure induced by the adjacency relations of K. The latter means that $\star\sigma \subset \star\sigma'$ if, and only if, $\sigma' \subset \sigma$. Then, $\star K$ can be given as a multiset over its vertex set too.

The duality between the primal and dual simplicial complexes induces a duality between the chains of the primal ($c \in C_p(K)$) and dual complexes ($\star c \in C_p(\star K)$) (as well as the co-chains of primal and dual complexes). These dualities read in Dirac notation:

$$|c\rangle = \sum_{\sigma_p \in K} c_{\sigma_p} |\sigma_p\rangle \quad \overset{\star}{\longleftrightarrow} \quad \langle \star c| = \sum_{\sigma_p \in K} c^{\star}_{\sigma_p} \langle \star \sigma_p| \quad .$$

This duality holds only up to a sign due to the relative orientations of the complexes:

$$\star^2 = (-1)^{p(d-p)} \quad . \tag{1.21}$$

Analogously, the duality also holds between primal and dual cochains.

Here, a notable observation can be made: The Hodge dual (1.17) maps p-forms $\omega \in \Omega^p(M)$ to $(d-p)$-forms $*\omega \in \Omega^{d-p}(M)$. A similar relationship is established in the discrete case between p-forms defined on p-simplices and $(d-p)$-forms, which cannot exist on p-simplices but only on $(d-p)$-cells. Therefore, we can naturally establish a discrete Hodge dual of a p-form $\phi \in \Omega^p(K)$ with the help of the dual complex, where $(d-p)$-cells $\star\sigma_p$ are dual to the primal p-simplices σ_p. These observations can be summarized in the following duality:

$$*\omega := \star\omega \in *\Omega^p(K) \cong \Omega^{d-p}(\star K) \cong C^{d-p}(\star K) \quad .$$

From these dualities, at the level of coefficients the defining condition for the discrete Hodge duality is the equality of the averaged field values:

$$(*\omega)_{\star\sigma_p} := \omega^*_{\sigma_p} \quad , \tag{1.22}$$

where * indicates complex conjugation. With the bra-ket convention:

$$\langle \star\sigma_p | \omega \rangle = *\omega_{\star\sigma_p} \quad , \tag{1.23}$$

or equivalently expressed as:

$$\langle \star\sigma_p | \omega \rangle = \langle \omega | \sigma_p \rangle^* . \tag{1.24}$$

Analogously, in the case of triangulations, we can represent the coefficients of dual fields $*\omega$ as smeared fields:

$$*\omega(\star\sigma_p) = V_{\star\sigma_p}(*\omega)_{\star\sigma_p} = \int_{\hat{\sigma}_{d-p}} *\omega_{\text{cont}} \quad . \tag{1.25}$$

These definitions allow us to interpret the Hodge duality in two different perspectives. On one hand ω is defined as a p-form $\langle\omega|$ on the primal complex. On the other hand $|\omega\rangle$ defined as a $(d-p)$-form on the dual complex, reflecting the freedom in choosing either the primal or dual complex for defining forms in the discrete.

It is important to note that (1.25) makes use of the dual volumes $V_{\star\sigma_p}(*\omega)$ which are typically not uniquely defined. Firstly, if K has a geometric realization[5] $|K|$ in terms of a (topological) simplicial complex over a metric space, then the volumes of the primal complex can be induced from this realization. However, dual volumes depend on how the dual complex is realized, i.e. how it is constructed from the primal complex. The most popular choices are circumcentric and barycentric dual complex [48, 51]. For instance, later in this work we will work with a cubilation. In this simple case, the dual complex is defined as a shifted complex of the primal cubilation, for instance by defining the edges of the dual complex as the average of two consecutive edges of the primal one.

With a well-defined meaning of the discrete Hodge dual, we can define as well an inner product as in the continuum case:

$$\langle\omega|\mu\rangle := \sum_{\sigma_p} V^{(d)}_{\sigma_p} \omega_{\sigma_p} \mu^*_{\star\sigma_p} = \langle\omega| \sum_{\sigma_p} V^{(d)}_{\sigma_p} |\sigma_p\rangle\langle\star\sigma_p|\mu\rangle \quad , \tag{1.26}$$

where we have introduced a resolution of the identity:

$$\sum_{\sigma_p} V^{(d)}_{\sigma_p} |\sigma_p\rangle\langle\star\sigma_p| = \mathbb{1} \quad . \tag{1.27}$$

Finally, with all definitions from above, we can identify primal chains with dual cochains and dual chains with primal cochains:

$$|\sigma_p\rangle \equiv |\star\,\sigma_p\rangle, \qquad \langle\sigma_p| \equiv \langle\star\sigma_p| \ . \tag{1.28}$$

We can define then a complete orthonormal basis (normed to the inverse volume factors):

[5] this refers to the embedding of the simplicial complex on some geometric space like $\mathbb{R}^n$ preserving the topological properties of the simplicial complex.

$$\langle \sigma_p | \sigma'_p \rangle = \frac{1}{V^{(d)}_{\sigma_p}} \delta_{\sigma\sigma'}, \qquad \sum_{\sigma_p} V^{(d)}_{\sigma_p} |\sigma_p\rangle\langle\sigma_p| = \mathbb{1} \quad , \tag{1.29}$$

with these identifications, it is straightforward to rewrite the Hodge dual (1.22) as follows:

$$\langle *\omega | \sigma_p \rangle := \langle \star\sigma_p | \omega \rangle \equiv \langle \sigma_p | \omega \rangle = \langle \omega | \sigma_p \rangle^* \quad . \tag{1.30}$$

For the case of kets, we need to include accordingly the sign (1.21):

$$\langle \sigma_p | * \omega \rangle := \langle \omega | \star \star \sigma_p \rangle = (-1)^{p(d-p)} \langle \omega | \sigma_p \rangle = (-1)^{p(d-p)} \langle \sigma_p | \omega \rangle^* \quad . \tag{1.31}$$

In this way, the sign factor in the duality of complexes consistently induces the usual sign factor in the Hodge duality:

$$\langle * * \omega | \sigma_p \rangle = \langle \omega | \star \star \sigma_p \rangle = (-1)^{p(d-p)} \langle \omega | \sigma_p \rangle \quad . \tag{1.32}$$

This completes the review of the discrete Hodge dualities.

1.4.3 Exterior calculus on complexes

Following the construction of exterior calculus in a discrete setting, we continue now with the construction of the exterior operator on discrete forms. In the continuum, the differential operator d is a map from p-forms to $(p+1)$-forms: $d : \Omega^p(\mathcal{M}) \to \Omega^{p+1}(\mathcal{M})$. We then take this insight along with Stokes's theorem to derive a discrete version of this operator: Consider a differential form $\omega \in \Omega^{p-1}(K)$ over a one simplex σ_p in the triangulation of a pseudo-manifold with corresponding complex K. Stokes's theorem states that:

$$\mathrm{d}\omega(\sigma_p) = \int_{\sigma_p} \mathrm{d}\omega_{cont} = \int_{\partial\sigma_p} \omega_{cont} = \omega(\partial\sigma_p) \quad . \tag{1.33}$$

Therefore, we define the *differential* of $\omega \in \Omega^{p-1}(K)$ on an abstract simplicial complex K as:

$$d\omega(\sigma_p) = V_{\sigma_p} \langle d\omega | \sigma_p \rangle := \omega(\partial\sigma_p) := \sum_{\sigma_{p-1} \in \partial\sigma_p} \mathrm{sgn}(\sigma_{p-1}, \sigma_p) V_{\sigma_p} \langle \omega | \sigma_{p-1} \rangle \quad . \tag{1.34}$$

The sign factor $\mathrm{sgn}(\sigma_{p-1}, \sigma_p)$ accounts for the relative orientation of the $(p-1)$-face σ_{p-1} within the oriented p-simplex σ_p, and it is determined by comparing the ordering of vertices:

$$\mathrm{sgn}(\sigma_{p-1}, \sigma_p) := \mathrm{sgn}(i_1 \dots \hat{i}_j \dots i_p)\, \mathrm{sgn}(i_1 \dots i_p) \quad , \tag{1.35}$$

where $\hat{i}_j$ denotes omission of the j-th vertex. Thus, this factor ensures that orientations are treated consistently across simplices.

Similarly, the differential on dual forms $\omega \in \Omega^{d-p-1}(\star K) \cong \Omega^{p+1}(K)$ can be defined as:

$$V_{\sigma_{d-p}}\langle \sigma_{d-p}|d\omega\rangle := \sum_{\sigma_{d-p-1}\in\partial\sigma_{d-p}} \operatorname{sgn}(\sigma_{d-(p+1)},\sigma_{d-p}) V_{\sigma_{d-(p+1)}}\langle \sigma_{d-(p+1)}|\omega\rangle \quad , \tag{1.36}$$

or equivalently:

$$V_{\star\sigma_p}\langle \sigma_p|d\phi\rangle := \sum_{\sigma_{p+1};\sigma_p\in\partial\sigma_{p+1}} \operatorname{sgn}(\sigma_{p+1},\sigma_p) V_{\star\sigma_{p+1}}\langle \sigma_{p+1}|\phi\rangle \quad . \tag{1.37}$$

This concludes or review of exterior calculus on simplicial complexes. We now have enough tools to rewrite (1.16) in a discrete setting.

1.5 Scalar matter on an irregular discretization

We can now employ the tools from discrete exterior calculus of the above section to rewrite the action (1.16). First, we can massage this action so a direct identification with discrete objects can be made. In the continuum, we can perform a integration by parts on the term $\int_{\mathcal{M}} d\phi \wedge \star d\phi$ in (1.16) as follows:

$$\int_{\mathcal{M}} d\phi \wedge \star d\phi = \int_{\partial\mathcal{M}} \phi \wedge \star d\phi - \int_{\mathcal{M}} \phi \wedge d(\star d\phi) \quad , \tag{1.38}$$

for a manifold with periodic boundary conditions (as the ones we explore in this work), the boundary term does no longer contribute and the above expression simplifies to:

$$\int_{\mathcal{M}} d\phi \wedge \star d\phi = -\int_{\mathcal{M}} \phi \wedge d \star d\phi = \int_{\mathcal{M}} \star d \star d\phi \wedge \star\phi \quad , \tag{1.39}$$

thus, the action (1.16) can be written using the inner product (1.19) as:

$$S = \frac{1}{2}\left[(\star d \star d\phi, \phi) + M^2(\phi,\phi)\right] \quad , \tag{1.40}$$

from this expression, a straight forward identfication of the action on the discrete can be made:

$$S_D = \frac{1}{2}\left[\langle \star d \star d\phi|\phi\rangle + M^2\langle\phi|\phi\rangle\right] \quad . \tag{1.41}$$

In the discrete, we can rewritte the first term of (1.41) as:

$$\frac{1}{2}\langle \star d \star d\phi|\phi\rangle = \frac{1}{2}\sum_{\sigma_0}\langle \star d \star d\phi|\sigma_0\rangle\langle \star\sigma_0|\phi\rangle \quad . \tag{1.42}$$

Using equations (1.34) and (1.22) repeatedly, the above term can be written as:

$$\frac{1}{2}\sum_{\sigma_0}\phi(\sigma_0)\sum_{\sigma_1\supset\sigma_0}\frac{V_{\star\sigma_1}}{V_{\sigma_1}}\mathrm{sgn}(\star\sigma_1,\star\sigma_0)\sum_{\sigma_0'\subset\sigma_1}\mathrm{sgn}(\sigma_0',\sigma_1)\phi(\sigma_0') \quad . \tag{1.43}$$

The second term of (1.41) reads:

$$\frac{M^2}{2}\langle\phi|\phi\rangle = \frac{M^2}{2}\sum_{\sigma_0}\langle\phi|\sigma_0\rangle\langle\star\sigma_0|\phi\rangle = \frac{M^2}{2}\sum_{\sigma_0}\phi_{\sigma_0}(V_{\star\sigma_0}\phi_{\sigma_0}) \quad . \tag{1.44}$$

Collecting (1.43) and (1.44) we obtain the discretized action of the free massive scalar field in a irregular setting:

$$S_D = \sum_{\sigma_0}\phi(\sigma_0)\sum_{\sigma_1\supset\sigma_0}\frac{V_{\star\sigma_1}}{V_{\sigma_1}}\mathrm{sgn}(\star\sigma_1,\star\sigma_0)\sum_{\sigma_0'\subset\sigma_1}\mathrm{sgn}(\sigma_0',\sigma_1)\phi(\sigma_0') + \frac{M^2}{2}\sum_{\sigma_0}V_{\star\sigma_0}\phi(\sigma_0)^2. \quad . \tag{1.45}$$

In the 4D case, the relevant geometric components of the primal and dual lattice on the action are given as follows: V_{σ_1} represents the length of the edge σ_1 connecting the vertices σ_0 and σ_0', whereas $V_{\star\sigma_1}$ is the volume associated to its dual 3-cell. $V_{\star\sigma_0}$ denotes the 4-volume of the 4-cell dual to a vertex.

The action (1.45) can also be rearranged in more compact expression as follows:

$$S_D = \frac{1}{2}\sum_{\sigma_0^i,\sigma_0^j}\phi(\sigma_0^i)K_{ij}\phi(\sigma_0^j) \ , \tag{1.46}$$

where

$$K_{ij} = \begin{cases} \sum_{\sigma_1\supset\sigma_0^i}\frac{V_{\star\sigma_1}}{V_{\sigma_1}}\,\mathrm{sgn}(\star\sigma_1,\star\sigma_0)\mathrm{sgn}(\sigma_0,\sigma_1) + M^2V_{\star\sigma_0} & i=j \\ \frac{V_{\star\sigma_1}}{V_{\sigma_1}}\,\mathrm{sgn}(\star\sigma_1,\star\sigma_0^i)\mathrm{sgn}(\sigma_0^j,\sigma_1) & i\neq j \text{ and } \sigma_0^i,\sigma_0^j\subset\sigma_1 \end{cases} . \tag{1.47}$$

As a consistency check, we now show how this discrete action reduces to the standard form of the scalar field action (1.10) in the case of a regular 4D lattice. In this case, all edges of the primal complex have a constant length a, and we define the dual complex as a shifted version of the primal one, by defining each edge in the dual as the average between two consecutive edges of the primal one. In this setting, the geometric volumes simplify as follows:

$$V_{\sigma_1} = a, \quad V_{\star\sigma_1} = a^3, \quad V_{\star\sigma_0} = a^4.$$

Additionally, after defining an orientation of the simplicial complex, all sign factors in (1.47) are ± 1 and can be absorbed appropriately. Furthermore, in a regular 4D hypercubic lattice, each vertex is connected to 8 neighbors, corresponding to 8 edges. Therefore, for the diagonal entries of K we obtain:

$$K_{ii} = \sum_{\sigma_1 \supset \sigma_0^i} \frac{a^3}{a} + M^2 a^4 = 8a^2 + M^2 a^4.$$

For off-diagonal terms $i \neq j$, where vertices σ_0^i and σ_0^j are connected by an edge, we get:

$$K_{ij} = \frac{a^3}{a} \cdot (-1) = -a^2.$$

Thus, the matrix K for the regular 4D case simplifies to:

$$K_{ij} = \begin{cases} 8a^2 + M^2 a^4 & i = j, \\ -a^2 & i \neq j \text{ and } \sigma_0^i, \sigma_0^j \subset \sigma_1 \end{cases} \tag{1.48}$$

which precisely correspond to the entries of K defined in a regular lattice in eq. (1.11).

We conclude this review of the free scalar field on an irregular lattice by highlighting its applicability within the broader context of this work. The discretized action defined in equation (1.46) has been previously employed in [36] to study the coupling of matter fields to the restricted spin foam model in the semiclassical limit. In our approach, we employ the same formulation to investigate a correlation function that admits a diffeomorphism-invariant interpretation, as will be discussed in Chapter 3. This observable is central to our analysis, as it provides a promising framework to probe physical information in background-independent systems.
Later on, in Chapter 4, we introduce a one-dimensional toy model: a free scalar field defined on a dynamical lattice. As part of this analysis, we compute now the explicit components of the matrix K from equation (1.47), in the one-dimensional setting with periodic boundary conditions. In this simplified configuration, V_{σ_1} corresponds to configuration length l and V_{σ_0} is set trivially to one. We define the lengths on the dual lattice as the average of the two lengths shared by each vertex on the primal lattice. This defines $V_{\star\sigma_0}$ as $l_\star$ and $V_{\star\sigma_1}$ is also set to one. Therefore, K is given by:

$$K_{ij} = \begin{cases} \frac{1}{l_i} + \frac{1}{l_{i-1}} + M^2 l_{\star i} & i = j \\ -\frac{1}{l_{i-1}} & j = i - 1 \\ -\frac{1}{l_i} & j = i + 1 \end{cases} \tag{1.49}$$

This concludes our review of the free massive scalar field defined in an irregular setting.

Chapter 2

Spin Foam Path integral with Quantum Cuboid Intertwiners

This chapter provides a review of the spin foam approach to quantum gravity, with a focus on the Spin(4) EPRL-FK (Engle–Pereira–Rovelli–Livine, Freidel–Krasnov) state sum model with Barbero–Immirzi parameter $\gamma < 1$. We begin by introducing the key concepts that lead to the construction of this spin foam partition function, and then examine the computational challenges associated with performing the full state sum. To address these challenges, we introduce a simplification by restricting the partition function to a specific class of geometries, namely cuboidal configurations. This particular choice can be translated into the allowed set of spins and intertwiners that form the spin foam state sum. We therefore construct the vertex amplitude for this particular model. Despite the simplification, evaluating the full sum remains non-trivial. To make further progress, we replace the vertex amplitude by its approximation in the semiclassical regime. This treatment, together with the restriction to cuboidal geometry, renders the resulting state sum amenable to numerical simulations. Finally, this framework lays the groundwork for exploring, later in this work, the coupling of spin foam models to matter fields that is accessible to numerical evaluations.

2.1 The Spin Foam State Sum

Spin foam models offer a path integral approach to quantum gravity, formulated in a non-perturbative and background-independent manner [52]. Spin foam models were originally conceived to define the dynamics of spin network states, which constitute the kinematical Hilbert space of the Loop Quantum Gravity (LQG) [53]. Thus, spin foam models describe the evolution of spin network states, defining transition amplitudes between boundary states (quantum geometric states). The spin foam path integral, then represents a sum over histories of spin net-

works where each state describes quantum space. In modern constructions, spin foam models depart from the Plebanski-Holst formulation of classical General Relativity (GR) [9], in which gravity is formulated as a constrained topological BF theory [10]. Thus, this formulation of GR, requires the implementation of so-called *simplicity constraints* [54]. In the continuum, the *simplicity constraints* serve the role of breaking the too many symmetries of the theory, thereby reducing the action to the familiar Palatini-Holst action [55]. Then, the constrained topological action is commonly employed to define the formal spin foam path integral. Thus, the goal in this framework is to give meaning to this formal expression. A common approach for this task is to introduce a lattice regulator. This is achieved by replacing the continuum spacetime with a cellular decomposition, typically realized as a triangulation of the manifold, thereby truncating the number of degrees of freedom. The triangulation enables the construction of a dual 2-complex (composed of vertices v, edges e, and faces f). The partition function is then reformulated in this context using group representation theory. Ultimately, the geometry encoded in the formal expression of the path integral is transposed to the discrete setting, represented by the 2-complex colored with group-theoretic data, which now conveys the geometric information. Finally, the *simplicity constraints* are imposed at the quantum level, resulting in specific restrictions on the path integral.

In this section, we will review the main ideas mentioned above that serve to construct the spin foam state sum. Interested readers could find a fully detailed construction of the spin foam path integral in existing reviews of the topic [52, 56, 57] .

2.1.1 Gravity as a constrained BF theory

BF theories are a family of topological theories [10]. In 4D these are constructed from a Lie group G with a Lie algebra $\mathfrak{g}$. The relevant fields are a local connection 1-form ω_{IJ}, which induces a curvature 2-form $F(\omega)^{IJ}$, and a general 2-form B_{IJ} (where $I, J = 0, 1, 2, 3$), all of which take values in the Lie algebra. With these ingredients, the BF action is defined as:

$$S_{BF}[B, \omega] = \int_{\mathcal{M}} B_{IJ} \wedge F(\omega)^{IJ} \,, \tag{2.1}$$

The corresponding equations of motion yield both curvature and torsion that vanish:

$$F(\omega) = 0 \qquad , \qquad d_\omega \equiv dB + [\omega, B] = 0 \tag{2.2}$$

where $[\cdot, \cdot]$ is the Lie bracket of $\mathfrak{g}$. Thus, BF theory is a torsion-free theory with flat connections. As a result, the theory has no local degrees of freedom. On the other hand, if the B-field is constrained to be of the form:

$$B^{IJ} = \frac{1}{2}\epsilon^{IJ}{}_{KL}\, e^K \wedge e^L + \frac{1}{\gamma} e^I \wedge e^J, \tag{2.3}$$

where e^I is a tetrad field [58] and γ is the Immirzi parameter, then local degrees of freedom are allowed, since (2.3) relaxes the previous condition on flat connections. The resulting theory is equivalent to General Relativty in the Palatini-Holst formulation, which can be expressed as a constrained BF theory:

$$S_{\text{PH}} = \int_{\mathcal{M}} B_{IJ} \wedge F(\omega)^{IJ} + \lambda_{IJKL}\, B^{IJ} \wedge B^{KL} \ , \tag{2.4}$$

where λ_{IJKL} is a Lagrange multiplier imposing the so-called *simplicity constraints*, $C(B) = B^{IJ} \wedge B^{KL}$. Varying the action with respect to λ enforces the B-fields to precisely take the form given in equation (2.3).
A further discussion of BF theories and gravity can be found in [59, 60].

2.1.2 Quantized BF theory

Having reformulated GR as a constrained BF theory, we will write a formal path integral for BF theory alone. This serves as the starting point for deriving spin foam amplitudes. This choice is indeed convenient since BF theory, being topological, possesses no local degrees of freedom and can be discretized without altering its physical content. The program of the spin foam path integral approach to quantum gravity is then to define a partition function for pure BF theory and in a subsequent stage to give meaning to the *simplicity constraints*, which will now have to be translated at the quantum level [1]. The implications of these choices will be explored in this and the subsequent subsections.
The formal partition function of the BF theory is given by :

$$Z = \int \mathcal{D}[B]\, \mathcal{D}[\omega] \ \exp\left(i \int_{\mathcal{M}} B^{IJ} \wedge F_{IJ} \right) \tag{2.5}$$

integrating over the B field we obtain:

$$Z = \int \mathcal{D}\omega\, \delta\left(F(\omega)\right) \ , \tag{2.6}$$

this expression is still a formal definition, as the functional integration is not well defined. At the same time, this expression shows that it reduces to a path integral over flat connections.

[1] Although the stage at which simplicity constraints should be imposed is not unique [61, 62]. Furthermore, different implementations of the simplicity constraints give rise to different spin foam models [11].

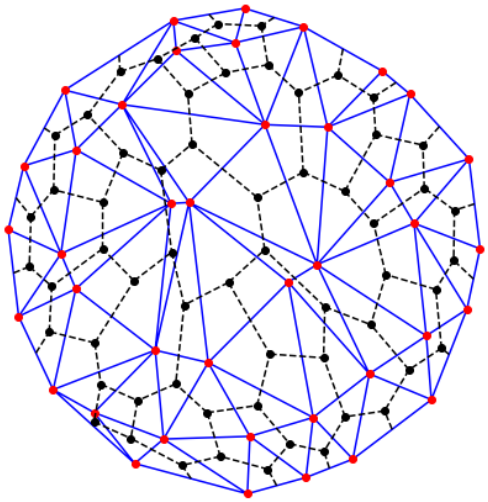

Figure 2.1: Example of a triangulation of a 2 dimensional region. The edges of the triangulation are represented in blue, while the vertices are marked in red. The dual complex is depicted using black dashed lines. In two dimensions, the vertices of the primal triangulation correspond to the faces of the dual complex, the edges of the primal triangulation correspond to the edges of the dual, and the faces of the primal triangulation correspond to the vertices of the dual.

To give meaning to (2.6), we need to introduce a regulator as follows: we start by replacing the d dimensional manifold $\mathcal{M}$ with an arbitrary cellular decomposition, commonly chosen to be a *tringulation* Δ. This decomposition admits a natural dual 2-complex $\Delta^\star$ (see Figure 2.1) (sometimes called the *Poincaré dual* [63]). This is a combinatorial object defined by a set of vertices $v \in \Delta^*$ (dual to d-cells in Δ), edges $e \in \Delta^*$ (dual to $(d-1)$-cells) and faces $f \in \Delta^*$ (dual to $(d-2)$-cells). We can translate the relevant fields of BF theory in 4D to the discretized setting as follows: We star by *smearing* the B fields in 2-cells in Δ:

$$B_f = \int_{2-cell} B \quad . \tag{2.7}$$

Now, the connection ω can be discretized by assigning group elements $g_e \in G$ to edges in the dual decomposition Δ^*. Therefore, we can define the holonomy of ω along the edges $e \in \Delta*$:

$$g_e = \mathcal{P} \exp\left(-\int_e \omega\right) \ , \tag{2.8}$$

where $\mathcal{P}$ stands for the path-ordered product. With these identifications in the discrete, we define the path integral:

$$Z_\Delta = \int \prod_{e\in\Delta^*} dg_e \prod_{f\in\Delta^*} dB_f \, \exp\left(iB_f U_f\right) = \int \prod_{e\in\Delta^*} dg_e \prod_{f\in\Delta^*} \delta(g_{e_1}\cdots g_{e_n}) \ , \tag{2.9}$$

where $U_f = g_{e_1 v_1} \cdots g_{e_n v_n}$ represents the holonomy around a face in Δ^* and dg_e is the Haar measure [64] on the group G. As in eq. (2.6), the delta function on the r.h.s of eq. (2.9) represents the integration over the B_f fields. In this case the flatneess condition is implemented on every face $f \in \Delta^*$ via $U_f = \mathbb{1}$.
For compact groups G, the integration over the group elements in eq. (2.9) can be carried out by expanding the delta function using the Peter-Weyl Theorem:

$$\delta(g) = \sum_{\rho} \mathrm{d}_\rho \, \mathrm{Tr}[\rho(g)] \ , \tag{2.10}$$

where ρ are irreducible unitary representations of G, d_ρ the dimensions of the vector spaces given by the representation ρ and $\chi = \mathrm{Tr}[\rho(g)]$ is the character of ρ. Applying the Peter-Weyl Theorem to each face $f \in \Delta^*$, we can write eq. (2.9) as:

$$Z_\Delta = \sum_{\{\rho\}\to\{f\}} \int \prod_{e\in\Delta^*} dg_e \prod_{f\in\Delta^*} \mathrm{d}_{\rho_f} \, \mathrm{Tr}[\rho_f(g_{e_1}\ldots g_{e_n})] \ . \tag{2.11}$$

We can massage this expression to obtain:

$$Z_\Delta = \sum_{\{\rho\}\to\{f\}} \prod_{f\in\Delta^*} \mathrm{d}_{\rho_f} \mathrm{Tr}_f \left[\prod_{e\in\Delta^*} \left(\int dg_e \, \rho_f(g_{e_1}) \cdots \rho_f(g_{e_n}) \right) \right] \ , \tag{2.12}$$

where we have used the fact that $\rho(g_1 g_2) = \rho(g_1)\rho(g_2)$ to write $\mathrm{Tr}(\rho(U_f)) = \mathrm{Tr}[\rho(g_{e_1}) \cdots \rho(g_{e_n})]$. In eq. (2.12) Tr_f denotes the contraction of the indices that follow *for each single face*.
Noticing that in D dimensions, the edges $e \in \Delta^*$ are shared exactly by D faces in Δ^*, we can identify the argument of the trace in eq. (2.12) to be a product for each edge of a Haar projector P^e_{inv}:

$$P^e_{inv}(\rho_1, \ldots, \rho_D) = \int dg_e \, \rho_1(g_e) \otimes \rho_2(g_e) \otimes \cdots \otimes \rho_D(g_e) \ . \tag{2.13}$$

As shown in Appendix A, due to the invariance of the Haar mesuare, P^e_{inv} indeed satisfies $P^e_{inv} = (P^e_{inv})^2$ for compact G groups. In eq. (2.12) these projectors then get contracted according to the trace around faces in Δ^*. It is also important to mention that the tensor product of D ρ matrices defines the space $\mathcal{H} = \mathcal{H}^{\rho_1} \otimes \cdots \otimes \mathcal{H}^{\rho_D}$ and P^{ev}_{inv} is the projector on the invariant states in $\mathrm{Inv}[\mathcal{H}^{\rho_1} \otimes \cdots \otimes \mathcal{H}^{\rho_D}]$, where the invariant space is defined as:

$$\mathrm{Inv}_G(\mathcal{H}) \equiv \{ v \in \mathcal{H} \mid \forall \, g \in G, \ \rho(g)v = v \} \ . \tag{2.14}$$

Returning to our BF path integral in Δ, we obtain:

$$Z_\Delta = \sum_{\{\rho\}\to\{f\}} \prod_{f\in\Delta^*} \mathrm{d}_{\rho_f} \prod_{e\in\Delta^*} \mathrm{Tr}_f[P^e_{inv}(\rho_1,\cdots,\rho_D)] \ , \tag{2.15}$$

Thus, BF quantum amplitudes are given by the sum over all possible assignments of irreducible representations of G to faces of Δ^* and the contraction among projectors P^e_{inv} defined by the pattern of faces in Δ^*.
There exists a graphical representation introduced in [65] of the projector in eq. (2.13). In eq. (2.15) a representation is assigned to each face in Δ^* and in the graphical notation (2.16), this is represented as a strand that goes around faces in Δ^*. An integration over a group element g_e is represented by a box:

$$P^e_{inv}(\rho_1,\rho_2,\rho_3,\cdots,\rho_D) = \tag{2.16}$$

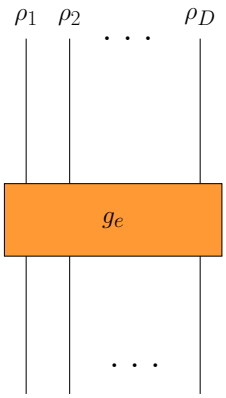

The way strands connect to each box is determined by the combinatorial structure of the triangulation, i.e., how faces are glued in Δ^*. As an illustrative example, consider the 2D case: here, the triangulation Δ consists of triangles joined along edges. At each triangle vertex, a representation ρ_i is assigned, and each shared edge corresponds to an integration over a group element. Since an edge in Δ is dual to a face in Δ^*, and is shared by two triangles, the group element g_e appears in two representations, which are represented graphically by two strands entering the same box.
The above logic can be extrapolated to the 4D case (which is more difficult to visualize), in this case a triangulation is made of 4-simplices glued together. In this case, every 4-simplex is made up of five tetrahedra (each made up of four triangles) and ten triangles. Each edge in Δ^* is shared by four faces, that is, four strands. For this case, five group integrations are performed, one for each tetrahedra. In the graphical notation, the partition function reads:

$$Z_\Delta = \sum_{\{\rho\}\to\{f\}} \prod_{f\in\Delta^*} \mathrm{d}_{\rho_f} \qquad (2.17)$$

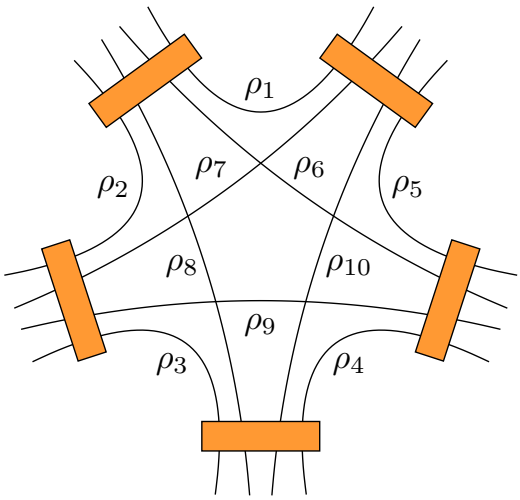

In this graphical notation, one obtains such a diagram (strands and boxes) for each vertex in Δ. The strands in this notation are understood to be contracted around faces in Δ^*. In (2.17) every tetrahedron is represented by a box that shares four strands (triangles) with other tetrahedra. The 10 strands correspond to the 10 faces $f \in \Delta^*$ sharing a vertex $v \in \Delta^*$ and connected to the neighboring vertices through the 5 boxes, corresponding to the 5 edges sharing the vertex $v \in \Delta^*$.

Further steps can be taken to elucidate the meaning of the partition function in equation (2.17); however, these steps depend on the choice of gauge group G and the dimensions and signature of the manifold $\mathcal{M}$. In this work, we focus on the four-dimensional Riemannian EPRL-FK spin foam model (Engle–Pereira–Rovelli–Livine, Freidel–Krasnov) [14, 12]. Accordingly, our gauge group is $Spin(4) = SU(2) \times SU(2)$, given the isomorphism $\mathfrak{so}(4) \cong \mathfrak{su}(2) \times \mathfrak{su}(2)$. In particular, we choose the Barbero–Immirzi parameter γ such that $\gamma < 1$. An overview of the Riemannian EPRL-FK model will be provided in a subsequent section. For now, its relevance lies in the fact that the partition function retains a structure similar to that of equation (2.17), but with additional constraints on the labeling of representations, imposed by the *simplicity constraints*. To set the stage, we begin by reviewing the partition function of pure BF theory with gauge group $Spin(4)$. However, since the elementary building blocks of $Spin(4)$ are copies of the $SU(2)$ group, it will be shown that the final amplitudes for the $Spin(4)$ group are expressed in terms of the $SU(2)$ amplitudes. Therefore, we will first review the $SU(2)$ BF partition function.

2.1.3 SU(2) BF theory

As a warm-up, we explore the BF partition function (2.15) with the gauge group $SU(2)$. This is the group of 2×2 complex matrices with unit determinant that satisfy the unitary condition:

$$\det(u) = 1, \quad \text{and} \quad u^{-1} = u^{\dagger}, \ \forall\, u \in SU(2)\,. \tag{2.18}$$

$SU(2)$ is also a double cover of the rotation group $SO(3)$ and is generated by the algebra of the angular momentum L_i, with $i = 1, 2, 3$, satisfying the commutation relations:

$$[L_i, L_j] = i\epsilon_{ijk} L_k \ . \tag{2.19}$$

In the fundamental representation $L_i = \sigma_i/2$ where σ_i are the Pauli matrices. The corresponding Casimir operator is $L^2 = \vec{L} \cdot \vec{L}$ and the unitary irreducible representations are labeled by spins (half-integers): $\rho_f = j_f \in \mathbb{N}/2$ and are $2j + 1$ dimensional. In the canonical basis of these representations, L^2 and L_3 are diagonalized as follows:

$$L^2|j, m\rangle = j(j+1)|j, m\rangle\,, \qquad L_3|j, m\rangle = m|j, m\rangle\,, \tag{2.20}$$

where $-j \leq m \leq j$. In this basis, the matrix elements of the representation are given by the Wigner matrices:

$$D^j_{mn}(u) = \langle j, m|\rho_j(u)|j, m\rangle\,. \tag{2.21}$$

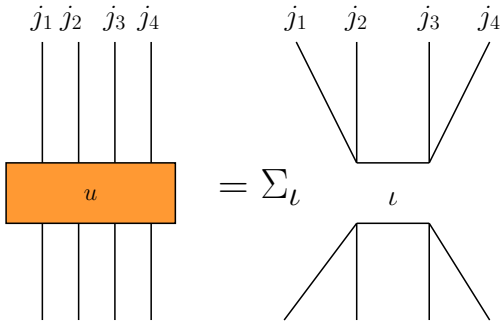

Figure 2.2: Intertwiner representation of a four valent strand-box diagram.

In 4D, the edges $e \in \Delta^*$ are shared by 4 vertices, so the projector (2.13) is a function of four representations, $P^e_{inv} = P^e_{inv}(j_1, j_2.j_3, j_4)$. In this case, the invariant vector space is $\mathrm{Inv}_{SU(2)}[j_1 \otimes j_2 \otimes j_3 \otimes j_4]$, which generally has dimensions greater than one. Now, referring to Appendix A, we can write P^e_{inv} in terms of an intertwiner basis of the $\mathrm{Inv}_{SU(2)}[j_1 \otimes j_2 \otimes j_3 \otimes j_4]$ space:

$$\int dg\, D^{j_1}_{m_1\, n_1}(g) D^{j_2}_{m_2\, n_2}(g) D^{j_3}_{m_3\, n_4}(g) D^{j_4}_{m_1\, n_4}(g) = \sum_{\iota} |\iota_{j_1,j_2,j_3,j_4}\rangle\langle\iota_{j_1,j_2,j_3,j_4}|\ , \tag{2.22}$$

where the sum in the r.h.s of the last expression is over an orthonormal basis of intertwiners[2], which can be labeled by a half integer. Graphically, (2.22) can be represented as shown in Figure 2.2. As mentioned above, in 4 dimensions, the edges $e \in \Delta^*$ are shared by four faces and thus the relevant projector is represented by a box with four wires. The four-valent diagrams on the right-hand side represent elements of an orthonormal basis of $\mathrm{Inv}_{SU(2)}[j_1 \otimes j_2 \otimes j_3 \otimes j_4]$ and its dual, which are labeled by a half integer ι.
With this notation, we can rewrite the $SU(2)$ BF partition function as:

$$Z_\Delta = \sum_{\{f\}\to j_f} \prod_{f\in\Delta^*} \mathrm{d}_{j_f} \sum_{\{e\}\to \iota_e}$$

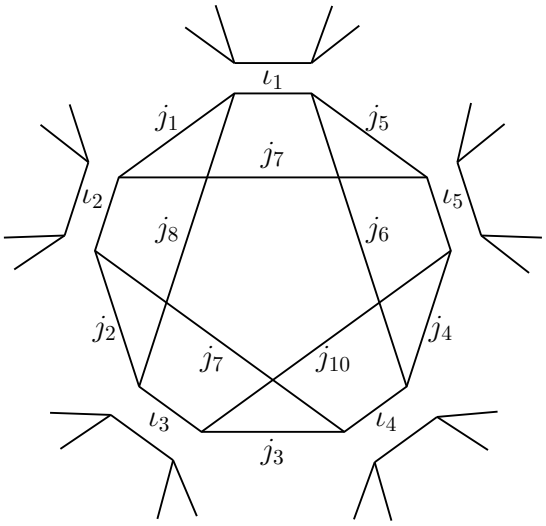

(2.23)

Thus, in this representation, we associate a contraction of intertwiners to each vertex. Such contraction gives a number, which we define as the vertex amplitude. Thus, it is customary to write the above expression as a sum over vertex amplitudes as follows:

$$Z_\Delta = \sum_{\{f\}\to j_f} \prod_{f\in\Delta^*} \mathrm{d}_{j_f} \sum_{\{e\}\to \iota_e} \prod_{v\in\Delta^*}$$

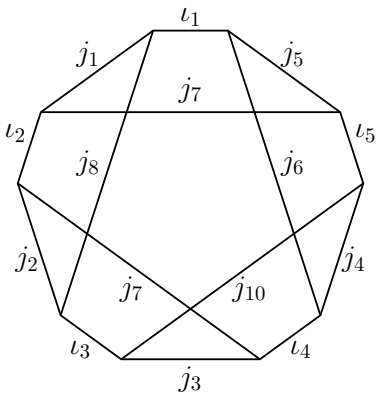

(2.24)

[2]The explicit construction of this basis can be found using recoupling theory, see, for example, [66, 67]. However, its detailed form is not essential for the purposes of this work.

The vertex amplitude in (2.24) is often called a $15j$-symbol.
It is also important to notice that the spin foam state sum from above can be succinctly expressed as a sum over a product of edges, faces and vertex amplitudes:

$$Z_\Gamma = \sum_{j_f, \iota_e} \prod_f A_f \prod_e A_e \prod_v A_v \ . \tag{2.25}$$

We conclude this section by noting that equation (2.25) represents the general form in which spin foam models are expressed. Naturally, the specific forms of the amplitudes A_f, A_e, A_v depend on the dimension and signature of the underlying manifold, as well as on the choice of gauge group G.

2.1.4 $Spin(4)$ BF Theory : Towards 4D Riemannian gravity

We now extend the BF theory partition function to the gauge group $Spin(4) = SU(2) \times SU(2)$. Given the structure of this group, the construction of the partition function in turn can be easily extrapolated from the $SU(2)$ case, since the structure of the $Spin(4)$ group implies that $Z_{BF}(SU(2) \times SU(2)) = Z_{BF}(SU(2))^2$. Thus, the first step is to work out the expression of the projector (2.13) for the $Spin(4)$ group, and rewrite it in terms of an orthonormal basis of intertwiners. In the graphical notation, this reads:

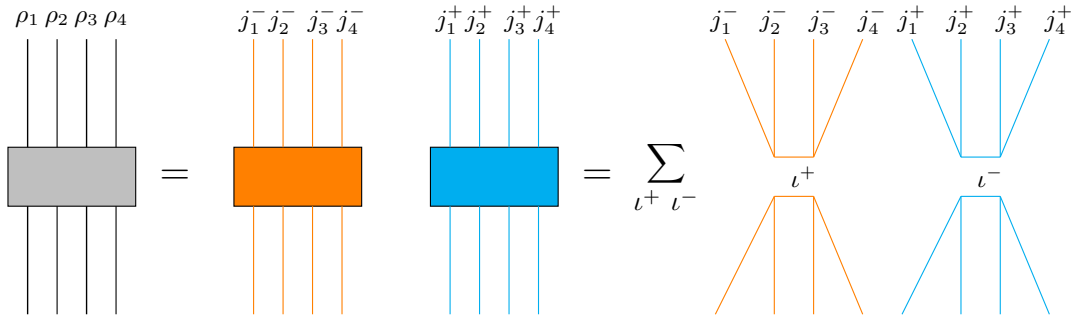

(2.26)

where now $\rho_f = j_f^- \otimes j_f^+$, and $\iota^\pm$ are the half integers labelling the unitary representations of $Spin(4) = SU(2) \times SU(2)$. Using this prescription and the same logic from the $SU(2)$ case, we can express the partition function of $Spin(4)$ as a product of two $SU(2)$ ones, namely:

$$Z_{BF}(\Delta) = \sum_{\{f\}\to\rho_f} \prod_{f\in\Delta^*} \mathrm{d}_{j_f^+}\mathrm{d}_{j_f^+} \sum_{\{e\}\to\iota_e} \prod_{v\in\Delta^*}$$

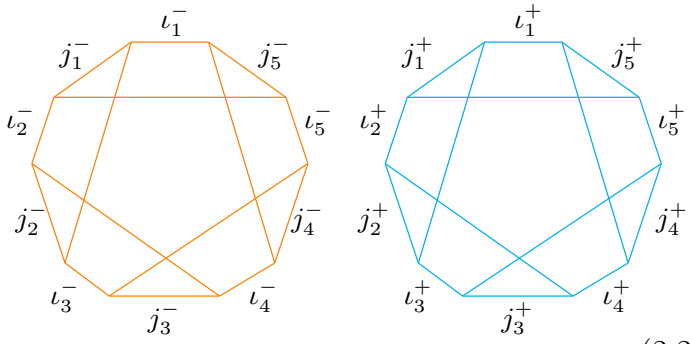

(2.27)

In the same way, we can succinctly express (2.27) as a product of faces, edges and faces amplitudes:

$$Z_\Gamma = \sum_{j_f,\iota_e} \prod_f A_f^\pm \prod_e A_e^\pm \prod_v A_v^\pm \ . \tag{2.28}$$

2.1.5 The 4D Riemannian EPRL-FK model

We now have the necessary ingredients to discuss the spin foam model formulation of the 4D Riemannian EPRL-FK model. In what follows, we briefly review the main components of this model, as the detailed construction is not essential for the purposes of this work. This section largely follows the presentation in [52].

The partition function of the $Spin(4)$ BF theory, given in equation (2.28) still a topological theory and does not yet represent a model of quantum gravity, as it lacks the implementation of the simplicity constraints $C(B)$ introduced in equation (2.4). These constraints ensure that the B fields come from a tetrad field e^I as specified in equation (2.3). Therefore, the final step in constructing a spin foam model is to impose these constraints within the path integral (2.28). As we shall eventually show, the *simplicity constraints* are translated at the quantum level as some restrictions in the labels of the group representations in the path integral. Thus, it is important first to review the representation theory of $Spin(4)$. This can be described in terms of the generators $J_\pm^i$ such that:

$$[J_\pm^i, J_\pm^j] = \epsilon_k^{ij} J_\pm^k \ . \tag{2.29}$$

The unitary reducible representations $\mathcal{H}_{j^+,j^-}$ of $Spin(4)$ are given by the product of unitary irreducible representations of $SU(2)$, which are labelled by two half-integers $j^\pm$. In this case, the basis of $\mathcal{H}_{j^+,j^-}$ is given by the states $|j^+, j^-, m^+, m^-\rangle$ which are eigenstates of the Casimirs

$C_1 = J_+^2 + J_-^2$ and $C_2 = J_+^2 - J_-^2$ and J_+^3 and J_-^3.
An important property of the unitary irreducible representations of Spin(4) is that they can be decomposed into a direct sum of SU(2) irreducible representation spaces:

$$\mathcal{H}_{j^+,j^-} = \bigoplus_{j=|j^+-j^-|}^{j^++j^-} \mathcal{H}_j \,, \tag{2.30}$$

where j^+ and j^- label the spins associated with the two SU(2) sectors of Spin(4).
Another key feature of the Spin(4) group is that its Lie algebra, as defined in equation (2.29), can be expressed in terms of rotation generators L^i and boost generators K^i:

$$\begin{aligned}
&[L_3, L_\pm] = \pm L_\pm \quad , \quad [L_+, L_-] = 2L_3 \\
&[L_+, K_+] = [L_-, K_-] = [L_3, K_3] = 0 \\
&[K_3, L_\pm] = \pm K_\pm \quad , \quad [L_\pm, K_\mp] = \pm 2K_3 \quad , \quad [L_3, K_\pm] = \pm K_\pm \\
&[K_3, K_\pm] = \pm L_\pm \quad , \quad [K_+, K_-] = 2L_3 \,,
\end{aligned} \tag{2.31}$$

where $K_\pm = K^1 \pm iK^2$ and $L_\pm = L^1 \pm iL^2$.
We now turn to the simplicity constraints $C(B)$. We note that these depend only on the B-fields, which we integrated out in faces of Δ^* in (2.9). In a similar fashion, the *simplicity constraints* have been shown [14] to be equivalent in the discrete setting to a linear constraint on each face $f \in \Delta^*$ of a given tetrahedron as:

$$D_i^f = L_f^i - \frac{1}{\gamma} K_f^i \approx 0, \tag{2.32}$$

commonly referred to as the linear simplicity constraints. In the EPRL model, these constraints are imposed as operator equations on the Hilbert spaces corresponding to the unitary irreducible representations of $Spin(4)$ that define the BF partition function in equation (2.28). However, the constraints in (2.32) do not form a closed algebra, since their commutator yields:

$$[D_f^i, D_{f'}^j] = 2\delta_{ee'}\epsilon^{ij}{}_k D^k + \delta_{ee'} \frac{1-\gamma^2}{\gamma^2} \epsilon^{ij}{}_k L_f^k \quad , \tag{2.33}$$

this non-closure implies that the simplicity constraints do not form a first-class algebra. As a result, imposing them strongly at the quantum level, i.e., requiring that physical states be annihilated by the constraint operators, would lead to an over-constrained and possibly trivial theory. Consequently, a weaker imposition of the simplicity constraints has been devised. In

the EPRL model, this is achieved by restricting the set of representations that appear in the BF partition function such that the constraints (2.32) are satisfied in the strongest possible way, while remaining consistent with the uncertainty relations implied by the non-closure property in (2.33). One possibility is to study the Master constraint $M_f = D_f \cdot D_f$. A weak imposition of (2.32) accounts to look for the minimum eigenvalue among spaces $\mathcal{H}_j \in \mathcal{H}_{j^+,j^-}$, that is, finding the minimum eigenvalue of $M_f|\psi\rangle = m_{j^\pm,j}|\psi\rangle$, where

$$m_{j^\pm,j} = (1-\gamma)^2 j_+(j_++1) + (1+\gamma^2) j_-(j_-+1) - (1-\gamma^2)\left[j(j+1) - j_+(j_++1) - j_-(j_-+1)\right] . \tag{2.34}$$

We therefore distinguish two cases based on the value of the Barbero–Immirzi parameter γ: $\gamma < 1$ and $\gamma > 1$. In the first case, the minimal spin labels are given by:

$$j^\pm = (1 \pm \gamma) j/2 \tag{2.35}$$

while in the second case, they take the form:

$$j^\pm = (\gamma \pm 1) j/2 \ . \tag{2.36}$$

This immediately requires γ to be a rational number to get half integers. This is considered a pathology of the Riemannian model, which is absent in the Lorentzian theory. The choice of γ therefore leads to slightly different spin foam models, as it affects the structure of the representations and ultimately the form of the vertex amplitudes. In all cases, the restriction on the representations take the form of the selection of a subspace $\mathcal{H}_j \subset \mathcal{H}_{j^+,j^-}$ given by unitary irreducible representations of a subgroup $SU(2) \in Spin(4)$. As mentioned in the previous section, in this work we focus on the case $\gamma < 1$, which amounts to choosing the maximum weight component $j = j^+ + j^-$ in the expansion 2.30. This regime offers the advantage of yielding more manageable expretssions for the amplitudes. Moreover, it is supported by extensive literature, which facilitates comparison with existing results and allows us to carry out explicit computations under further assumptions that will be introduced later in this chapter.
There exists also a graphical representation of the vertex amplitude for the EPRL model analogous to the expression in (2.27) . For now, we finish our discussion of the Riemannian EPRL model. For further details see [52]. For our purposes, we rather focus on the coherent representation of the partition function, which we introduce in the next section.

2.1.6 SU(2) coherent states and intertwiners

The construction of a coherent intertwiner basis depends on the choice of gauge group G. As discussed in previous sections, the relevant group for our analysis is the $Spin(4)$ group, which can be decomposed into two copies of $SU(2)$. Consequently, intertwiners for $Spin(4)$ can be constructed from pairs of coherent intertwiners associated with $SU(2)$. To build these $Spin(4)$ intertwiners, we begin by introducing the coherent intertwiner structure in the $SU(2)$ case.

In the representation space $\mathcal{H}_j$ of dimension $d_j = 2j+1$, the identity operator can be expressed in terms of the standard orthonormal basis $|j,m\rangle$ as:

$$\mathbb{1}_j = \sum_m |j,m\rangle\langle j,m| \,, \tag{2.37}$$

where $-j \leq m \leq j$. Nevertheless, there exists an overcomplete basis $|j,g\rangle \in \mathcal{H}_j$ labeled by $g \in SU(2)$ such that:

$$\mathbb{1}_j = \mathrm{d}_j \int_{SU(2)} dg \; |j,g\rangle\langle j,g| \;, \tag{2.38}$$

where the new states $|j,g\rangle \in \mathcal{H}_j$ are $SU(2)$ Perelomov coherent states [68]. These states are defined by the action on a reference state. A common choice is the maximum weight state $|j,j\rangle$ with respect to $\tau_3 = \frac{i}{2}\sigma_3$, corresponding to the unit vector in the 3- or z-direction. Thus:

$$|j,g\rangle \equiv D^j(g)|j,j\rangle = \sum_m |j,m\rangle D^j_{mj}(g) \,, \tag{2.39}$$

where $D^j_{mj}(g)$ are the Wigner matrices. Since for any $h \in U(1) \subset SU(2)$, the action $D^j(gh)$ differs from $D^j(g)$ only by a phase, these coherent states are naturally labeled by points on the two-sphere $S^2 \cong SU(2)/U(1)$. We thus define:

$$|j,\vec{n}\rangle := |j,g\rangle \quad \text{such that} \quad g \triangleright \vec{e}_3 = \vec{n} \;\; , \tag{2.40}$$

where $\vec{e}_3$ is the unit vector in the z-direction and $\triangleright$ denotes the adjoint action of $SU(2)$ on $\mathbb{R}^3$. Explicitly, this means $g \triangleright \vec{v} := R(g)\vec{v}$, with $R(g) \in SO(3)$ the rotation associated with $g \in SU(2)$. With this identification, the resolution of the identity in $\mathcal{H}_j$ takes the form:

$$\mathbb{1}_j = d_j \int_{S^2} d\vec{n} \; |j,\vec{n}\rangle\langle j,\vec{n}| \,, \tag{2.41}$$

where $d_j = 2j + 1$, and the integral is taken over the unit sphere S^2 with the invariant (Haar-induced) measure. The states $|j, \vec{n}\rangle$ form an overcomplete basis of $\mathcal{H}_j$. At the same time, these states encode semiclassical information. For example, consider the angular momentum operators J^i, which generate the Lie algebra $\mathfrak{su}(2)$. One finds that:

$$\langle j, \vec{n}|\vec{J}, |j, \vec{n}\rangle = j\,\vec{n} \ , \tag{2.42}$$

where $\vec{n}$ is a three dimensional unit vector $\vec{n} \in S^2$. Moreover, it can be shown that the fluctuations in of $\vec{J}^2$ are minimized, with $\Delta J^2 = \hbar^2 j$. Therefore, the state $|j, n\rangle$ can be interpreted as a semiclassical state representing a vector of length j pointing in the direction $\vec{n} \in \mathbb{R}^3$.
Equation (2.41) also admits a graphical notation:

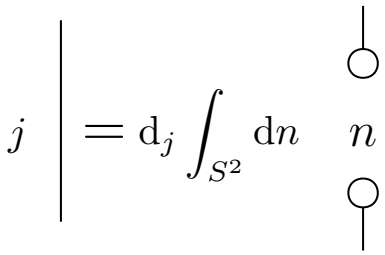

(2.43)

It is also worthy mentioning a useful property of the $SU(2)$ coherent states. Given that:

$$|j, j\rangle = |\tfrac{1}{2}\tfrac{1}{2}\rangle|\tfrac{1}{2}\tfrac{1}{2}\rangle \cdots |\tfrac{1}{2}\tfrac{1}{2}\rangle = |\tfrac{1}{2}, \tfrac{1}{2}\rangle^{\otimes 2j} \tag{2.44}$$

then

$$|j, \vec{n}\rangle = |\tfrac{1}{2}, \vec{n}\rangle^{\otimes 2j} \ . \tag{2.45}$$

We now turn to the construction of coherent intertwiners for the SU(2) group [69]. In the four-dimensional case, each edge of the spin foam is associated with an invariant subspace of the tensor product of four representations:

$$\mathcal{H}_0 = \mathrm{Inv}_{\mathrm{SU}(2)}\left[j_1 \otimes j_2 \otimes j_3 \otimes j_4\right]$$

(see equation (2.14)). The spin foam quantization assigns to each edge an integral over the group, which is evaluated by inserting into $\mathcal{H}_0$ a resolution of the identity:

$$\mathbb{1}_{\mathcal{H}_0} = \sum_{\iota} |\iota_{j_1,j_2,j_3,j_4}\rangle \langle \iota_{j_1,j_2,j_3,j_4}| \ , \tag{2.46}$$

where the sum is taken over an orthonormal basis of intertwiners. In [69], coherent intertwiners were introduced to provide a clearer geometric interpretation of the spin foam state sum. These are defined by group-averaging the tensor product of N_f $SU(2)$ coherent states $|j_i, \vec{n}_i\rangle$, where N_f denotes the number of faces incident on a given edge in Δ^*. The group averaging enforces gauge invariance and leads to the definition of the *Livine–Speziale coherent intertwiners*:

$$|\iota\rangle_0 := \int_{\mathrm{SU}(2)} dg \bigotimes_{i=1}^{N_f} g \triangleright |j_i, \vec{n}_i\rangle \ . \tag{2.47}$$

If the *closure condition*: $\sum_{i=1}^{N_f} j_i \, \vec{n}_i = 0$ is satisfied, then *Minkowski's theorem* [70] guarantees the existence of a unique (up to translation) convex polyhedron with face areas proportional to j_i and face normals given by $\vec{n}_i$. Therefore, the coherent intertwiner can be interpreted geometrically as a quantum state peaked on a classical polyhedron in $\mathbb{R}^3$.

Finally, we brefiely summirzed how to implement the construction of the intertwiners within the EPRL model with Barbero-Immirzi parameter $\gamma < 1$ (see subsection 2.1.5). This is commonly implemented by defining the boost map Y_γ consisting of two parts. For an SU(2) intertwiner ι, each vector space V_j is isometrically embed into the unique component appearing in the Clebsch–Gordan decomposition of $V_{j^+,j^-} \simeq V_{j^+} \otimes V_{j^-}$. We call this map β^γ_j as it explicitly depends on γ. The resulting tensor is not necessarily a $\mathrm{SU}(2) \times \mathrm{SU}(2)$ intertwiner; thus we act with the Haar projector $\mathcal{P}$ to enforce this condition. For an N-valent intertwiner Y_γ reads:

$$Y_\gamma : \mathrm{Inv}(V_{j_1} \otimes \cdots \otimes V_{j_N}) \to \mathrm{Inv}(V_{j_1^+,j_1^-} \otimes \cdots \otimes V_{j_N^+,j_N^-})$$

$$Y_\gamma := \mathcal{P} \circ (\beta^\gamma_{j_1} \otimes \cdots \otimes \beta^\gamma_{j_N}). \tag{26}$$

Eventually, the vertex amplitude A_v is defined as the contraction of the intertwiners associated with the vertex v:

$$A_v := \mathrm{Tr}_{e \supset v}(Y_\gamma(\iota_e)) \ . \tag{2.48}$$

2.1.7 Riemannian EPRL-FK model in the coherent state basis

We are now ready to express the vertex amplitude of the Spin(4) EPRL-FK model with Barbero–Immirzi parameter $\gamma < 1$ in the coherent state representation. This representation is particular useful to study the semiclassical properties of the amplitudes as it will be shown in later section. In this section, we present only the final expression of the amplitude, without delving into the detailed derivation. One of the key ideas is to insert the resolution of the identity (2.41) on each strand connecting neighboring vertices in each copy of the $SU(2)$ vertex amplitude in the strand-box notation. Applying the graphical representation introduced in (2.43), we finally obtain:

$$Z^{\gamma<1}_{\mathrm{EPRL}}(\Delta) = \sum_{j_f} \prod_{f\in\Delta^*} \mathrm{d}_{j_f^-}\mathrm{d}_{j_f^+} \int \prod_{e\in\Delta^*} \mathrm{d}_{j_{ef}}\, \mathrm{d}n_{ef}$$

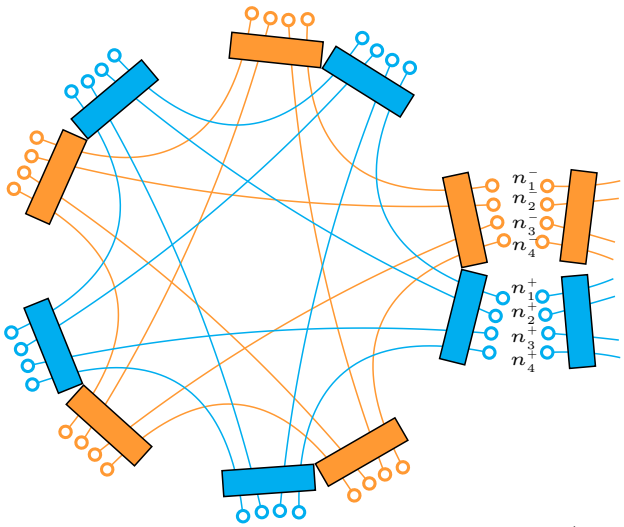

(2.49)

where have explicitly written the integration variables only in one of the boxes.
A very useful representation of (2.49) is given in terms of an effective action, which allows us to investigate semiclassical properties of the vertix amplitude using the stationary phase approximation as will be shown in subsequent sections. For now, if we restore the explicit group integrations represented by boxes in (2.49) we obtain:

$$\begin{aligned} Z^{\gamma<1}_{EPRL}(\Delta) = & \sum_{c_f:\{f\}\to\rho_f} \prod_{f\in\Delta^*} \mathrm{d}_{j_f^-}\mathrm{d}_{j_f^+} \int \prod_{e\in\Delta^*} \mathrm{d}_{j_{ef}^-}\mathrm{d}_{j_{ef}^+}\, dn_{ef}^-\, dn_{ef}^+ \\ & \times \prod_{v\in\Delta^*} \prod_{e,e'\in v} dg_{ev}^- dg_{ev}^+ \left(\langle n_{ef}^-|(g_{ev}^-)^{-1} g_{e'v}^- |n_{e'f}^-\rangle\right)^{2j_f^-} \left(\langle n_{ef}^+|(g_{ev}^+)^{-1} g_{e'v}^+ |n_{e'f}^+\rangle\right)^{2j_f^+} , \end{aligned} \tag{2.50}$$

where we have used the coherent state property (2.45) and where $|n\rangle$ is a handy notation for $|\frac{1}{2}, n\rangle$. The $g_{ev}^{\pm}$ denote the group elements associated to the five boxes for each given vertex as in (2.49). The main component of (2.50) is the vertex amplitude $\mathcal{A}_v$, which we identify as:

$$\begin{aligned}\mathcal{A}_v &= \int_{\mathrm{SU}(2)^{N_f}} \prod_{i=1}^{N_f} dg_i^- \prod_{a<b} \langle -\vec{n}_{ba}|(g_b^-)^{-1} g_a^- |\vec{n}_{ab}\rangle^{2j_{ab}^-} \times \int_{\mathrm{SU}(2)^{N_f}} \prod_{i=1}^{N_f} dg_i^+ \prod_{a<b} \langle -\vec{n}_{ba}|(g_b^+)^{-1} g_a^+ |\vec{n}_{ab}\rangle^{2j_{ab}^+} \\ &=: \mathcal{A}_v^- \mathcal{A}_v^+\end{aligned} \tag{2.51}$$

where a and b denote intertwiners, and pairs ab the links connecting intertwiner a to b. We can also express $\mathcal{A}_v^{\pm}$ succinctly as:

$$A_v^{\pm} = \int_{SU(2)^{N_f}} \prod_{i=1}^{N_f} dg_i^{\pm}\, e^{S^{\pm}} \tag{2.52}$$

where the inner products of $SU(2)$ coherent states were exponentiated to define the action:

$$S^{\pm} := \sum_{a<b} 2j_{ab}^{\pm} \ln \langle -\vec{n}_{ba}|(g_b^{\pm})^{-1} g_a^{\pm} |\vec{n}_{ba}\rangle \tag{2.53}$$

This particular form of the vertex amplitude (2.52) is commonly used to study the semiclassical limit through the stationary phase approximation.

2.2 Restricted, semi-classical, Riemannian EPRL-FK model

Having defined the Spin(4) EPRL-FK spin foam state sum in the coherent state basis (2.50), we now turn to the challenges involved in evaluating this full expression. First, equation (2.50) includes a sum over all possible spin assignments to the faces $f \in \Delta$, resulting in a computationally demanding task whose complexity grows exponentially with the number of vertices in the triangulation Δ of the underlying manifold. In addition, the vertex amplitude (2.51) is highly nontrivial to evaluate, as the integrand involves rapidly oscillating exponentials. These two features, make the full evaluation of the state sum (2.50) extremely challenging. For this particular state sum, full numerical computations have only recently been performed, and only for small numbers of spins within restricted configurations [71]. Although significant progress has been

made in understanding the structure and behavior of individual vertex amplitudes in spin foam models [19, 20, 21], little is known about the full spin foam path integral. At present, most amplitude computations rely on semiclassical approximations, which make closed-form expressions more tractable [17]. Even in this regime, however, this approximations remain computationally expensive, as it still requires summing over a large number of variables. To gain further insight into the behavior of the full state sum (2.50), various simplifications have been proposed in the literature, tailored to address particular issues on different aspects of the theory. First, one can exploit the freedom in choosing the discretization of the underlying manifold. While we have primarily focused on the standard triangulation approach, alternative discretization schemes have also been explored [34, 72]. In particular, regular cellular decompositions such as cubulations provide a symmetric combinatorial setting. These discretizations have proven especially useful for renormalization studies, as they offer a more natural framework for applying coarse-graining techniques [73]. Second, one can restrict the spin foam state sum to a specific subset of coherent intertwiners, effectively limiting the path integral to a particular sector of the full theory. This restriction significantly reduces the number of degrees of freedom, making the model more tractable while retaining the key geometric features relevant to the particular analysis. Finally, one can study the semiclassical limit of the model, which corresponds to taking large spin values j (i.e., large area eigenvalues [74]). In this regime, the vertex amplitude can be approximated using the stationary phase method [17, 18]. This approach captures the leading-order contributions to the path integral where it is expected to connect to discrete classical gravity, described by Regge calculus [75]. Accordingly, this regime provides a setting in which to test the consistency of spin foam models with classical general relativity. Despite significant progress in this direction, several open issues remain. One prominent problem is the so-called *cosine problem* [76], where the semiclassical approximation yields a cosine of the Regge action instead of the expected single exponential. Another challenge is the *flatness problem* [77, 78, 79, 80], which arises when studying triangulations involving internal triangles (rather than a single 4-simplex). In such cases, constraints arising in the semiclassical limit lead the curvature to vanish, potentially constraining the model from reproducing non-trivial geometries. An additional issue occurs in the semiclassical limit, where *degenerate geometries* [18] also take part on the contributions to this regime. The physical interpretation and relevance of these contributions to the full spin foam path integral remain unclear and are the subject of ongoing investigation.

Following the above insights, we propose some simplifications of the state sum (2.50). Thus, for the present work, we introduce the following restrictions on the aforementioned state sum as follows:

- **Hypercubic combinatorics**

  We choose the 2-complex to be dual to a 4D cubulation. This choice offers the advantage of a regular combinatorial structure: for instance, each face is bounded by four edges, and each edge is 6-valent. While the original motivation for working in this setting was to simplify the coarse-graining procedures required for renormalization studies [73], here it will also prove useful in establishing a connection between our model and lattice field theory [36], as will be discussed in the following chapter .

- **Restriction to Quantum cuboid intertwiners**

  A significant development in the spin foam approach is the realization that intertwiners ι_e admit a geometric interpretation in terms of classical polyhedra embedded in $\mathbb{R}^3$ [69]. These polyhedra are most commonly taken to define tetrahedra, which serve as the fundamental building blocks of the triangulation Δ. Nevertheless, spin foam models with hypercubic combinatorics also exist. These models are generally more intricate than those defined on (dual) triangulations, due to the increased amount of data required to specify their geometric structures. For example, a vertex in a hypercubic complex is bounded by eight edges and 24 faces, in contrast to the five edges and ten faces of a vertex dual to a 4-simplex. This added complexity, is then counteracted by only allowing specific coherent intertwiners that are peaked on a cuboid [34] or a frustum shape [72]. These choices also restrict the space of representations, reducing the complexity of the model further. In the present work, we adopt this strategy by restricting to the class of quantum cuboids intertwiners which are *peaked* on cuboidal geometries [34]. This choice significantly simplifies the spin foam state sum (2.50), making the summation over states substantially more manageable. While this restriction constitutes a drastic approximation of the full theory (which does not allow for curvature [34]), the resulting model remains sufficiently rich to explore several open questions, including the role of matter couplings in spin foam models.

- **Semiclassical approximation of the vertex amplitude**

  The restriction to cuboidal intertwiners leads to a significant simplification of the spin foam state sum (2.50). Nevertheless, the exponential computational complexity of the model persists [71]. To extract meaningful insights into the behavior of the path integral under these restrictions, we will replace the corresponding vertex amplitude of the restricted model by its approximation on the semiclassical regime. This corresponds to take the limit on the vertex amplitude where $j \to \infty$. In this limit, the path integral admits a closed-form expression that is more tractable computationally, enabling explicit evaluation of the system.

We begin the construction of our restricted spin foam model by introducing the quantum cuboid intertwiners. In a later subsection, we will also discuss the semiclassical approximation of the vertex amplitude within this restricted setting.

2.2.1 Cuboid intertwiners

We start this subsection by recalling the definition of the *Livine–Speziale* coherent intertwiners (see equation (2.47)) [69] :

$$|\iota\rangle = \int_{SU(2)} dg\, g \triangleright \bigotimes_{i=1}^{3} |j_i, \vec{n}_i\rangle. \tag{2.54}$$

The geometric interpretation of this object is that of a polyhedron, with face areas j_f and face normals $\vec{n}_i$. It can be shown that the state sum model (2.50) can be written solely as an integral over coherent polyhedra, i.e. having closing normals [81].

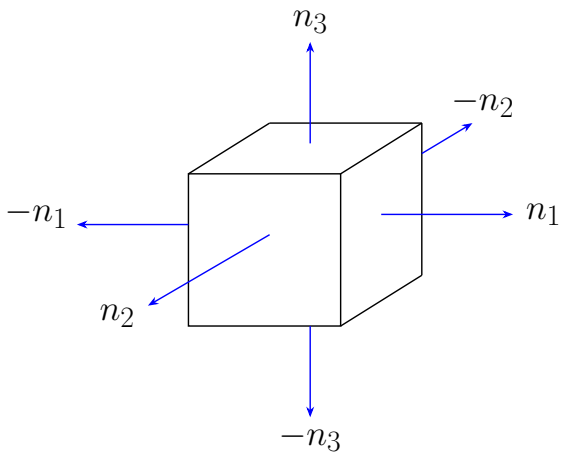

Figure 2.3: The shape of a cuboid is encoded in the areas of its faces j_i and the the outward pointing normal vectors.

Our goal now is to define (2.54) in the specific case of a cuboid. This can be achieved by noting that when the discretization of the manifold $\mathcal{M}$ is given by a cubulation, the corresponding 2-complex has the property that each edge is shared by six faces, corresponding to the six faces of a cube (see Figure 2.3). Consequently, every intertwiner appearing in the state sum will be six-valent and can thus be interpreted as a coherent polyhedron with six faces. A classical cuboid is characterized by its three edge lengths, or equivalently, by three independent face areas, each pair of opposite faces having equal area, and by face normals that are equal in magnitude and opposite in direction. Additionally, all internal angles are $\frac{\pi}{2}$ (see Figure 2.3). Imposing such regular cuboid geometry on all dual edges of the spin foam lattice introduces a

high degree of symmetry into the model. Specifically, the area, and hence the spin assigned to any pair of opposite faces related by a translation perpendicular to those faces must be equal. As a result, a quantum cuboid intertwiner is labeled by three independent spins and is defined as:

$$|\iota_{j_1,j_2,j_3}\rangle = \int_{SU(2)} dg\, g \triangleright \bigotimes_{i=1}^{3} |j_i, e_i\rangle |j_i, -e_i\rangle. \tag{2.55}$$

Here $e_1 = \exp(-i\frac{\pi}{4}\sigma_2) \triangleright e_3$, $e_2 = \exp(i\frac{\pi}{4}\sigma_1) \triangleright e_3$, and e_3 are taken to be unit vectors in $\mathbb{R}^3$.
A hypercuboid built from eight such cuboid intertwiners then depends on six representations due to the symmetry of each cuboid intertwiner, see Figure 2.4.

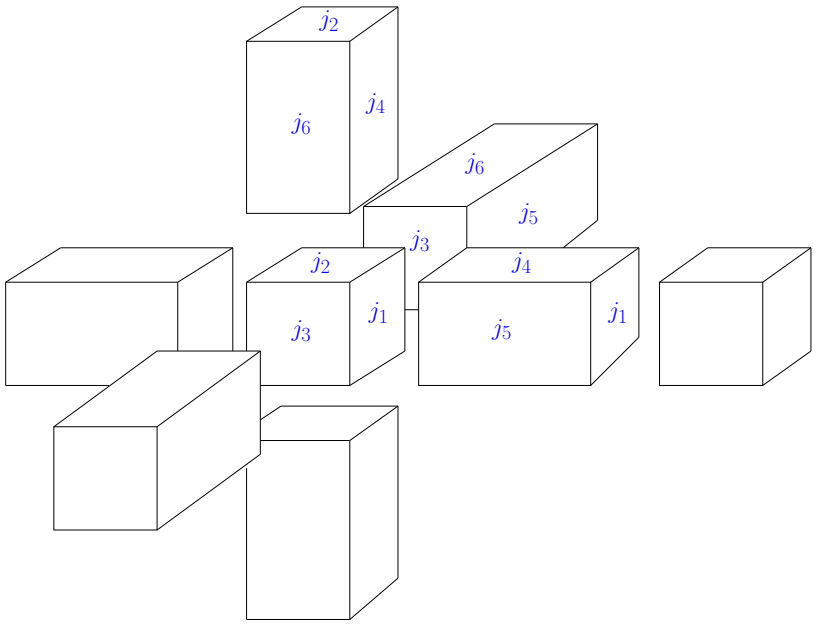

Figure 2.4: The boundary of a 4D cuboid consists of eight three-dimensional cuboids, which are glued together along faces of equal area. Due to the symmetry of the cuboid geometry, where opposite faces have identical areas, each configuration is fully determined by six independent spins (or face areas).

2.2.2 Spin foam sum with quantum cuboid intertwiners

The constructions discussed in the previous sections are now employed to define our restrcited model, namely the 4D Riemannian EPRL spin foam state sum with Barbero–Immirzi parameter $\gamma < 1$, restricted to quantum cuboid intertwiners.
The full state sum is given by (2.50). This sum can be succinctly expressed as:

$$Z_\Gamma = \sum_{j_f, \iota_e} \prod_f A_f \prod_e A_e \prod_v A_v, \tag{2.56}$$

where A_f, A_e and A_v are the face-, edge- and vertex-amplitude functions. This sum represents the full theory and must be performed over all spins, as well as over an orthonormal basis of intertwiners at each edge. It is at this stage that we implement our **restricted** spin foam model by considering only the quantum cuboid intertwiners defined in eq. (2.55). As a result, in our model, the sum over intertwiners ι in eq. (2.56) is no longer performed.

The allowed spins j_f in the Riemannian EPRL-FK model are constrained such that both $j_f^\pm := \frac{1\pm\gamma}{2} j_f$ are also spin values, i.e., half-integers. Common choices for the face amplitude include $A_f = 2j_f + 1$ and $A_f = (2j_f^+ + 1)(2j_f^- + 1)$. In [34], a more general approach was proposed that interpolates between these two choices by introducing an additional parameter $\alpha \in \mathbb{R}$, which plays an important role in the renormalization analysis of the spin foam state sum [73]. Following this approach, we define the face amplitude as:

$$A_f = \Big((2j_f^+ + 1)(2j_f^- + 1)\Big)^\alpha, \tag{2.57}$$

and investigate how different values of the parameter α affect the behavior of the state sum. In our formulation, the edge amplitudes A_e are defined as the norm of the coherent cuboid intertwiners $A_e = ||\iota_e||^{-2}$.

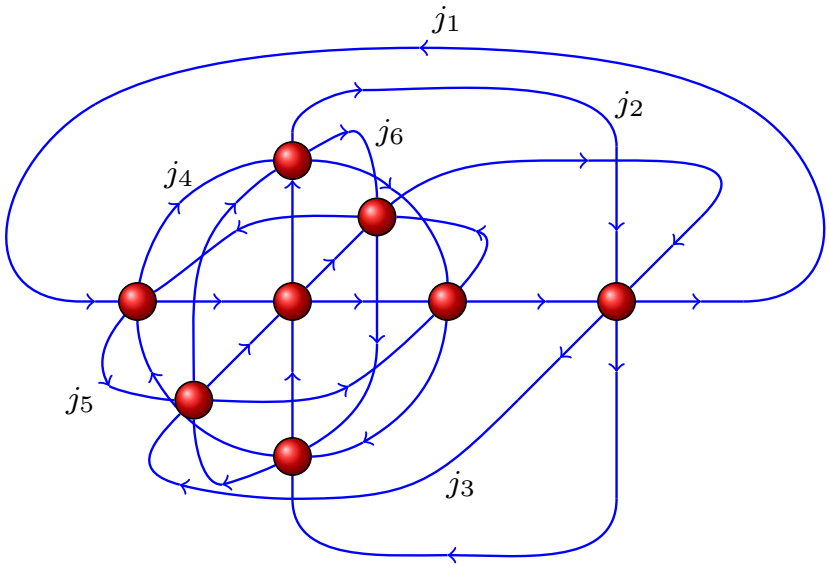

Figure 2.5: Spin network graph for a spin foam vertex with the combinatorics of a dual 4d hypercube.

As discussed in subsection 2.1.7 , the central ingredient of the spin foam state sum is the vertex amplitude A_v given in equation (2.51). As mentioned above, in our restricted model,

this amplitude is modified by constraining the sum over intertwiners such that only quantum cuboids, as defined in (2.55), are allowed. Thus, this amplitude can obtained by the evaluation of the spin network in Figure 2.5. For coherent boundary data, it reads:

$$\begin{aligned} A_v := &\int_{SU(2)^8} \prod_{a=1}^{8} dg_a^+ \prod_{a<b} (\langle -\vec{n}_{ba}|(g_b^+)^{-1} g_a^+ |\vec{n}_{ab}\rangle)^{2j_{ab}^+} \times \\ &\times \int_{SU(2)^8} \prod_{a=1}^{8} dg_a^- \prod_{a<b} (\langle -\vec{n}_{ba}|(g_b^-)^{-1} g_a^- |\vec{n}_{ab}\rangle)^{2j_{ab}^-} \\ &= A_v^+ A_v^- \quad , \end{aligned} \tag{2.58}$$

here, the indices a, b label the intertwiners in the spin network, and there is one group integration per intertwiner. Each link connecting two intertwiners contributes an inner product of coherent states, labeled by their associated normal vectors. Specifically, $\vec{n}_{ab}$ denotes the unit normal vector to the face shared between polyhedra a and b, as seen from polyhedron a, and $\vec{n}_{ba}$ vice versa.

In (2.58) we can exponentiate the inner products to write succinctly :

$$A_v^\pm = \int_{SU(2)^8} dg_a^\pm \, e^{S^\pm} \tag{2.59}$$

with the complex action

$$S^\pm := \frac{1 \pm \gamma}{2} \sum_{a<b} 2j_{ab}^\pm \ln \langle -\vec{n}_{ba}|(g_b^\pm)^{-1} g_a^\pm |\vec{n}_{ba}\rangle \tag{2.60}$$

Thus, the action $S^\pm$ encode the essential information contained in the vertex amplitude. Equation (2.59) constitutes one of the main ingredients in the model we study in this project. In the next subsection, we investigate the semiclassical limit of this amplitude.

2.2.3 Semi-classical approximation of amplitudes

As outlined in the introduction to this section, evaluating the vertex amplitude (2.58) remains computationally expensive due to the exponential complexity of the summation and the highly oscillatory nature of the group integrations. To address this challenge, we restrict our analysis to the semiclassical regime of the vertex amplitude and investigate its connection to classical gravity.

We begin by presenting the semiclassical approximation of (2.58), which is obtained via the stationary phase method. This technique allows us to obtain the the dominant contributions to the amplitude in the limit $j \to \infty$. The method proceeds as follows [17, 82]: let $D \subset \mathcal{M}$ be

a compact region of a smooth manifold, and let $S, f \in C^\infty(D, \mathbb{C})$ be smooth complex-valued functions defined on D, where we additionally require that $\mathrm{Re}(S) \leq 0$. Then we define:

$$A(\lambda) := \int_D dx\, f(x)\, e^{\lambda S(x)} \ , \tag{2.61}$$

we denote by H the $n \times n$ Hessian matrix of S and assume that the stationary points $\{x_0 \in D \,|\, \mathrm{d}_{x_0} = 0\}$ of S are isolated and non-degenerate, i.e. $\det(H_{x_0}) \neq 0$. A critical point of S is defined as a stationary point x_0 such that $\mathrm{Re}(S(x_0)) = 0$. If S has no critical points, then A is exponentially suppressed. On the other hand, if S has isolated critical points, then each critical point x_0 contributes to A by a term proportional to $\lambda^{-n/2}$. For large λ the asymptotic expansion of A yields for each critical point:

$$f(x_0) \left(\frac{2\pi}{\lambda}\right)^{\frac{n}{2}} \frac{1}{\sqrt{\det(-H)}}\, e^{\lambda S(x_0)} \left(1 + \mathcal{O}\left(\frac{1}{\lambda}\right)\right) \ . \tag{2.62}$$

This scheme can be applied to approximate the amplitudes (2.59) for large j_l. In this approach, the critical and stationary points are derived by varying the action (2.60) with respect to the dynamical variables, i.e, group elements, and enforcing that $\mathrm{Re}S^{\pm} = 0$. We start by noticing that in (2.59) one of the $N = 8$ integrations, is redundant due to the invariance of the Haar measure dg and can be absorbed into the other ones. As proved in [34], the remaining integrals have isolated critical points, and therefore they admit a stationary phase approximation. Furthermore, the action (2.60) is invariant under the exchange $g_a \to -g_a$ so, in total there is a 2^7-fold symmetry. Modulo this symmetry, there are two distinct stationary and critical points, satisfying the equations:

$$\tilde{n}_{ab} := g_a \triangleright \vec{n}_{ab} = -g_b \triangleright \vec{n}_{ba} \ , \tag{2.63}$$

for all links (ab), since the closure condition is satisfied automatically by the choice of quantum cuboids for any spin j_l. With the convention shown in Figure 2.4 and by fixing $g_0 = \mathbb{1}$, the two solutions Σ_1 and Σ_2 are shown in table 2.1.

According to (2.62), each critical stationary point $\vec{g}_c$ contributes one term of the form:

$$I = \sqrt{\frac{(2\pi)^{21}}{\det(-H(\vec{g}_c))}}\, e^{S(\vec{g}_c)} \ . \tag{2.64}$$

As reported in [34], the critical stationary points listed in Table 2.1 satisfy $S[\vec{g}_c] = 0$. This outcome arises from the restriction to quantum cuboid intertwiners as the only admissible

	Σ_1	Σ_2
g_1	$\exp(i\frac{\pi}{4}\sigma_1)$	$\exp(-i\frac{\pi}{4}\sigma_1)$
g_2	$\exp(i\frac{\pi}{4}\sigma_2)$	$\exp(-i\frac{\pi}{4}\sigma_2)$
g_3	$\exp(i\frac{\pi}{4}\sigma_3)$	$\exp(-i\frac{\pi}{4}\sigma_3)$
g_4	$\exp(-i\frac{\pi}{4}\sigma_3)$	$\exp(i\frac{\pi}{4}\sigma_3)$
g_5	$\exp(-i\frac{\pi}{4}\sigma_2)$	$\exp(i\frac{\pi}{4}\sigma_2)$
g_6	$\exp(-i\frac{\pi}{4}\sigma_1)$	$\exp(i\frac{\pi}{4}\sigma_1)$
g_7	$\exp(i\frac{\pi}{2}\sigma_1)$	$\exp(i\frac{\pi}{2}\sigma_1)$

Table 2.1: The two set of solutions corresponding the the stationary and critical points of the action (2.60). Note that the solutions correspond to rotations by $\frac{\pi}{2}$ except for g_7 which corresponds to a rotation by π.

intertwiners, which suppresses the excitation of local curvature. As a result, the leading contributions to the amplitude in equation (2.64) are governed by the determinant of the Hessian matrix H evaluated at the critical points. The Hessian is computed by introducing coordinates $\{X_a^I\}$ around each critical point $\vec{g}_c$ via $g_a = g_{a,c}\exp(i\sigma_I X_a^I/2)$. The entries of the Hessian matrix are given by:

$$\frac{\partial^2 S}{\partial X_a^I \partial X_a^I} = -\sum_{(ab)\supset a} \frac{j_{ab}}{2}\left(\delta_{IJ} - \tilde{n}_{ab}^I \tilde{n}_{ab}^J\right) \ , \tag{2.65}$$

$$\frac{\partial^2 S}{\partial X_a^I \partial X_a^I} = \frac{j_{ab}}{2}\left(\delta_{IJ} - i\epsilon_{IJK}\tilde{n}_{ab}^K - \tilde{n}_{ab}^I \tilde{n}_{ab}^J\right) \ , \tag{2.66}$$

where the vectors $\tilde{n}$ are defined as in (2.63). The Hessian is a 21×21 matrix and the determinant is given as follows:

$$\begin{aligned}\det H =& 2\Big[j_1^2(j_2+j_4)+j_2j_4(j_2+j_4)+j_1(j_2^2+(1+i)j_2j_4+j_4^2)\Big]\Big[j_1^2(j_3+j_5)+j_3j_5(j_3+j_5)\\ &+j_1(j_3^2+(1+i)j_3j_5+j_5^2)\Big]\Big[j_3j_4j_5+j_2(j_4j_5+j_3(j_4+j_5))\Big]\Big[j_2^2(j_3+j_6)+j_3j_6(j_3+\\ &j_6)+j_2(j_3^2+(1+i)j_3j_6+j_6^2)\Big]\Big[j_4^2(j_5+j_6)+j_5j_6(j_5+j_6)+j_4(j_5^2+(1+i)j_5j_6+j_6^2)\Big]\\ &\Big[j_3j_4j_6+j_1(j_4j_6+j_3(j_4+j_6))\Big]\Big[j_2j_5j_6+j_1(j_5j_6+j_2(j_5+j_6))\Big]\ .\end{aligned} \tag{2.67}$$

It turns out that the determinants of the two sets of solutions Σ_1 and Σ_2 are complex conjugate of each other, so that the whole amplitude is real. It is also worth noting that since $S[\vec{g}_c]=0$ on the critical stationary points for the quantum hypercuboid, then eventually, the Immirzi parameter γ appears only as an overall factor of the partition function. We can also readily see that $\det(\lambda j)=\lambda^{21}\det H(j)$, i.e. H is a homogeneous function of the spins. Putting together these insights, the amplitudes $\mathcal{A}^{\pm}{}_v$ satisfy on the large j limit:

$$\mathcal{A}_v^{\pm}\approx\left(\frac{1\pm\gamma}{2}\right)^{\frac{21}{2}}\mathcal{B}_v\quad,\quad \mathcal{B}_v=\left(\frac{2}{16\pi^2}\right)^7(2\pi)^{\frac{21}{2}}\left(\frac{1}{\sqrt{\det(-H)}}+\text{cc.}\right)\ , \tag{2.68}$$

where we also obtain one factor of $\left(\frac{2}{16\pi^2}\right)^7$ for each $SU(2)$ integration. In a similar way, it can be shown that in the large j-limit, the norm squared of the cuboid states (2.55) is given by:

$$||\iota_{j_1j_2j_3}||^2\sim\frac{8(1-\gamma^2)^{-\frac{3}{2}}}{(j_1+j_2)(j_2+j_3)(j_1+j_3)}\sim\mathcal{A}_e^{-1}(j_1,j_2,j_3)\ . \tag{2.69}$$

Similarly, the face amplitude reads:

$$\mathcal{A}_f\sim j_f^{2\alpha}\ . \tag{2.70}$$

Collecting these results, we obtain for the state sum, in the large j-limit on a regular hypercubic lattice, that

$$
\begin{aligned}
Z &\sim \left(\frac{1-\gamma^2}{4}\right)^{\alpha F-\frac{3}{2}E+\frac{21}{2}V} \sum_{j_f}\prod_f j_f^{2\alpha}\prod_e (j_1+j_2)(j_2+j_3)(j_1+j_3)\prod_v \mathcal{A}_v^2 \\
&=: \left(\frac{1-\gamma^2}{4}\right)^{6\alpha-\frac{9}{2}V} \sum_{j_f}\prod_v \widehat{A}_v \ ,
\end{aligned}
\tag{2.71}
$$

where F, E, V represent the total number of faces, edges and vertices respectively. We have also defined in the last line the dressed vertex amplitude $\widehat{A}_v$, where the face and edge amplitudes have been absorbed in a way that the boundary amplitudes are taken appropriately, since in a hypercuboid lattice it holds $V = \frac{F}{6} = \frac{E}{4}$. We can now note explicitly that in (2.71) the only dependence on the Barbero-immirzi parameter γ appears only as a prefactor in the partition function.

2.2.4 From spins to lengths

We now study the relationship between spins and edge lengths in the semiclassical approximation within our hypercubic lattice. In this regime, our setting admits a natural geometric interpretation of the restricted state sum. In the large-j limit, quantum cuboids approach classical cuboids, as illustrated in Figure 2.3, and are fully characterized by their three face areas. The condition that opposite faces have equal areas propagates through the hypercubic lattice: since adjacent hypercuboids share a cuboid, this constraint extends across neighboring cells. As a result, a given face area is preserved along directions orthogonal to the orientation of each face, creating a translation pattern throughout the lattice. Furthermore, a semiclassical configuration is described by an assignment of areas $a = j\ell_{\mathrm{P}}^2$ (where ℓ_{P} is the Planck length) to the faces of the hypercubic lattice. Two such face areas must coincide whenever the corresponding faces are parallel and related by a translation orthogonal to their plane. In the 4D lattice, we label the directions by x, y, z, t, and index the hypercubes by $\vec{n} \in \mathbb{Z}^4$. The areas $a_{\mu\nu}^{\vec{n}}$ then satisfy the symmetry condition:

$$
a_{\mu\nu}^{\vec{n}+pe_\rho+qe_\sigma} = a_{\mu\nu}^{\vec{n}}, \tag{2.72}
$$

where μ, ν, ρ, σ are all distinct directions, e_ρ and e_σ are unit vectors in the ρ- and σ-directions respectively, and $p, q \in \mathbb{Z}$. Dual to each vertex $\vec{n}$ of the lattice there is a *semiclassical quantum hypercuboid*, which is characterized by six independent areas $a_{xy}^{\vec{n}}, a_{xz}^{\vec{n}}, \ldots, a_{zt}^{\vec{n}}$. In contrast, a classical hypercuboid in $\mathbb{R}^4$ is determined by only four edge lengths. Therefore, there are two excess degrees of freedom in the quantum description. This redundancy arises because the six areas determine the three face areas of each 3D cuboid comprising the boundary of the 4D hypercuboid. In turn, for each such 3D cuboid, the three areas determine three edge lengths.

However, for the 4D structure to correspond to a *geometric* hypercuboid, not only must the shared areas between adjacent 3D cuboids match, but the corresponding edge lengths of each shared rectangle must also agree. This requirement imposes additional constraints on the areas. These conditions can be expressed as:

$$a_{xy}a_{zt} = a_{xz}a_{yt} = a_{xt}a_{yz}. \tag{2.73}$$

At the level of spins these condition define the so-called *geometricity* constraints (see Figure 2.4) :

$$j_1 j_6 = j_2 j_5 = j_3 j_4 \tag{2.74}$$

When these *geometricity* conditions are imposed, one can go from areas to edge lengths in the path integral (2.71). In the semi-classical limit the representation labels of the vertex amplitude (2.71) are uniformly scaled up . In this limit, the discreteness of representations is barely noticeable and we approximate them as continuous variables [34]. As discussed in [73], since originally the integrations were carried over all spins in the path integral, this effectively gauge fixes the redundant spins. A way to account for this is by including a Fadeev-Popov determinant (FPD). In a next step, a Jacobian is included to take into account the change of variables from the four remaining spins j_1, j_2, j_3, j_4 to four edge lengths x, y, z, t. The final FPD is given by:

$$\Delta = \frac{J}{cos\theta} \tag{2.75}$$

where

$$J = \left| \det \frac{\partial(j_1, j_2, j_3, j_4)}{\partial(x, y, z, t)} \right| = xy^2z \tag{2.76}$$

and

$$\cos\theta = \frac{j_1^2 j_2^2}{\sqrt{j_1^4(j_2^2+j_3^2)(j_2^2+j_4^2) + j_3^4(j_1^2+j_2^2)(j_2^2+j_4^2) + j_4^4(j_1^2+j_2^2)(j_2^2+j_3^2)}} \tag{2.77}$$

Eventually, due to the regular combinatorics, it is possible to combine face, edge and vertex amplitudes as well as Jacobian and Fadeev-Popov determinant into a common amplitude that we define as $\tilde{\mathcal{A}}$, which is a homogeneous function of degree $24\alpha - 14$:

$$\tilde{\mathcal{A}}(\{\lambda l_i\}) = \lambda^{24\alpha-14}\tilde{\mathcal{A}}(\{l_i\}) \ , \tag{2.78}$$

and the spin foam partition function (2.71) can be written as a function of the lengths of the lattice as:

$$Z_{SF} = \int \prod_i dl_i \prod_v \tilde{\mathcal{A}}_v(\{l_i\}) \ . \tag{2.79}$$

Thus, in this partition function, one integrates over all possible length assignments to the 2-complex, which are weighted by the spin foams amplitudes. This partition function will play a main role in the computations of the model. Given that $\tilde{A}_v(\{l_i\})$ is positive and non-oscillatory, then it can be used to define a probability distribution (after dividing by Z). Thus, Markov Chain Monte Carlo techniques can be employed for the evaluation of this partition function. We will cover how this is achieved in the next chapter.

This concludes our review of the spin sum restricted to quantum cuboid intertwiners and the semiclassical limit of the amplitudes. We now have the necessary components to investigate the coupling of the scalar free field, defined on an irregular hypercubic lattice (discussed in Chapter 1), with our restricted spin foam model in the semiclassical limit. The partition function (2.79) will subsequently define the hypercubic lattice on which the free field can be defined "on top". In the next chapter, we will explore how to achieve this task and address the computational challenges involved in the numerical evaluation of our model. We will also place significant emphasis on the definition of meaningful observables pertaining to our model.

Chapter 3

Scalar Matter Coupled to Spin Foams

This chapter builds upon the free massive scalar field defined on irregular discretizations from Chapter 1 and our restricted spin foam model introduced in Chapter 2. First, we define the coupling of the free massive scalar field to our restricted spin foam model and define expectation values of geometric and matter observables. Second, in the quantum gravity regime, as in classical General Relativity, one encounters the challenge of defining *meaningful* observables, as diffeomorphism-invariant quantities are not available. To address this, we propose a *relational* correlation function of the matter field, which admits a diffeomorphism-invariant interpretation and serves as a viable test observable in this background-independent setting. Finally, we outline the framework for the numerical evaluation of our model and present the numerical results of the evaluation of matter and geometric observables along the *relational* correlation function.

3.1 Scalar matter field coupled to restricted Spin Foam Model

We finally have the main ingredients to explore the coupling of a free massive scalar field to our restricted spin foam model. It is worth mentioning that a variety of approaches have been developed to include matter in loop quantum gravity and spin foam models. These include unification frameworks with enlarged symmetry groups encompassing both gravity and matter [22], and deparameterization strategies using matter fields as reference systems [23, 24, 25, 26]. In the present work, we follow a more conservative approach by coupling matter "on top" the spin foam background. Thus, the spin foam provides a (fluctuating) quantum spacetime on which matter degrees of freedom and their interactions are defined. This strategy has been employed to couple gauge fields [27, 28, 29, 30], fermions [31, 32], and scalar fields [33], with the latter derived from loop quantum gravity techniques and inspired by similar developments in loop quantum cosmology [83, 84]. Constructing such coupled systems is crucial for understanding

the interplay between quantum matter and geometry. This endeavor raises important questions across quantum gravity approaches, such as whether quantum gravity imposes constraints on the matter content of the universe, or whether it leads to significant modifications of matter dynamics. For instance, indications of such phenomena have been observed in the asymptotic safety scenario [85, 7, 86]. Despite the relevance of these questions, addressing them remains technically challenging due to the particular complexities of discrete settings. However, results in Causal Dynamical Triangulations show progress: for instance, coupling a scalar field has revealed matter-driven changes in spacetime topology [40, 87, 88]. In contrast, in spin foam models, the dynamics of coupled systems in the deep quantum regime remain barely explored, primarily due to the complexity of computing the fundamental amplitudes. However, certain aspects of the theory can still be tested in simplified scenarios, which could allow us to extract meaningful insights. This work aims to contribute to that direction by studying a restricted spin foam model in the semiclassical regime coupled to a free massive scalar field defined on an irregular discretization. In such a setting, one can directly compare spin foam predictions to those of lattice field theory and learn valuable lessons.

3.1.1 Partition function of the coupled system

In Chapters 1 and 2, we defined the two components of the coupled system explored in this Chapter: a free, massive scalar field on an irregular lattice (eq. (1.46)), and a restricted spin foam model in the semiclassical limit (eq. (2.79)), which describe superpositions of discrete flat spacetimes. Our coupling strategy is as follows: the scalar field action depends on various (dual) volumes associated with the underlying 4D hypercubic lattice. Given a spin foam state, that is, a specified configuration of edge lengths $\{l_i\}$, we treat the corresponding volumes in eq. (1.46) as functions of these lengths, thereby defining the discrete geometry on which the scalar field propagates. A similar coupling strategy was applied in [27] to incorporate Yang–Mills theory into the Barrett–Crane spin foam model [89]. In our case, we sum over all scalar field configurations and length configurations to define the total partition function. Importantly, we modify only the matter sector while keeping the gravitational sector unchanged, in analogy to minimal coupling in general relativity: the Einstein–Hilbert action remains unchanged, while the matter action acquires explicit dependence on the geometry. In our case, this dependency is encoded in the edge lengths of the spin foam.

It is important to note that coupling matter to spin foams is not unique. A key choice concerns the placement of matter degrees of freedom: either on the discretization itself (the cubulation) or on its dual 2-complex. For our setup, where the combinatorics of the cubulation and its dual coincide and periodic boundary conditions are imposed, this distinction is expected to have little effect on the dynamics. However, these choices define distinct theories, since matter

theories are generally not self-dual. Moreover, in spacetimes with boundaries, this decision influences the structure of the associated boundary Hilbert spaces.

Following [36], we choose to place the scalar field on the vertices σ_0 of the cubulation and derive the relevant volumes directly from the edge lengths V_{σ_1} defined by the spin foam. Primal volumes (e.g., edge lengths V_{σ_1} and hypervolumes V_{σ_4}) are computed from the cubulation itself, while dual volumes are determined analogously from the dual lengths. Since the dual of a hypercuboidal lattice is again hypercuboidal, we place the vertices of the dual lattice at the centers of the 4D hypercuboids. Dual edges connect the centers of adjacent hypercuboids, forming a regular dual cubulation.

Collecting the above insights, we define the partition function of the system as (see equations (1.46), (2.79)):

$$Z = \int \prod_i dl_i \int \prod_{a\in\sigma_0} d\phi_a \prod_{v\in\star\sigma_0} \tilde{A}_v(\{l_i\}_{i\in\sigma_4}) \exp\left(-\sum_{a,b} \phi_a K_{ab}(M,\{l_i\})\phi_b\right) \quad , \tag{3.1}$$

where we denote the edges of the cubilation by i and the vertices of the cubilation by a, b. σ_4 represent the hypercuboids and σ_0 are the vertices of the cubilation. M denotes the mass of the free massive scalar field.

3.1.2 Properties from regular lattices

To gain an initial insight into the partition function of the coupled system (eq. (3.1)), we consider a simplified scenario in which all edge lengths in the spin foam are equal, though they remain dynamical. This setup corresponds to a superposition of regular lattices with varying uniform length scales. As discussed in subsection 2.2.4, the spin foam vertex amplitude (eq. (2.79)) exhibits a scaling behavior proportional to $l^{24\alpha-14}$. Thus, after performing the Gaussian integrations over the scalar field for fixed l in eq. (3.1), we obtain the probability distribution[1] for the length l:

$$\frac{1}{Z}\frac{l^{N(24\alpha-14)}}{\sqrt{l^{2N}\left(\sum_{i=1}^{N} a_i l^{2i} M^{2i}\right)}} \quad , \tag{3.2}$$

where a_i are numerical factors that are not relevant for the scaling of the amplitude. In eq. (3.2), we observe two competing behaviors in the coupled system for sufficiently large α: the scalar field introduces a polynomial suppression of large edge lengths, which becomes stronger

[1] as we explain below, this probability distribution is well defined only after imposing lower and upper cutoffs on the lengths.

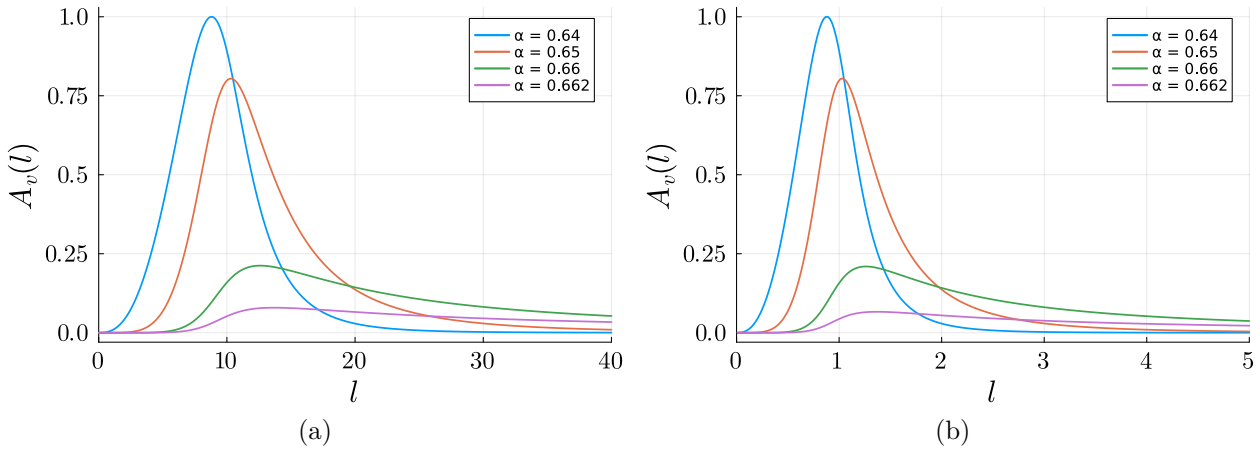

Figure 3.1: Amplitude (3.2) for different values of α in the region where the distribution remains finite. The peak shifts to larger lengths as α increases. The width of the distributions also increases rapidly for values beyond 0.66. In these plots, the amplitudes were normalized (arbitrarily) to the maximum value of the distribution with $\alpha = 0.64$. a) Lattice size $N = 10$, $M = 0.1$, b) Lattice size $N = 10$, $M = 1$.

with increasing mass M, while the spin foam amplitude, in contrast, increasingly favors larger lengths as α grows. This leads to two qualitative regimes:

- **Finite M, small α:** The suppression from the scalar field dominates (which is a polynomial in l and M). In this regime, the exponent of the numerator is smaller than any monomial in the denominator. This leads to a divergence as $l \to 0$ and small lengths prevail. To regulate this divergence, a lower cutoff needs to be introduced to perform numerical evaluations in this region. It is important to notice, that such small scales lie outside the regime of validity of the semiclassical approximation of the spin foam amplitude.

- **Finite M, large α:** In this case, the exponent of the numerator is larger than any in the denominator. Thus, the spin foam contribution dominates, and the amplitude diverges as $l \to \infty$; large lengths dominate. Accordingly an upper cut-off needs to be introduced for numerical evaluations in this region.

The structure of the denominator in the probability distribution further suggests the existence of an intermediate regime where lengths remain finite. For small l, the term with the smallest exponent dominates; for large l, the opposite holds. Tuning α to interpolate between these extremes, such that the exponent of the numerator is between the minimum and maximum exponents of the denominator, leads to a peaked distribution at finite l, with its position and width dependent on α and M, as shown in Figure 3.1.

From the functional form of the distribution in eq. (3.2), it is possible to estimate the range of α where finite lengths are expected. For small l, the distribution scales as $l^{N(24\alpha-15)-1}$, and for large l, as $l^{N(24\alpha-16)-1}$. Hence, for $N \gg 1$, thus, we expect a peak in the interval $\alpha \in \left[\frac{5}{8} \approx 0.625, \frac{2}{3} \approx 0.66\right]$. Although these considerations assume uniform lengths, they offer useful insight into how the dynamics shift when summing over irregular lattices with fully dynamical edge lengths.

3.1.3 Expectation values of Observables

Following [36], the expectation values of standard observables (as defined, for instance, in Lattice Field Theory) are defined in a similar manner as in statistical physics, where given an observable $\mathcal{O}(\{l_i\}, \{\phi_a\})$ the expectation value of $\mathcal{O}$ is defined as:

$$\langle \mathcal{O} \rangle = \frac{1}{Z} \int \prod_i dl_i \int \prod_{a \in \sigma_0} d\phi_a \, \mathcal{O}(\{l_i\}, \{\phi_a\}) \prod_{v \in \star\sigma_4} \tilde{\mathcal{A}}_v \, e^{-\sum_{a,b} \phi_a K_{ab} \phi_b}, \tag{3.3}$$

where we used a compact notation for the amplitude $\tilde{\mathcal{A}}(\{l_i\})$ and $\phi_a(\{l_i\}, M)$.
At first sight, there are two sets of observables that we can straightforwardly define: geometric and matter observables:

- **Geometric observables**
  For the spin foam, observables like the 4-volume V and individual lengths l_i are relevant as they are indicators of the scaling behavior of the coupled model. As suggested by the form of the distribution in eq. (3.2), divergent lengths occur for values beyond $\alpha \approx 0.66$. On the other hand, in our system the kinect term of the action scales with $\sim l^2$, while the potential part with $\sim M^2 l^4$. Thus, for small lengths, the contribution to the action gets smaller, with a more pronounced effect as the mass increases. Thus, an interesting interplay arises from these considerations and can be further explored through geometric expectation values.

- **Matter observables**
  The free massive scalar field is uniquely determined by its two-point correlation function (see eq. (1.4)), in non-dynamical, flat space-time. At first sight, this quantity can be studied as defined in eq. (3.3). Yet, due to the construction of our system (where no background is specified), the definition of such correlation function is more subtle. Consider the correlator $\langle \phi_a \phi_b \rangle$ on regular lattice in standard lattice field theory. In this setting, vertices a and b correspond to spacetime points, and their geodesic distance is well-defined via the discretization of a fixed background. This allows for a straightforward

computation of the correlation length from field correlations across the lattice. In contrast, spin foam models, being background-independent, lack a fixed geometric structure. Here, vertices a and b are merely labels without intrinsic spatial meaning, and their separation is not predetermined but integrated over as part of a superposition of geometries in the spin foam path integral. To construct a physically meaningful observable in this context, one must take into account both the field correlations and the dynamical nature of the distance between a and b. One of the central goals of this work is to address these challenges by introducing an alternative framework. Specifically, we propose a correlation function in *relation* to geodesic distances. This new object is defined and motivated in the following subsection.

3.1.4 Relational Observables

As discussed in the previous subsection, if we wish to measure *meaningful* observables in our coupled system, we must proceed differently. Consider the usual case in continuum quantum field theory (QFT), where the two-point correlation function (after a Wick rotation) is defined as:

$$\langle \phi(x)\phi(y)\rangle = \frac{1}{Z}\int \mathcal{D}\phi\, \phi(x)\phi(y)e^{-S[\phi]} \ . \tag{3.4}$$

If we include dynamical gravity in the continuum, we can formally write:

$$\langle \phi(x)\phi(y)\rangle = \frac{1}{Z}\int \mathcal{D}\phi\, \mathcal{D}g_{\mu\nu}\sqrt{\det g}\, \phi(x)\phi(y)\, e^{-S[\phi]}e^{-S_{EH}[g]}\,, \tag{3.5}$$

where S_{EH} is the Einstein-Hilbert action. Although one can write such formal expression, it does not carry any clear physical meaning. Firstly, $\phi(x)$ and $\phi(y)$ are not diffeomorphism-invariant objects, as they depend explicitly on the coordinate system of the underlying manifold. Moreover, the integration over all metrics does not uniquely define the *distance* between x and y, thus the correlator is effectively evaluated at a superposition of distances, resulting on correlations of fields as an average over distances. Thus, in this context, the above considerations undermine the usual interpretation of correlation functions in QFT. Therefore, a more general version of eq. (3.5) is required if we wish to define a *meaningful* correlation function in our coupled system. To address this challenge, several proposals have been developed for defining *meaningful* observables in background-independent approaches. A prominent framework is the notion of *relational observables* [42], which distinguishes between *partial observables*, quantities that can be measured but not predicted on their own, and *complete observables*, which represent physical predictions in the form of correlations between partial observables. For example,

the reading T of a clock and the position q of a particle are both partial observables: each can be individually measured, but neither is predictable without further information. A complete observable in this context would be the position of the particle *when* the clock reads a certain value $T = \tau$, i.e., $q(\tau)$. This correlation is something the theory can, in principle, predict. In a generally covariant context, where coordinate labels have no physical meaning, this shift to relational data becomes essential. Meaningful physical quantities arise not from evaluating a field at a fixed coordinate location (which is inherently diffeomorphism-dependent), but from specifying the value of one dynamical variable when another takes a given value. This idea can be formalized within classical general relativity through a general construction of complete observables [41]. In this approach, one introduces *clock variables*, frequently chosen to be scalar fields, to define *Dirac observables*[2] [90] as the value of a partial observable when the clocks assume specified values. This procedure guarantees gauge invariance, since both the partial observable and the clock transform identically under diffeomorphisms, rendering the resulting *relational* observable invariant. Thus, these concepts lead to a new way of constructing observables in GR: physically meaningful observables are inherently relational, encoding correlations among dynamical degrees of freedom without relying on a fixed background or absolute spacetime localization. In light of these ideas, we can take a similar approach to define a two-point correlation function on our investigations. Given that it makes little sense to talk about the behavior of $\langle\phi(x)\phi(y)\rangle$ as a function of the *coordinate* distance between x and y, since these quantities lack a diffeomorphism-invariant meaning, then a more appropriate notion is the **geodesic distance** $d_{g_{\mu\nu}}(x, y)$, where $g_{\mu\nu}$ represents the metric of a given geometry. Furthermore, since there is no canonical way to identify "the same two points" across a superposition of geometries, we instead sum over all pairs of points separated by a fixed geodesic distance R within each geometry, and then repeat this process across all geometries [40]. This leads us to define a diffeomorphism-invariant correlation function in relation to the geodesic distance R: $\langle\phi\phi(R)\rangle$. In the spirit of relational observables, we refer to this quantity throughout this work as the *relational correlation* function. In the continuum this takes the form:

$$\langle\phi\phi(R)\rangle := \frac{1}{Z}\int \mathcal{D}\phi\,\mathcal{D}g_{\mu\nu}\sqrt{\det g}\;\underbrace{\int_{\mathcal{M}} dx \int_{\mathcal{M}} dy}_{\substack{\text{integrate over}\\ \text{all coordinates } x,y}}\;\overbrace{\langle\phi(x)\phi(y)\rangle_{g_{\mu\nu}}}^{\substack{\text{correlator measured}\\ \text{in } g_{\mu\nu} \text{ at } x,y}}\; e^{-S[\phi]}e^{-S_{EH}[g_{\mu\nu}]}\;\underbrace{\delta(d(x,y)-R)}_{\substack{\text{geodesic distance}\\ \text{between } x,y}}, \tag{3.6}$$

[2]Dirac observables are phase space functions that commute with all first-class constraints and are thus invariant under the gauge symmetries of the theory, including spacetime diffeomorphisms in general relativity.

this definition has the advantage that no reference to coordinates is needed, and thus the expression is manifestly diffeomorphism-invariant. This feature is achieved by integrating (or averaging) over all pairs of points separated by a specific **geodesic distance**, as enforced by the delta function in (3.6).

For our particular coupled model, we can make the straightforward identifications in the discrete:

$$\mathcal{D}g_{\mu\nu} \longrightarrow \prod_i dl_i \quad \text{or} \quad \sum \text{ over finite set of length values}$$

$$\int dx \int dy \longrightarrow \sum_{\langle i,j \rangle} \text{sum over all pairs } \; i,j$$

$$\delta \longrightarrow \text{function analogous}$$

Therefore, for our coupled system, we define:

$$\langle \phi\phi(R) \rangle_\Delta := \frac{1}{Z} \int \prod_i d\phi_i \prod_k dl_k \sum_{\langle i,j \rangle} \underbrace{\langle \phi_i \phi_j \rangle}_{\substack{\text{correlator} \\ \text{defined for lengths } \{l_k\}}} \underbrace{\prod_v \tilde{\mathcal{A}}(\{l_k\})}_{\substack{\text{SF semiclassical} \\ \text{amplitude}}} e^{-\sum_{a,b} \phi_a K_{ab} \phi_b} \underbrace{\delta(d(i,j) - R)}_{\substack{\text{geodesic distance} \\ \text{between vertices } i,j}} \tag{3.7}$$

Our proposed correlator in eq. (3.7) can be investigated explicitly numerically for our coupled system. The next subsections will mostly be concerned with the numerical evaluation of this object.

3.2 Numerical results

In this subsection, we present the explicit evaluation of geometric and matter observables as defined in the previous subsections. The results presented below are entirely based on the dataset from [36], which is archived on Zenodo, with the associated code publicly available via the corresponding GitHub repository. Both the dataset and code links are provided in the references for [36] in this work.

Firstly, to start the presentation of numerical results, we revisit the study of geometric observables, building directly on the results reported in [36]. Next, on the matter side, we also revisited the two-point correlation function presented in [36]. In that work, the two-point correlation function was evaluated with a different numerical strategy as the one we present here (which we discuss thoroughly in the subsections below). Thus, our approach aims to extract

additional insights from the same underlying data. Beyond this reanalysis, we also present, for the first time, a numerical evaluation of the *relational correlation* function defined in (3.7), which extends the scope of previous investigations. Thus, in this section, we discuss in detail the differences and novel results from the expectations values we compute in this work and those reported in [36].
In [36], the partition function of the coupled system (eq. (3.1)) was evaluated using Markov Chain-Monte Carlo methods [43], which we briefly outline below. A detailed description of the simulation techniques can be found in the original work.

3.2.1 Setup of numerical simulations

In [36] a Metropolis–Hastings Markov Chain Monte Carlo [91] algorithm was employed to sample configurations of edge lengths $\{l_i\}$ and scalar field values $\{\phi_a\}$ according to the joint distribution (see eq. (3.1)):

$$P(\{l_i\},\{\phi_a\}) = \frac{1}{Z}\prod_{v\in\star\sigma^4}\tilde{A}_v(\{l_i\})\,\exp\left(-\sum_{a,b}\phi_a K_{ab}(M,\{l_i\})\phi_b\right), \tag{3.8}$$

the sampling procedure alternates between geometry and field updates. Geometry updates were performed by randomly selecting a hypercuboid and rescaling its four edge lengths according to:

$$l_i^{\text{new}} = r_i \cdot l_i^{\text{old}}, \qquad r_i \in \mathcal{U}(0.5, 2.0), \tag{3.9}$$

where $\mathcal{U}$ denotes the uniform distribution. Scalar field updates are performed locally, by proposing additive changes to individual vertex values:

$$\phi^{\text{new}} = \phi^{\text{old}} + r, \qquad r \in [-\delta, \delta], \tag{3.10}$$

with δ tuned to maintain an acceptance rate between 40% and 60%. The acceptance or rejection of each proposal is determined by the usual Metropolis criterion, based on the change in the full joint action. As commented in subsection 3.1.3, to prevent divergences, cutoffs on the edge lengths are introduced $l_{\min} = 5 \times 10^{-5}$ $l_{\max} = 10^4$, respectively.
Thermalization of the Markov chain was assessed by monitoring observables such as the total 4D volume and the full spin foam amplitude. A burn-in phase was discarded to eliminate dependence on initial conditions. To mitigate correlations between successive samples, subsampling was performed at intervals determined by the autocorrelation length, which depends

on the lattice size and model parameters.
The simulations were conducted on three hypercuboidal lattice configurations with periodical boundary conditions and a number of vertex:

$$N_1 = 3^4 = 81, \qquad N_2 = 4^4 = 256, \qquad N_3 = 5^4 = 625\,. \tag{3.11}$$

where N_i refers to the total number of vertices in each lattice. For each configuration, different scalar field masses were used: for N_1, $M \in \{0.5, 5, 50\}$; for N_2, $M \in \{5, 50\}$; and for N_3, $M \in \{0.5\}$. In all cases, the parameter α (see eq. (2.57)) was varied within the range [0.61,0.7] in steps of 0.001. Due to increased autocorrelation and computational cost with larger lattices, the number of samples was set to 5000 for N_1 and N_2, and 2000 for N_3.

3.2.2 Geometric observables

In [36], the expectation value of the total volume $\langle V \rangle$, as defined in (3.3), was computed using lengths sampled from the distribution (3.15). That work also presents the corresponding histogram of the sampled lengths across all four directions in the lattice. In the present study, we revisit both analyses, but we introduce some modifications to the treatment of the data. These new treatment will provide new perspectives on the underlying geometric structure, as we detail in the subsections below.

3.2.2.1 Total volume

As shown in the analysis of regular lattices (see eq. (3.2)), there exists a range of the parameter α for which the total volume $\langle V \rangle$ is expected to remain finite. This regime corresponds to configurations where the sampled edge lengths are themselves finite. Figure 3.2 shows $\langle V \rangle$ as a function of α for the three lattice sizes N_1, N_2, and N_3. In all cases, we observe a similar qualitative behavior, independent of the mass and lattice size. For $\alpha < 0.63$, the total volume remains close to the minimum set by the lower cutoff on edge lengths, while for $\alpha > 0.67$, it approaches the maximum allowed by the upper cutoff. Thus, both regimes are cutoff-dependent and therefore do not reflect the true dynamics of the system. However, they indicate that for small α, the lattice tends to minimize edge lengths, whereas for large α, it favors configurations with maximal lengths, as discussed in subsection 3.1.3. Finally, we observe that the regime where $\langle V \rangle$ is finite and cutoff-independent lies approximately within the range $[\alpha \approx 0.63, \alpha \approx 0.67]$. Therefore, we restrict the rest of our analysis to this interval.

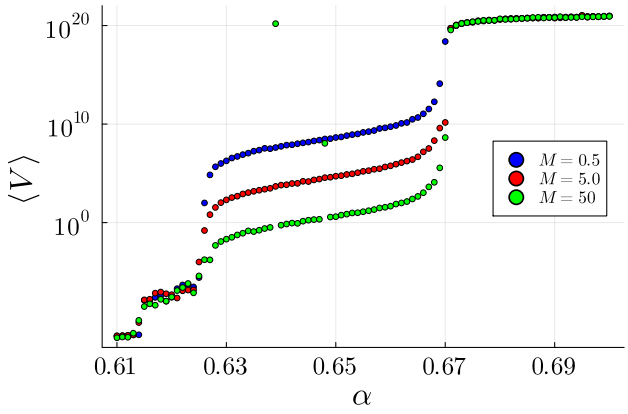

(a) Lattice size $N_1 = 81$

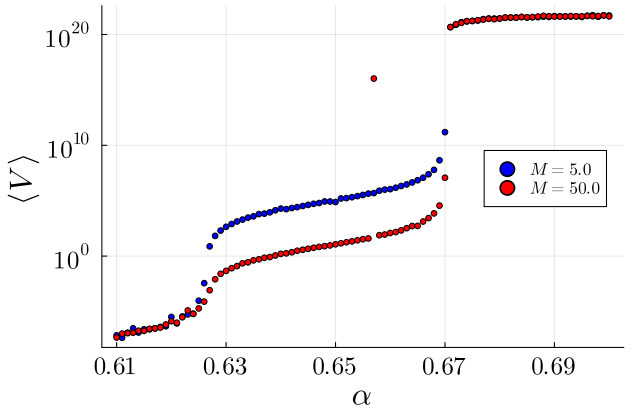

(b) Lattice size $N_2 = 256$

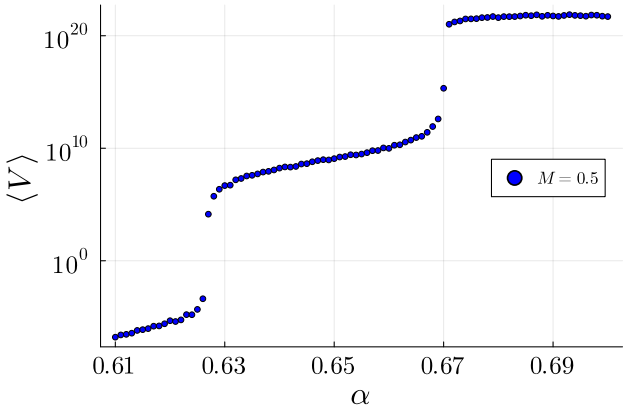

(c) Lattice size $N_3 = 625$

Figure 3.2: $\langle V \rangle$ as function of α for different lattice sizes N_1, N_2 and N_3.

3.2.2.2 Distribution of edge lengths

We now examine the distribution of lengths across the three hypercubic lattices N_1, N_2 and N_3 within the range of α at which the total volume remains finite: $\alpha \in [0.63, 0.67]$.
This analysis investigates the frequency with which a given length value l occurs across the edges in all spacetime directions within the lattice. In [36], this analysis is represented through histograms depicting the frequency of l for various lattice sizes and α values.
In our study, we introduce a different aspect to this analysis that does not rely solely on the classification of the data in histograms. Our approach is motivated by a subsequent stage of this work (thoroughly discussed in the following subsections), where we aim to measure geodesic distances R, defined as the sum of n edge lengths. To achieve this, it is essential to

implement a binning strategy that groups length values within the range $[l, l+\delta l]$. Without this strategy, it is not possible to generate an accurate statistic of the sampled lengths, since even small numerical differences between length values could result in artificially sparse statistics. This issue arises particularly when employing a naive approach that classifies length values by rounding them to a fixed number of decimal places, which is found to be too coarse and inflexible for precise data classification. In contrast, binning enables explicit control over the resolution at which two lengths are considered statistically indistinguishable. In practice, we tuned this minimum resolution to smooth the otherwise spare statistics. These results are shown in Figures 3.3, 3.4 and 3.5. As the qualitative behavior is consistent throughout the interval $\alpha \in [0.63, 0.67]$, we present representative results for $\alpha = 0.63, 0.64, 0.65, 0.66$. In these plots, the distributions exhibit a clear peak at finite length and share a qualitatively similar shape: a smooth, asymmetric profile with a sharp drop-off at short lengths and a tail toward larger values, consistent with the analytical results in subsection 3.1.2. This indicates that, in the plateau region of $\langle V \rangle$ (see figure 3.2), the system is sharply peaked around a characteristic length, which we interpret as an emergent regular lattice geometry with small perturbations.
Quantitatively, increasing the scalar field mass M shifts the peak of the distribution to shorter lengths approximately linearly. In contrast, increasing α (with M and lattice size fixed) moves the peak to larger lengths and broadens the tail. Although the tail appears shorter than predicted analytically, this may be due to limited sample sizes at low probability regions.
Finally, we can compare different lattice sizes. Keeping M and α fixed, the peak location remains largely unchanged, suggesting it is primarily determined by these parameters. However, larger lattices exhibit more sharply peaked distributions and shorter tails, possibly due to increased constraints or under-sampling of rare configurations.

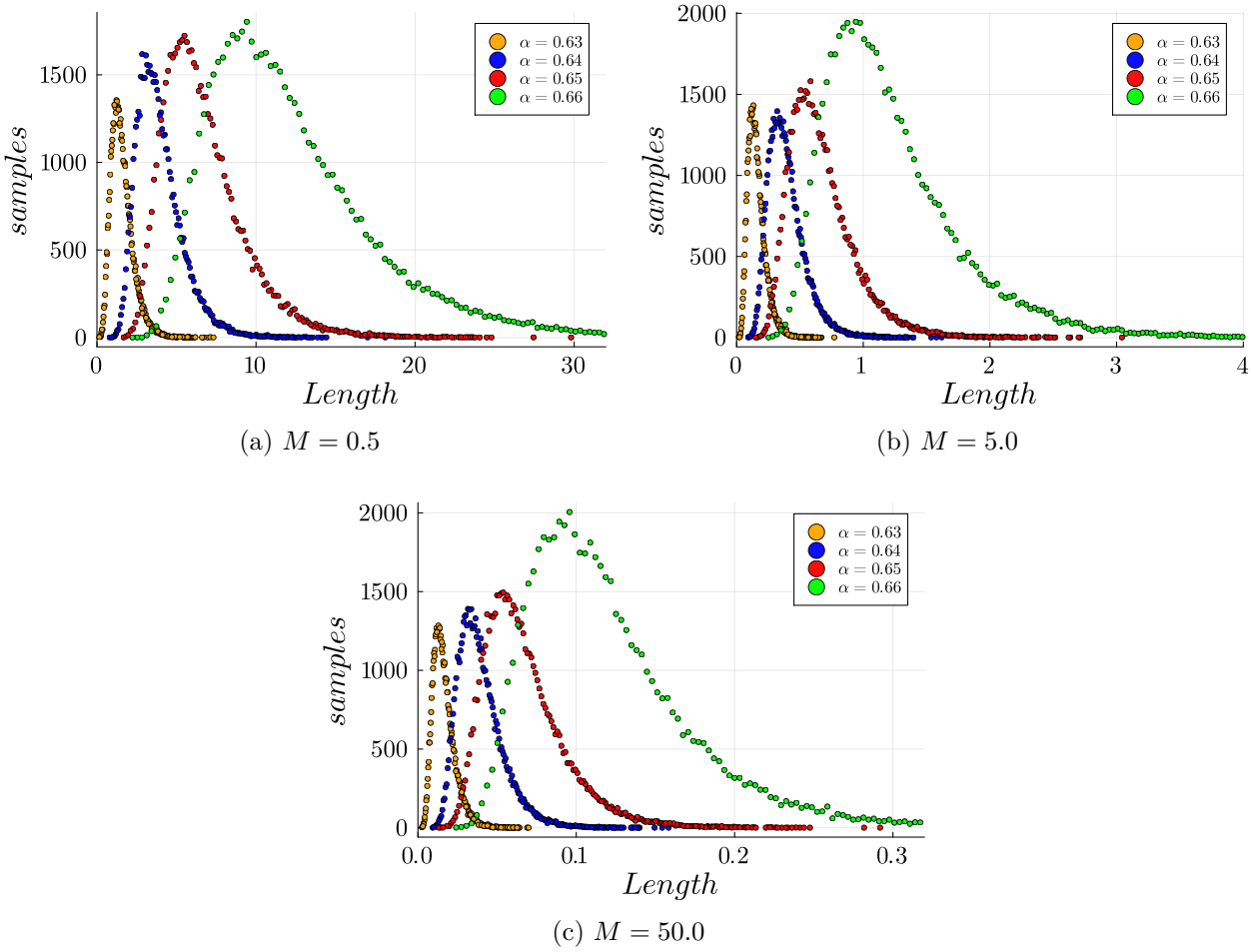

(a) $M = 0.5$ (b) $M = 5.0$

(c) $M = 50.0$

Figure 3.3: Distribution of lengths for lattice size $N_1 = 81$, a) $M = 0.5$, b) $M = 5.0$ and c) $M = 50.0$.

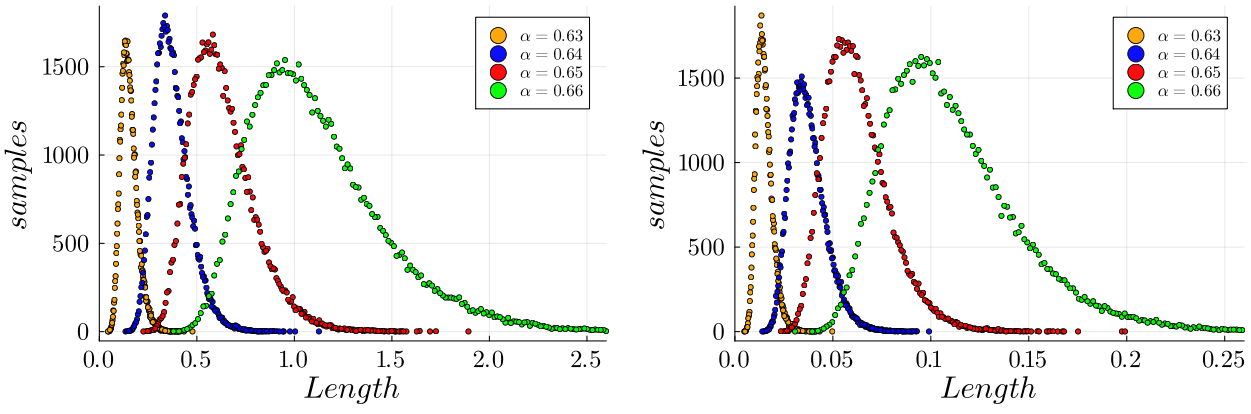

(a) $M = 5.0$ (b) $M = 50.0$

Figure 3.4: Distribution of lengths for lattice size $N_2 = 256$, a) $M = 0.5$ and b) $M = 50.0$.

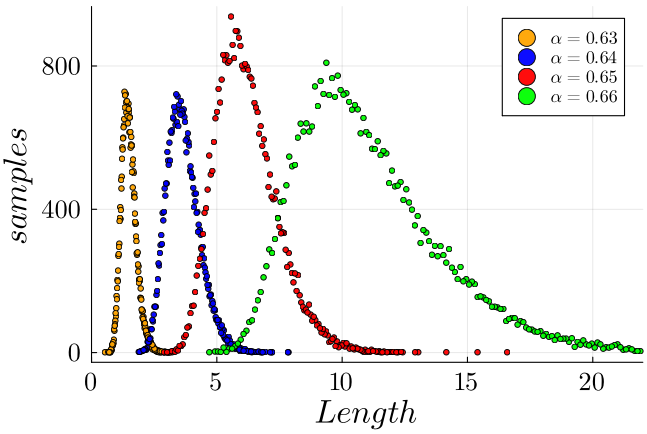

(a) $M = 0.5$

Figure 3.5: Distribution of lengths for lattice size $N_3 = 625$, a) $M = 0.5$.

3.2.3 Two-point correlation function

In this subsection, we revisit the two-point correlation function studied in [36], defined in analogy with ordinary lattice field theory, using a distinct numerical and conceptual approach, as detailed below.

In [36], the two-point correlation function was computed by taking products of the sampled field values $\phi_a\phi_b$, where a and b represent lattice vertices, and plotting them against the distance R between those vertices. There, R was defined as the length of the shortest path connecting a and b, obtained by summing the edge lengths along that path. This is referred to as the *Manhattan* distance:

$$d_M(a,b) = \sum_{i=1}^{4} |x_{i_a} - x_{i_b}| \,, \tag{3.12}$$

with periodic boundary conditions in all directions, so the topology must be accounted for when identifying the shortest path.

On the other hand, our analysis of $\langle\phi_a\phi_b\rangle$ departs from that of [36] in two key ways:

1. **Averaging over all vertex pairs.**
   Instead of fixing a reference vertex a and computing correlations with respect to it, we sum over all vertex pairs (a,b), collecting every instance of a given geodesic distance R across the lattice. This not only enlarges the statistical sample but also extends the accessible range of distances. For each bin of distances $[R, R+\delta R]$, we compute the average

of all products $\phi_a\phi_b$ separated by a distance within that bin.
The need for binning is crucial: since individual edge lengths follow a nontrivial distribution (see Figs. 3.3, 3.4, and 3.5), the same statistical structure is inherited to R, which is defined as a sum over these lengths. Thus, in practice, one encounters that without binning, even small numerical differences in R would artificially fragment the data, yielding noisy and unreliable statistics. Binning thus defines a consistent resolution for aggregating contributions to $\langle\phi_a\phi_b\rangle$ at fixed R. Thus, this statistical consideration departs from the analysis presented in [36].

2. **Euclidean metric.**
In addition to the Manhattan metric, we also compute correlations using the *Euclidean* geodesic distance,

$$d_E(a,b) = \sqrt{\sum_{i=1}^{4}(x_{i_a} - x_{i_b})^2}\,, \tag{3.13}$$

which allows us to examine the dependence of the results on the chosen notion of *distance* in the lattice geometry.

Figures 3.6–3.8 present the results of this analysis for the three lattice configurations N_1, N_2, N_3. Given that the distribution of edge lengths exhibits a consistent trend across the range $\alpha \in [0.63, 0.67]$ (which corresponds to the regime in which the total volume remains finite. See Figs. 3.3, 3.4, and 3.5), then the overall behavior of the two-point correlation function shows only minor variations with α within this interval. For clarity of this presentation, we therefore focus here on the representative case of $\alpha = 0.65$. For completeness, the corresponding results for $\alpha = 0.63, 0.64$, and 0.66 are provided in the Appendix B. A discussion of these results follows these plots.

3.2.3.1 Lattice size $N_1 = 81$

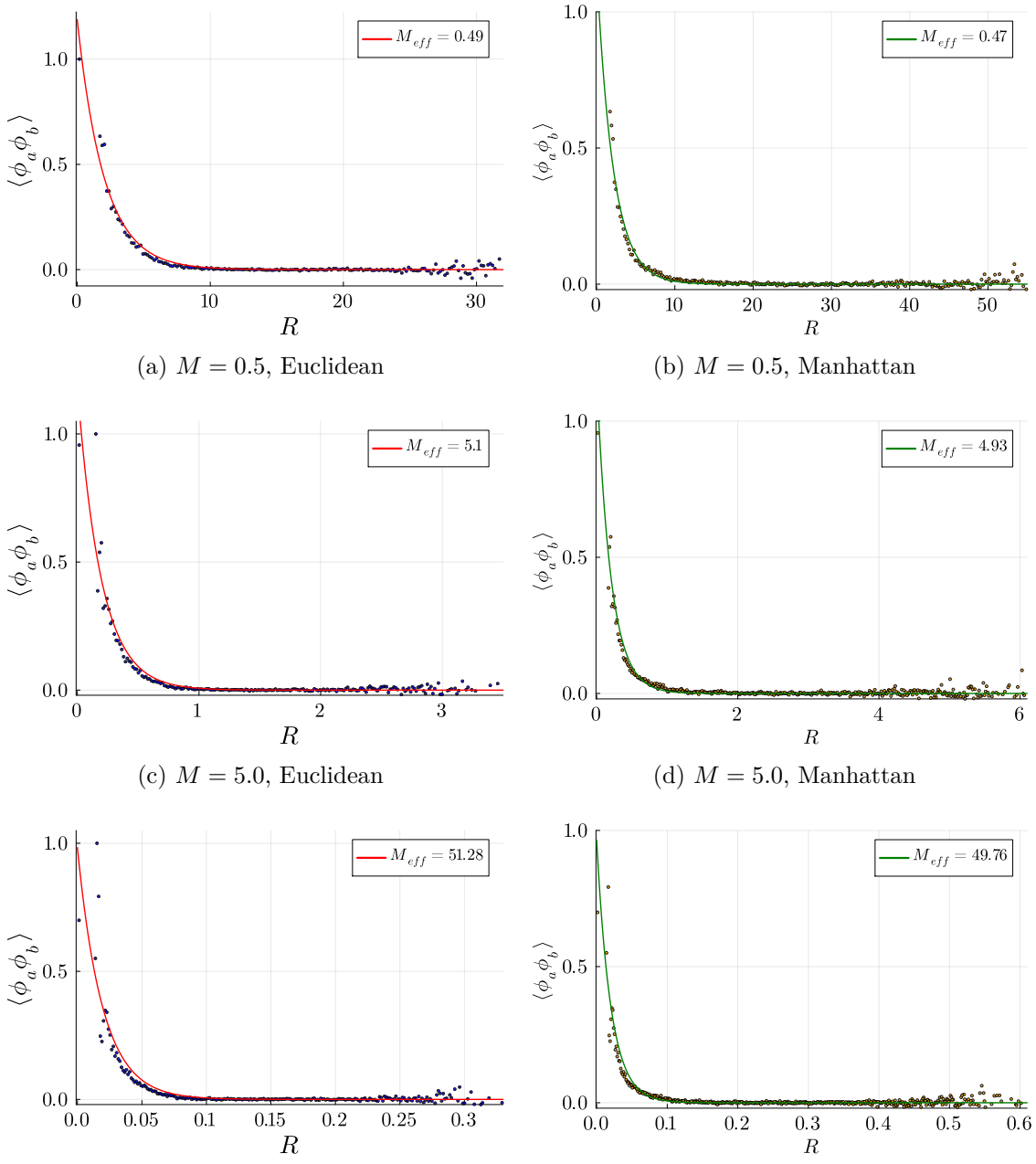

(a) $M = 0.5$, Euclidean

(b) $M = 0.5$, Manhattan

(c) $M = 5.0$, Euclidean

(d) $M = 5.0$, Manhattan

(e) $M = 50.0$, Euclidean

(f) $M = 50.0$, Manhattan

Figure 3.6: Two-point correlation $\langle \phi_a \phi_b \rangle$ as function of the Euclidean (left column) and Manhattan (right column) distance R, for different masses and fixed lattice size $N_1 = 81$ and $\alpha = 0.65$.

3.2.3.2 Lattice size $N_2 = 256$

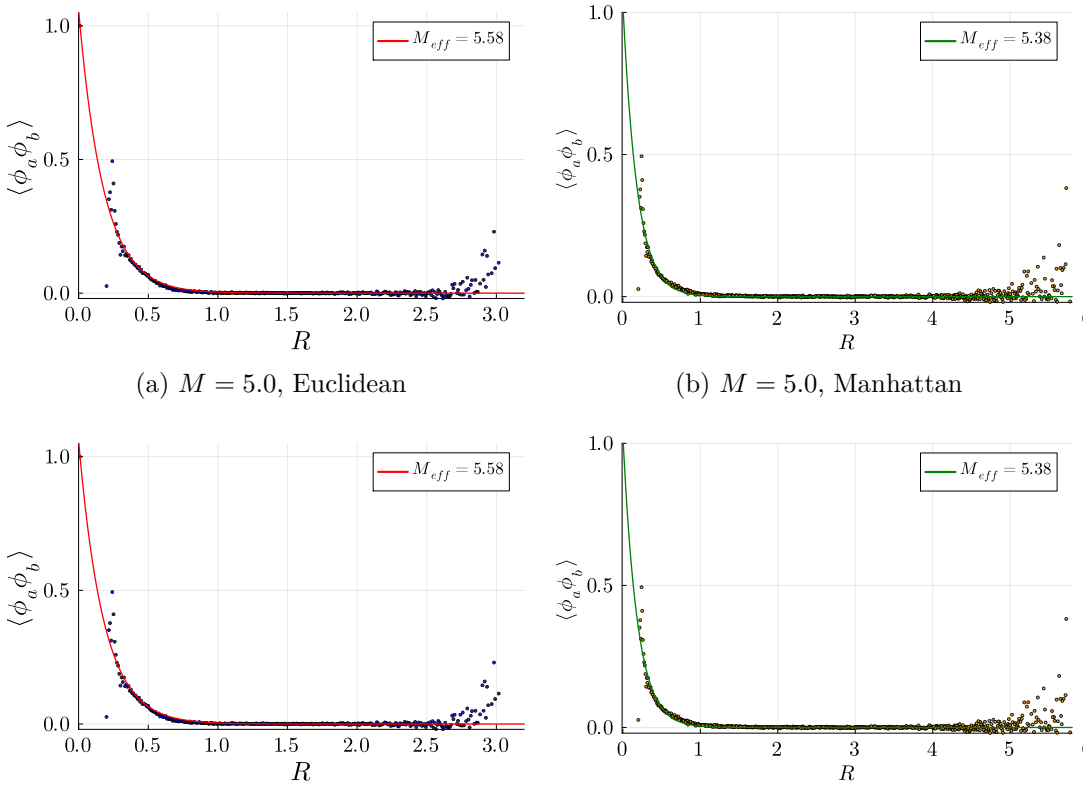

(a) $M = 5.0$, Euclidean (b) $M = 5.0$, Manhattan

(c) $M = 50.0$, Euclidean (d) $M = 50.0$, Manhattan

Figure 3.7: Two-point correlation $\langle \phi_a \phi_b \rangle$ as function of the Euclidean (left column) and Manhattan (right column) distance R, for different masses and fixed lattice size $N_2 = 256$ and $\alpha = 0.65$.

3.2.3.3 Lattice size $N_3 = 625$

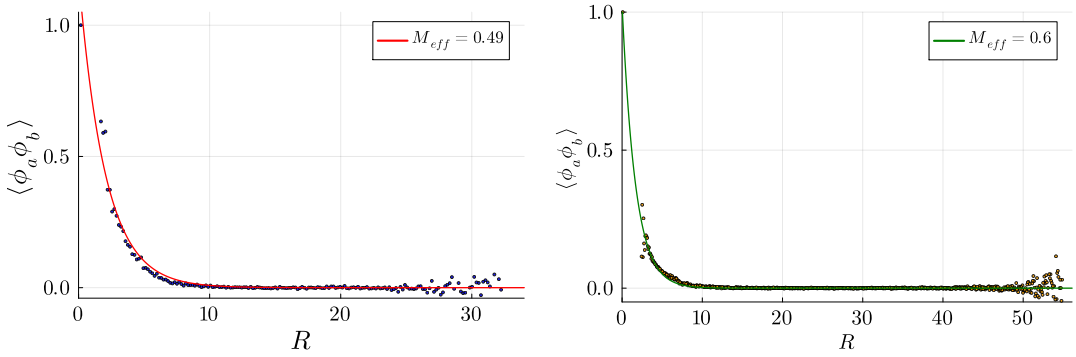

(a) $M = 0.5$, Euclidean (b) $M = 0.5$, Manhattan

Figure 3.8: Two-point correlation $\langle \phi_a \phi_b \rangle$ as function of the Euclidean (left figure) and Manhattan (right figure) distance R, for $M = 0.5$, lattice size $N_3 = 625$ and $\alpha = 0.65$.

As discussed above, although the spin foam model allows for configurations with very short edges, such configurations are strongly suppressed. This suppression makes short-distance correlations challenging to sample, and as a result, scalar field correlators at small but nonzero distances exhibit substantial fluctuations. At the opposite extreme, for large separations, we again observe a pronounced spread in the averaged values of $\langle\phi_a\phi_b\rangle(R)$. Here, the issue arises in big part due to the reduction in realizations of such samples: configurations with such large separations are rare, both because of the finite sampling of fields and lengths, and because of the probability of realizing such geometries is intrinsically low. Consequently, $\langle\phi_a\phi_b\rangle(R)$ in this regime does not fully converge, and the mean values are likely overestimated compared to expectations from standard lattice field theory. This overestimation could in turn bias any mass extraction based on the exponential decay of the correlator.
Qualitatively, across all lattice sizes, values of α within the plateau region, and scalar masses M, $\langle\phi_a\phi_b\rangle(R)$ consistently displays an exponential decay with increasing distance. The parameters α and M, however, affect the emergent geometry in distinct ways: from the horizontal axis of the plots above, one sees that increasing α shifts R toward larger values, thereby reducing correlations, whereas increasing M favors shorter edge lengths, effectively bringing vertices closer together. As a result, although a larger M shortens the correlation length, the apparent field correlations remain strong due to the reduced vertex separation. Overall, the increasing the scalar mass has a marked impact on the emergent geometry, by suppressing the correlations for fixed lattice size and α. Nevertheless, the shape of the two-point function closely mirrors that of a scalar field on a regular lattice with a spacing equal to the average spin foam edge length. This resemblance persists for larger lattices, where the greater number of vertex pairs, which allows to probe longer distances. To quantify this, we extract an effective mass by fitting a exponential decay as in eq. (1.4), interpreting the inverse correlation length as the effective mass. The resulting picture suggests that a scalar field coupled to cuboid spin foams behaves, to a good approximation, like a scalar field on a regular lattice with a *dynamical* lattice spacing that emerged by the peak nature of the spin foam plus matter amplitude.

3.2.3.4 Effective Mass

In Figure 3.9, we compare the effective mass M_{eff} obtained using both Euclidean and Manhattan distance definitions across the three lattice sizes N_1, N_2, N_3. The results show close agreement between the two approaches, with no significant deviations in any of the configurations studied. Notably, for $\alpha = 0.65$, the value of M_{eff} closely matches the bare mass M of the scalar field across all lattices and both distance metrics. It is also evident that M_{eff} decreases as α increases. Following the interpretation in [36], this decline is likely a numerical artifact

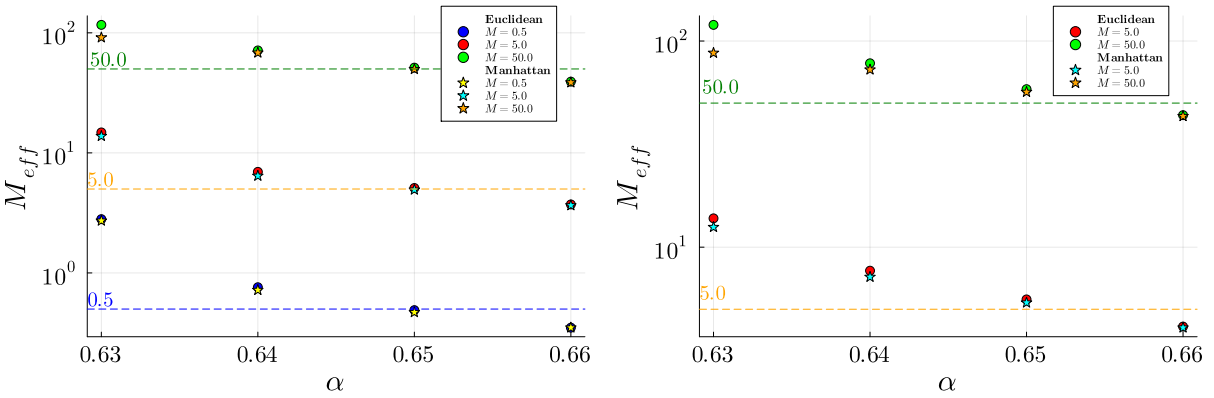

(a) Lattice size $N_1 = 81$

(b) Lattice size $N_2 = 256$

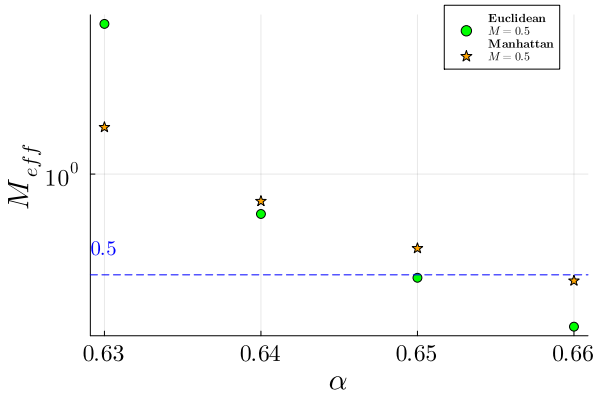

(c) Lattice size $N_3 = 625$

Figure 3.9: Comparison of estimated effective masses M_{eff} from the exponential decay of the scalar field correlator between Euclidean and Manhattan metrics. The horizontal lines, show the mass M of the scalar field for different configurations.

rather than a physical effect. At large distances, scalar field correlations become increasingly difficult to sample accurately. As a result, Monte Carlo methods may overestimate correlation values, artificially increasing the correlation length and thus leading to a smaller fitted mass.

3.2.4 Relational correlation function

We now present the numerical evaluation of the relational correlation function defined in eq. (3.7), which we reproduce here for clarity:

$$\langle \phi\phi(R)\rangle_\Delta := \frac{1}{Z}\int \prod_i d\phi_i \prod_k dl_k \sum_{\langle i,j\rangle} \underbrace{\langle \phi_i \phi_j \rangle}_{\substack{\text{correlator} \\ \text{defined for lengths } \{l_k\}}} \underbrace{\prod_v \tilde{\mathcal{A}}(\{l_k\})}_{\substack{\text{SF semiclassical} \\ \text{amplitude}}} e^{-\sum_{a,b}\phi_a K_{ab}\phi_b} \underbrace{\delta(d(i,j)-R)}_{\substack{\text{geodesic distance} \\ \text{between vertices } i,j}} \tag{3.14}$$

The main contributions to the relational correlation function $\langle\phi\phi(R)\rangle_\Delta$ arise from two ingredients: the two-point correlator $\langle\phi_i\phi_j\rangle$, evaluated for a given set of edge lengths $\{l_k\}$, and the semiclassical spin foam vertex amplitude $\tilde{\mathcal{A}}(\{l_k\})$. In subsection 3.2.3, we showed that $\langle\phi_i\phi_j\rangle$ exhibits exponential decay with geodesic distance R, in close agreement with expectations from lattice field theory. Separately, in subsection 3.2.2.2, we analyzed the distribution of edge lengths across sampled hypercubic geometries and found it to be peaked, with a long tail toward larger values, behavior that reflects the influence of $\tilde{\mathcal{A}}$. These two components, field correlations and spin foam geometry, come together in the evaluation of the relational correlator $\langle\phi\phi(R)\rangle_\Delta$. In the numerical simulations, lengths and fields were sampled from the distribution:

$$P(\{l_i\},\{\phi_a\}) = \frac{1}{Z}\prod_{v\in\star\sigma^4}\tilde{A}_v(\{l_i\})\,\exp\left(-\sum_{a,b}\phi_a K_{ab}(M,\{l_i\})\phi_b\right), \tag{3.15}$$

using Markov Chain Monte Carlo methods. Based on this sampling, the relational correlation function can be approximated as:

$$\langle\phi\phi(R)\rangle_\Delta \approx \frac{1}{n}\sum_{\text{samples},\ i<j}\phi_i\phi_j\ \delta(d(i,j)-R), \tag{3.16}$$

where n is the number of sampled configurations[3]. To illustrate the procedure, consider a lattice with $N_3 = 625$ vertices and a scalar field mass $M = 0.5$. From 2000 sampled lattice configurations, we evaluate $\phi_i\phi_j$ for each pair $i < j$ in every sample. For a chosen target distance $R = r_0$, we sum all such correlator contributions where the separation between i and j is in the interval $[r_0, r_0 + \delta r_0]$. Thus, we aggregate the contributions to $\langle\phi\phi(R = r_0)\rangle_\Delta$ following the same binning strategy we described in the past subsection when measuring $\langle\phi_a\phi_b\rangle(R)$. Grouping R into bins, is a essential part of the evaluation of this object, since one encounters that without binning, even small numerical differences in R would artificially fragment the data, yielding noisy and unreliable statistics. Binning thus allows to define a consistent resolution for aggregating contributions to $\langle\phi\phi(R)\rangle_\Delta$ at a given R.

At first glance, the strategy for computing $\langle\phi\phi(R)\rangle_\Delta$ appears similar to that used for $\langle\phi_a\phi_b\rangle(R)$ in subsection 3.2.3. The key difference lies in the fact that $\langle\phi\phi(R)\rangle_\Delta$ does **not** require averaging over contributions at a given geodesic distance, as is done in when computing $\langle\phi_a\phi_b\rangle(R)$. Instead, the *frequency* with which a given geodesic distance occurs across the ensemble of geometries directly influences the final value of $\langle\phi\phi(R)\rangle_\Delta$.

[3]This refers to the total number of samples obtained by the Markov Chain Monte Carlo method. As mentioned in subsection 3.2.1 these are 5000 for N_1 and N_2 and 2000 for N_3.

This distinction is important because, in the superposition of geometries, some geodesic distances are inherently more likely than others. Since R is a function of the underlying edge lengths of the lattices, the probability distribution of those lengths shapes how often each R is realized. Consequently, $\langle\phi\phi(R)\rangle_\Delta$ encodes both geometric and matter information, and its behavior reflects the nontrivial interplay between the statistical geometrical structure and the scalar field dynamics.

3.2.4.1 Distribution of R

Given that $\langle\phi\phi(R)\rangle_\Delta$ encodes how frequently a given geodesic distance R occurs within the superposition of geometries, we begin by analyzing the distribution of R across the different lattice sizes. This preliminary step is not merely technical, since it provides crucial insight into the statistical structure underlying this quantity. Understanding how often each distance is realized will help us interpret the behavior of $\langle\phi\phi(R)\rangle_\Delta$, whose results we present in a subsequent subsection.

In this subsection, we focus on representative cases of these distributions for clarity of presentation. Specifically, we present the case $\alpha = 0.65$, since for fixed M and lattice size, the overall trend of the distributions follows a similar pattern for different values of α (within the range in which the total volume remains finite). For completeness, the corresponding results for $\alpha = 0.63, 0.64$, and 0.66 are provided in Appendix C. The plots are discussed below.

Lattice size $N_1 = 81$

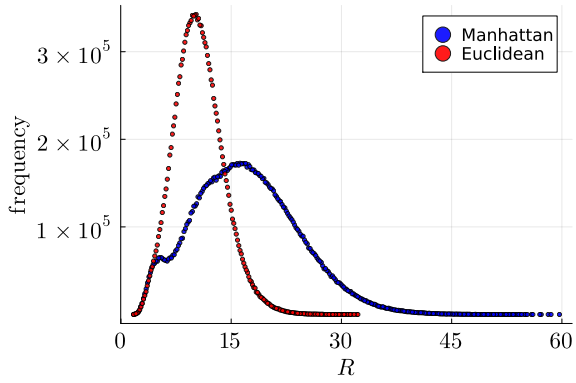

(a) $M = 0.5$

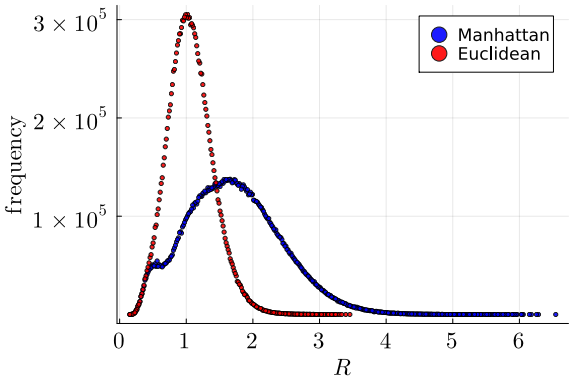

(b) $M = 5.0$

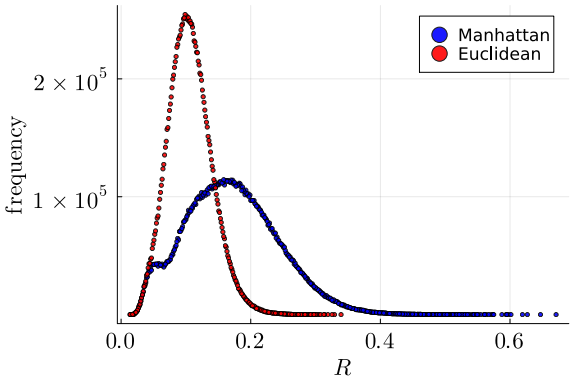

(c) $M = 50.0$

Figure 3.10: Distribution of distances R, for lattice size $N_1 = 81$ and $\alpha = 0.65$.

Lattice size $N_2 = 256$

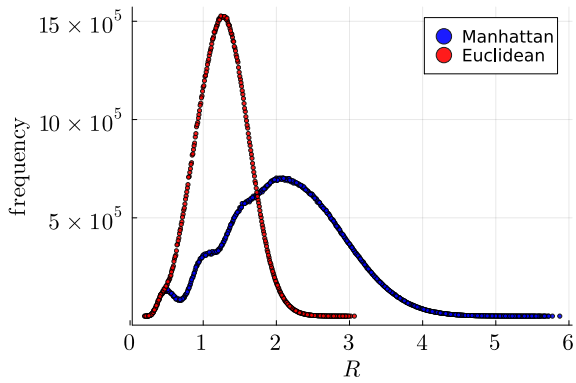

(a) $M = 5.0$

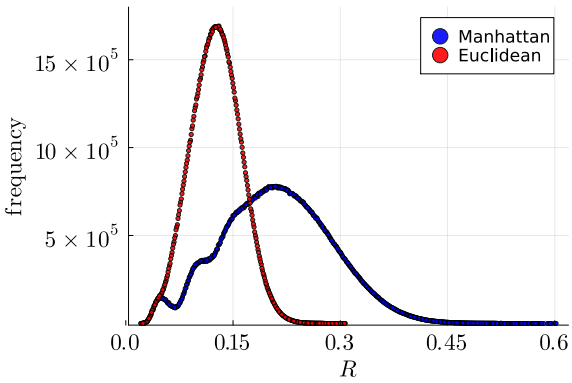

(b) $M = 50.0$

Figure 3.11: Distribution of distances R, for lattice size $N_2 = 256$ and $\alpha = 0.65$.

Lattice size $N_2 = 625$

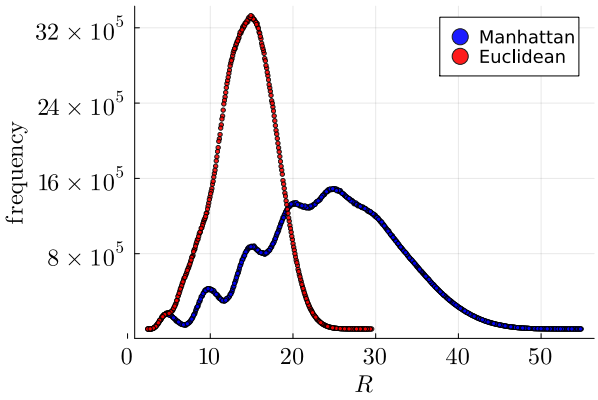

(a) $M = 0.5$

Figure 3.12: Distribution of distances R, for lattice size $N_3 = 625$ and $\alpha = 0.65$.

To interpret these results, we present a further analysis for both metrics as follows:

- **Manhattan metric**

  Using this metric, we find that the distribution of R exhibits a peaked profile with several local maxima, whose number increases with lattice size. This behavior can be understood by examining Fig. 3.13, where we plot the distribution of R for lattice size $N_3 = 625$ with $M = 0.5$ and $\alpha = 0.65$. In this case, we provide a more detailed analysis by grouping values of R according to the number of edges (or equivalently vertices, since #edges = #vertices+1) that make up the corresponding geodesic path. For example, red points represent distances between vertex pairs connected by a single edge (two vertices), yellow points correspond to paths of two edges (three vertices), and so on across the lattice. Summing this edge lengths is equivalent to the sum of $k \in \mathbb{N}$ approximately normally distributed edge lengths (see the histograms in Figs. 3.3, 3.4, and 3.5), which yields approximately another normal distribution with mean and variance scaling as $\mu_T = \sum_k \mu_k$, $\sigma_T^2 = \sum_k \sigma_k^2$. This explains the normal-like profiles of the underlying distributions of R when grouping by the number of edges in the corresponding geodesic path. The blue points then represent the total distribution of R, obtained by summing over all possible realizations of geodesic distances for different vertex separations, where each local peak corresponds to a maximum of one of these underlying quasi-normal distributions.
  As a further general observation, for a fixed lattice size and scalar mass M, larger values of R are realized in the Manhattan metric than in the Euclidean case. This is expected, since the sum of the absolute value of edge lengths is, in general, greater than the square root of the sum of their squares for the same set of edges.

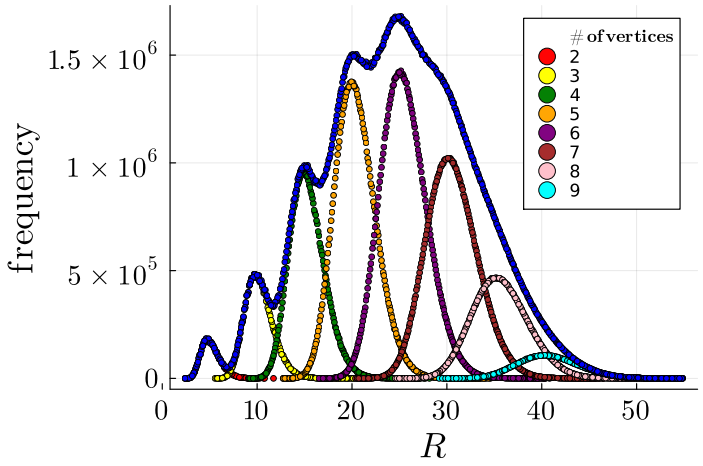

(a) $M = 0.5$

Figure 3.13: Distribution of R (blue points) in the Manhattan metric, grouped by the number of edges (labeled by the number of vertices apart since # vertices = # edges +1) each geodesic path R is made up.

- **Euclidean metric**

  In the case of the Euclidean metric, we find that for all lattice sizes, scalar masses M, and values of α, the histograms of geodesic distances R display a Gaussian-like profile centered around a characteristic mean value. This behavior follows the same underlying reasoning as in the Manhattan metric case. As before, we perform the analysis by grouping R according to the number of edges composing a given geodesic path, for lattice size $N_2 = 256$, $M = 5.0$ and $\alpha = 0.65$ (see Fig. 3.14). In this setting, we observe that the mean values of the underlying quasi-normal distributions are closer together, effectively overlapping and producing a smoother overall distribution of R when these individual contributions are summed. This tighter clustering of the underlying distributions arises from the fact that the Euclidean metric generally yields smaller distances, since the square root of the sum of squared edge lengths is always less than or equal to the sum of their absolute values. Consequently, the mean values μ_k of the quasi-normal distributions are themselves smaller, leading to a stronger overlap in a more compact region of R.

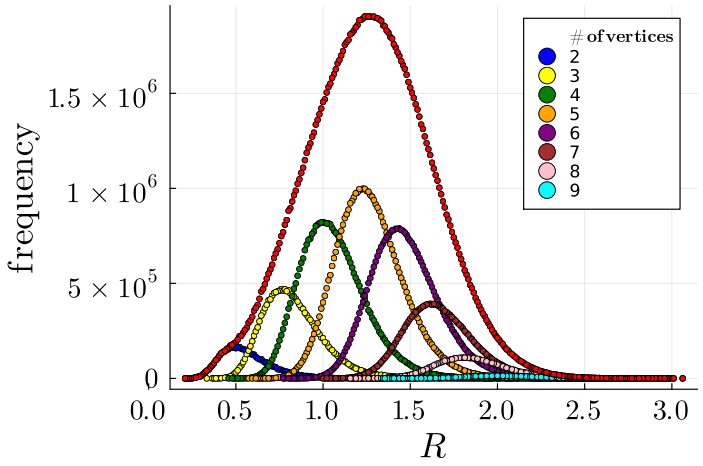

(a) $M = 0.5$

Figure 3.14: Distribution of R (red points) in the Euclidean metric, grouped by the number of edges (labeled by the number of vertices apart since # vertices = # edges +1) each geodesic path R is made up.

3.2.5 $\langle\phi\phi(R)\rangle$

Having understood the pure geometric part of $\langle\phi\phi(R)\rangle_\Delta$, in this subsection we present the results for $\langle\phi\phi(R)\rangle_\Delta$ across the three lattice sizes N_1, N_2, and N_3 in Figures 3.15–3.17, using both geodesic distance definitions (Euclidean and Manhattan). As in previous sections, we restrict our attention to the $\alpha = 0.65$, given that for fixed lattice size and M, $\langle\phi\phi(R)\rangle_\Delta$ follows a similar trend. For completeness, the results for $\alpha = 0.63, 0.64, 0.66$ are presented in Appendix D. A discussion of these results follows the plots.

3.2.5.1 Lattice size $N_3 = 625$

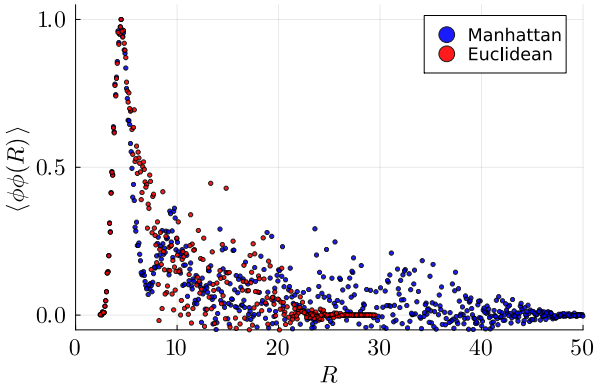

(a) $M = 0.5$

Figure 3.15: $\langle\phi\phi(R)\rangle_\Delta$ for lattice size $N_3 = 625$, $M = 0.5$ and $\alpha = 0.65$.

3.2.5.2 Lattice size $N_1 = 81$

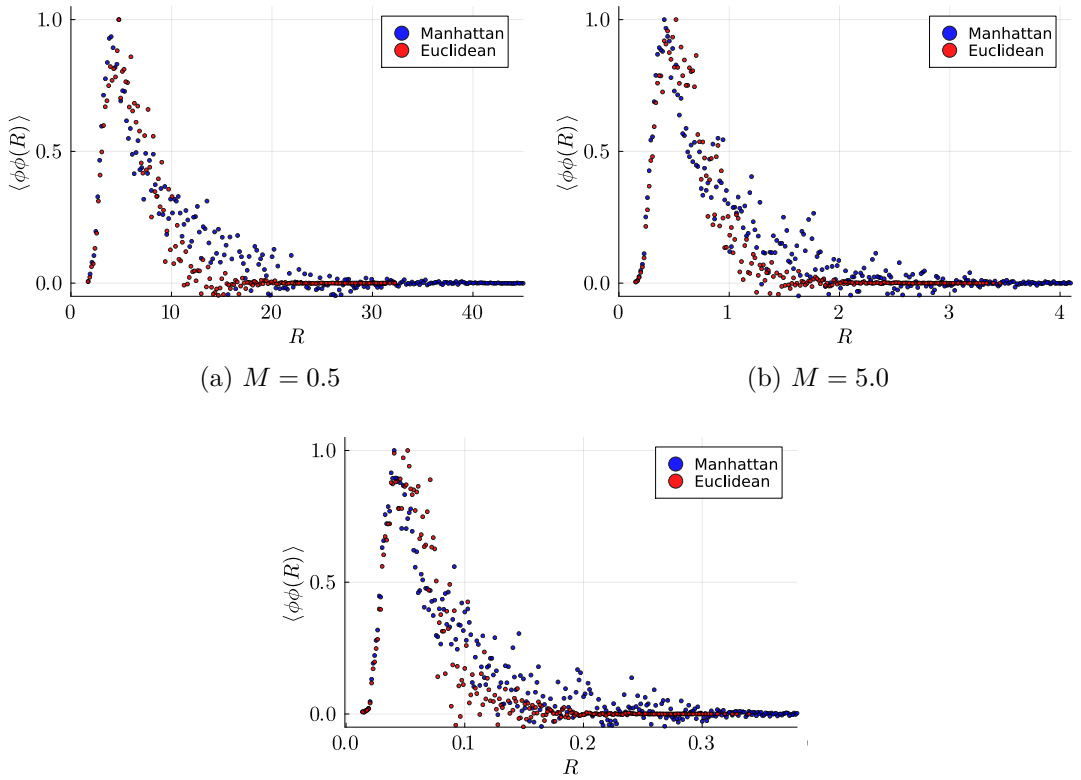

(a) $M = 0.5$ (b) $M = 5.0$

(c) $M = 50.0$

Figure 3.16: $\langle\phi\phi(R)\rangle_\Delta$ for lattice size $N_1 = 81$, $\alpha = 0.65$ and different values of M. a) $M = 0.5$, b) $M = 5.0$, c) $M = 50.0$.

3.2.5.3 Lattice size $N_2 = 256$

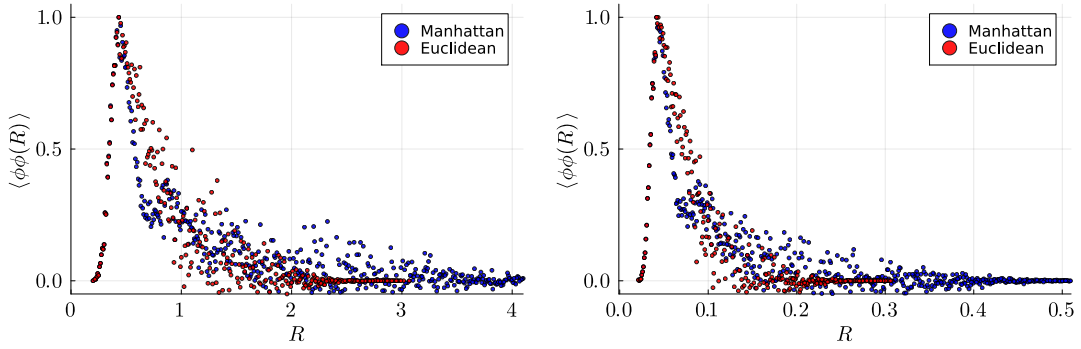

(a) $M = 5.0$ (b) $M = 50.0$

Figure 3.17: $\langle\phi\phi(R)\rangle_\Delta$ for lattice size $N_2 = 256$, $\alpha = 0.65$ and different values of M. a) $M = 5.0$, b) $M = 50.0$.

We begin this analysis by recalling that $\langle\phi\phi(R)\rangle_\Delta$ is determined by two key ingredients: the two-point correlators $\langle\phi_i\phi_j\rangle$ themselves, and the frequency with which a given geodesic distance R appears in the sampled lattice ensemble. This naturally raises a question: if a particular distance R is realized only rarely, can the fields, according to the definition of $\langle\phi\phi(R)\rangle_\Delta$, still be meaningfully correlated at that scale? To address this, we identify three characteristic regimes in the behavior of $\langle\phi\phi(R)\rangle_\Delta$:
At short distances $R = r_{\text{small}}$, the correlator $\langle\phi_i\phi_j\rangle$ tends to be large. However, Figures D.1–D.6 show that $\langle\phi\phi(r_{\text{small}})\rangle$ is suppressed in this region. This in accordance with the fact that such small geodesic separations occur rarely across the sampled configurations. Despite the high amplitude of $\langle\phi_i\phi_j\rangle$, the low frequency of these distances leads to a negligible contribution.
At large distances $R = r_{\text{large}}$, the correlator $\langle\phi_i\phi_j\rangle$ is exponentially suppressed, and such distances also occur less frequently. As a result, the correlator $\langle\phi\phi(R)\rangle$ decays rapidly in this regime.
In the intermediate region $R = \tilde{r}$, a clear peak (using both metrics) appears in all figures. While the correlators $\langle\phi_i\phi_j\rangle$ decrease with distance, the higher frequency of occurrence for $\tilde{r}$ amplifies their cumulative contribution, leading to the observed maximum in $\langle\phi\phi(R)\rangle$.
We also observe that for all lattice sizes N_1, N_2, N_3, the correlator $\langle\phi\phi(R)\rangle$ exhibits a broader spread at large R, particularly as α increases, since this leads to larger lengths (and therefore larger R). As discussed in subsection 3.2.3, sampling scalar field configurations at large geodesic distances becomes increasingly challenging, leading to pronounced statistical fluctuations. This indicates that a substantially larger number of samples would be required to ensure robust convergence of $\langle\phi\phi(R)\rangle$ across all regimes. Moreover, at most distances the statistical resolution exhibits considerable variance. Although an overall trend is discernible, the observed variability in $\langle\phi\phi(R)\rangle$ makes it clear that full convergence has not yet been achieved with the current data sets.

The insights outlined above can now be tested directly with the measured values of $\langle\phi\phi(R)\rangle_\Delta$. Given that the two-point correlator $\langle\phi_i\phi_j\rangle$ decays exponentially as $\exp(-M \cdot R)$, where M is the mass of scalar field, it follows that $\langle\phi\phi(R)\rangle_\Delta$ should, to a good approximation, behave like the product:

$$\#R_{\text{sample}} \cdot \exp(-M \cdot R) \ , \tag{3.17}$$

where $\#R_{\text{sample}}$ denotes the number of realizations of a given geodesic distance R, as indicated by the histograms. This comparison is illustrated in Figures 3.18 to 3.20, where we highlight representative cases, particularly those exhibiting nontrivial or pathological behavior in the

measured values of $\langle\phi\phi(R)\rangle_\Delta$. Notably, across both Euclidean and Manhattan metrics, our empirical approximation closely matches the actual values of $\langle\phi\phi(R)\rangle_\Delta$. This strong agreement reinforces the interpretation that the relational correlation function is effectively governed by the interplay between the exponential decay of $\langle\phi_i\phi_j\rangle$ and the frequency distribution of geodesic distances R across the sampled geometries.

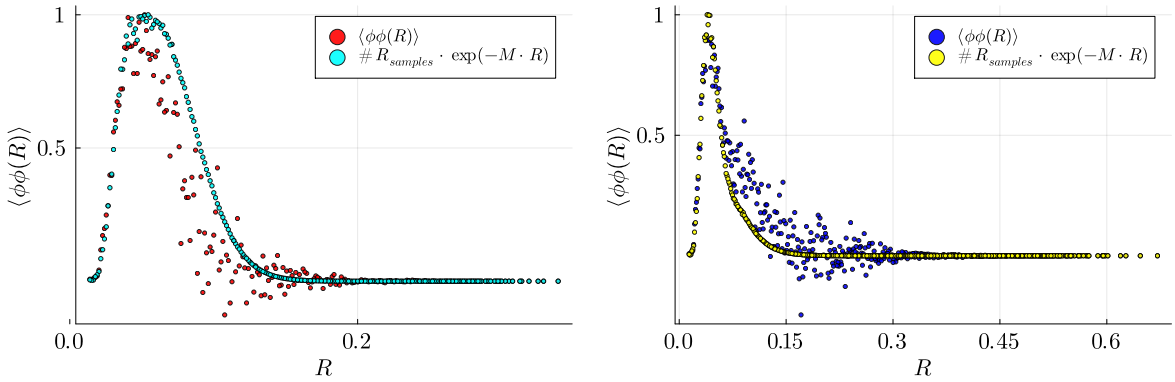

(a) Euclidean (b) Manhattan

Figure 3.18: $\langle\phi\phi(R)\rangle_\Delta$ and $\#R_{\text{sample}} \cdot \exp(-M \cdot R)$, for $N_1 = 81$, $M = 50.0$, $\alpha = 0.65$. a) Euclidean Metric, b) Manhattan Metric.

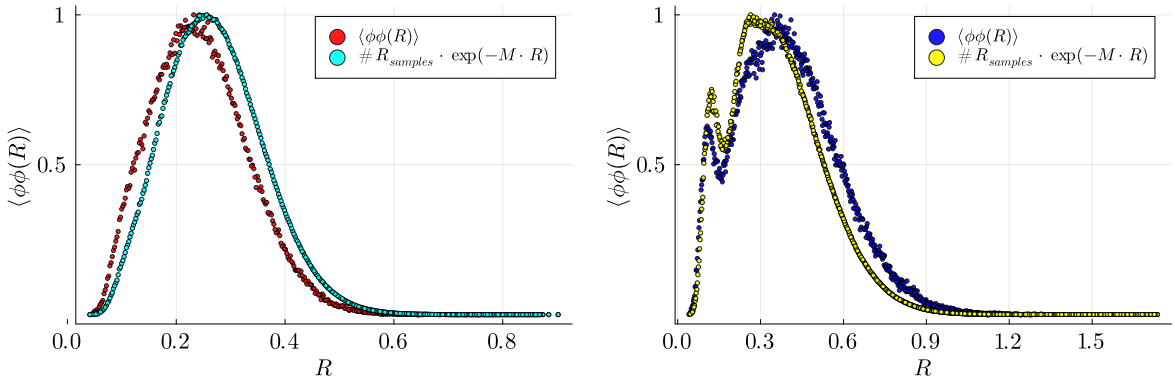

(a) Euclidean (b) Manhattan

Figure 3.19: $\langle\phi\phi(R)\rangle_\Delta$ and $\#R_{\text{sample}} \cdot \exp(-M \cdot R)$, for $N_2 = 256$, $M = 5.0$, $\alpha = 0.63$. a) Euclidean Metric, b) Manhattan Metric.

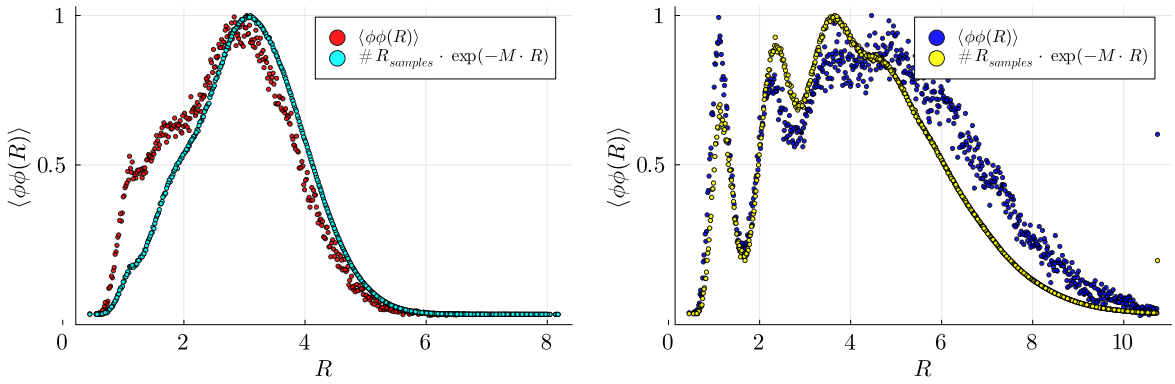

(a) Euclidean (b) Manhattan

Figure 3.20: $\langle\phi\phi(R)\rangle_\Delta$ and $\#R_{\text{sample}} \cdot \exp(-M \cdot R)$, for $N_3 = 625$, $M = 0.5$, $\alpha = 0.63$. a) Euclidean Metric, b) Manhattan Metric.

3.2.6 Discussion on numerical results

In this Chapter, we studied geometric and matter observables within a semiclassical spin foam model minimally coupled to a scalar field. Our revisited studied of geometric observables, such as the total 4D volume and the distribution of edge lengths, reproduced the results found in [36]. These can be summed up as follows: We observe that two competing effects take place in our system. In one hand, the scalar field suppresses large edge lengths, with an observed amplified effect when increasing scalar mass. On the other hand, the spin foam amplitude, controlled by the parameter α, favors large lengths as α increases. As a result, we identified three qualitative regimes: small α leads to minimal edge lengths, large α favors maximal ones, and an intermediate "plateau" region yields finite edge lengths and volumes consistent with an emergent regular lattice.

On the matter side, we first computed the expectation value of the two-point[4] correlation function of the scalar field, using a numerical strategy different from that employed in [36]. Here, we average all contributions of the field products $\phi_a\phi_b$ (where a, b are any vertices in the lattice) within the bin $[R, R + \delta R]$. In this sense, this expectation value can also be regarded as a relational observable (since this is computed in relation to the geodesic distance R), although it remains non-local and follows a similar computational strategy than in standard lattice field theory, which differs from our definition of a relational correlation function $\langle\phi\phi(R)\rangle$. The important lesson obtained from this evaluation, is that $\langle\phi_a\phi_b\rangle(R)$ behaves really close to the well know two-point correlation function from a lattice field theory defined on a fixed background, with correlation lengths approximately matching those of a free scalar on a regular lattice. In

[4]Not to be confused with the relational correlation function $\langle\phi\phi(R)\rangle$. Here we refer to the computed average of $\langle\phi_a\phi_b\rangle(R)$, where a and b are arbitrary vertices.

addition, computing R using both metrics (Euclidean and Manhattan), shows no substantial difference in the computed effective masses M_{eff}. Variations in effective mass are attributed to sampling difficulties at large geodesic distances.
Finally, we proposed and evaluated, for the first time, a *relational* correlation function $\langle\phi\phi(R)\rangle$ that captures diffeomorphism-invariant information by correlating scalar field values as a function of the geodesic distance R. In this construction, the frequency with which a given geodesic distance R occurs plays a central role: in the type of setting investigated here, certain distances are naturally realized more often than others. Our numerical results for $\langle\phi\phi(R)\rangle$ reveal that this observable encodes the interplay between field correlations and the probability of realizing a given R, showing explicitly that correlations depend not only on distance but also on its statistical weight in the geometry ensemble. However, these results also come with limitations, which we discuss as follows:

- **Convergence.**
  An initial challenge becomes apparent from Figures 3.18–3.20, which compare the numerical evaluation of $\langle\phi\phi(R)\rangle_\Delta$ with our empirical approximation. As α increases and larger values of R are probed, the variance between the numerical data and the approximation grows, indicating that additional data is needed to achieve convergence in most cases across all three lattice sizes N_1, N_2, N_3. The origin of this issue can be traced as follows: Although geodesic distance histograms R exhibit smooth distributions, the correlator $\langle\phi_a\phi_b\rangle$ shows significant fluctuations, particularly at very small and very large distances. These fluctuations directly propagate into $\langle\phi\phi(R)\rangle_\Delta$, especially in the large-R regime, where the quality of the approximation is reduced. Thus, this further suggest, that a larger sample of scalar field configurations is required to improve the statistical robustness of the results.

- **Larger lattices.**
  Extending the analysis to larger lattices is crucial to validate the observed behavior of the relational correlation function and to exclude possible finite-size artifacts. In particular, realizing larger geodesic distances than those available in the current data set would provide a clearer understanding of the long-range structure of correlations.

While the results presented here are promising, they rest on several simplifying assumptions that must eventually be relaxed to test their robustness in more physically realistic scenarios. On the spin foam side, this requires moving beyond quantum cuboids and semiclassical approximations toward more general classes of geometries. However, the inherently oscillatory nature of spin foam amplitudes poses a major computational challenge: in many cases, standard Monte Carlo

techniques are insufficient, though some initial progress has been made in this direction [92, 93].

A complementary avenue is to extend the matter-coupling framework to the full quantum spin foam amplitudes and to investigate interactions with other types of matter, such as gauge fields and fermions, while maintaining numerical feasibility. In this sense, the present work should be viewed as a first step along a broader research avenue aimed at bridging simplified spin foam models with richer, fully dynamical matter sectors.

Chapter 4

Scalar Matter defined on a dynamical lattice.

Motivated by the coupled model studied in Chapter 3, this chapter introduces a simplified toy model: a free massive scalar field on a one-dimensional dynamical, irregular lattice, where length amplitudes are modeled by a Gaussian distribution over edge lengths as a simplified spin foam-like structure. This reduction preserves essential features of the original model from Chapter 3, while making explicit evaluations of the partition function and expectation values of this model feasible. It also allows us to probe larger lattices and gain insight into matter-geometry coupling. At the core of our analysis is the relational correlation function $\langle\phi\phi(R)\rangle$, whose study tests its robustness, limitations, and potential as a meaningful observable in a background-independent framework.

4.1 1D toy model

In Chapter 3, we investigated the coupling of a free massive scalar field to a restricted spin foam model in the semiclassical limit. During this study, several computational challenges emerged. Although Markov Chain Monte Carlo methods are applicable to this model, their computational cost grows rapidly with the number of lattice vertices, limiting the number of feasible samples of fields and lengths. As discussed in [36], implementing Markov Chain Monte Carlo *moves* to explore configurations of the coupled system is a nontrivial task. Moreover, a large number of samples and Monte Carlo steps are required to reduce autocorrelation and achieve thermalization. These factors make the study of larger lattices particularly demanding. In addition, obtaining reliable results at both very small and very large geodesic distances requires an even larger number of samples. In these regimes, significant fluctuations are observed in both geometric and matter observables due to the intrinsically low probability of configurations

in these regions. Such fluctuations in many cases prevent the convergence of the measured observables, which is reflected in the disproportional variations of observables, most notably in the field correlation functions.
To gain deeper insight into the interplay between the couple of matter and geometry, while keeping the computational complexity manageable, we introduce in this chapter a simplified toy model. This model retains the core structure of the coupled system explored in Chapter 3 but replaces the semiclassical spin foam vertex amplitude with an idealized, simplified version of this amplitude as is detailed in the section below. This will enables us to explore regions of configuration space that are otherwise inaccessible due to computational constraints. In particular, our focus is to better understand the behavior and interpretation of the relational correlation function $\langle\phi\phi(R)\rangle$, which serves as a key test observable in background independent settings. The detailed formulation of our simplified model is presented in the following section.

4.1.1 Partition function of the model

Our goal in this chapter is to introduce a simplification of the scalar field coupled to the restricted semiclassical spin foam model presented in Chapter 3. The original partition function is given by:

$$Z = \int \prod_i dl_i \int \prod_{a\in\sigma_0} d\phi_a \prod_{v\in\star\sigma_0} \tilde{A}_v(\{l_i\}_{i\in\sigma_4}) \exp\left(-\sum_{a,b}\phi_a K_{ab}(M,\{l_i\})\phi_b\right), \tag{4.1}$$

where the most involved component is the vertex amplitude $\tilde{A}_v(\{l_i\})$, interpreted as the spin foam amplitude associated with a given set of edge lengths $\{l_i\}$. From our analysis in Chapter 3, we observed that the distribution of edge lengths (after integrating out the scalar field) in the hypercubic lattice approximately follows a normal distribution (see Figures 3.3, 3.4, and 3.5). Thus, to simplify computations, while keeping a similar profile of the combined matter plus matter amplitude, we replace $\tilde{A}_v(\{l_i\})$ with a more manageable approximation that captures its qualitative features. Specifically, we model the amplitude of each edge length l as a Gaussian profile:

$$P_\nu(l) = \frac{1}{\sigma\sqrt{2\pi}} \exp\left(-\frac{1}{2}\left(\frac{l-\mu}{\sigma}\right)^2\right), \tag{4.2}$$

where μ and σ represent the mean and standard deviation of the length distribution, respectively. This simplification allows us to interpret the system as a free massive scalar field defined on a dynamical, irregular lattice, in which the edge lengths are weighted by a normal distribution. Accordingly, we define the partition function of the toy model as:

$$Z_{1\mathrm{D}} := \int \prod_i dl_i \int \prod_{a\in\sigma_0} d\phi_a \prod_{v\in\star\sigma_0} P_v(\{l_i\}) \exp\left(-\sum_{a,b} \phi_a K_{ab}(M,\{l_i\})\phi_b\right), \tag{4.3}$$

We restrict our analysis to the one-dimensional case to keep the number of degrees of freedom manageable, which allows us to perform full computations of the partition function despite the exponential complexity of the coupled system. Thus, tha matrix K is as defined on eq. (1.49). The above simplifications in our system offer some major computational advantages:

- It allows us to explore larger lattice sizes than those feasible in the full model of Chapter 3.

- The Gaussian form of $P_v(\{l_i\})$ allows us to continuously study how the shape of this length distribution influences the expectation values of observables by varying σ and μ respectively. In particular, this allows us to investigate the transition from irregular, dynamical lattices to configurations with nearly constant lattice spacing, thereby it is possible to investigate as consistency check the limit in which ordinary lattice field theory is expected to emerge.
  Furthermore, the close form of the amplitude will prove handy for exploring different numerical approaches, such as importance sampling of lengths, as it will be detailed in next subsections.

- At the core of our analysis lies the relational correlator $\langle\phi\phi(R)\rangle$, which we aim to compute and evaluate as a candidate for a physically meaningful observable in a background independent framework.

We can further simplify the partition function (4.3), by performing Gaussian integrations on the fields, to obtain:

$$Z_{1\mathrm{D}} = \int \prod_i dl_i \frac{1}{\sqrt{\det K}} \prod_{v\in\star\sigma_0} P_v(\{l_i\}), \tag{4.4}$$

this representation of $Z_{1\mathrm{D}}$ is particularly convenient for explicit evaluations, as it requires integration only over the set of the edge lengths. In contrast, the computational strategy in [36] evaluated the partition function of the coupled system as a function of both the fields and the lengths. Here, we instead explore the feasibility of formulating the coupled system entirely in terms of the set of lengths $\{l_i\}$.

4.1.2 Expectation values of observables

Proceeding analogously to Chapter 3, we define geometric and matter observables in our system (4.4). On the geometric side, we define the total volume of our system as:

$$\langle V \rangle = \frac{1}{Z_{1D}} \int \prod_i dl_i \, \frac{V}{\sqrt{\det \mathrm{K}}} \prod_{v \in \star\sigma_0} P_v(\{l_i\}) \tag{4.5}$$

where $V = \sum_{i=1}^{k} l_i$, and k is total number of edges in the lattice. On the matter side, the relational correlation function (see eq. (3.1.4)) with respect to the geodesic distance R is given by:

$$\langle \phi\phi(R) \rangle = \frac{1}{Z_{1D}} \int \prod_i dl_i \, K^{-1}_{ab} \prod_{v \in \star\sigma_0} P_v(\{l_i\}) \; \delta(d(i,j) - R) \tag{4.6}$$

4.2 Numerical Results

4.2.1 Full computations

Despite the simplifications introduced in our toy model (4.4), the computational complexity to fully evaluate its partition function remains exponential. Consider, the one-dimensional lattice with periodic boundary conditions consisting of n edge lengths. To perform a numerical evaluation of $Z_{1\mathrm{D}}$, assume each length l_i is restricted to the interval $[a, b]$ (where a, b are the lower and upper cutoff, respectively), with $i = 1, \ldots, n$, and this interval is discretized into $m \in \mathbb{N}$ equal subintervals. In this case, the total number of function evaluations required to approximate $Z_{1\mathrm{D}}$ is m^n. Thus, increasing the accuracy in the approximation gets rapidly costly, which gets worse as the number of vertices increase in the lattice.

To gain initial insights into the model, we consider a one-dimensional lattice with periodic boundary conditions and five edges. We study the influence of different length distributions by fixing the mean to $\mu = 0.5$ and varying the standard deviation $\sigma = 0.05, 0.02, 0.005$, as illustrated in Figure 4.1. These choices correspond to distributions that become increasingly sharply peaked around their mean value as σ decreases. For the scalar field, we explore two values of the mass parameter: $M = 5.0$ and $M = 0.5$. For the explicit numerical evaluation, we impose both lower and upper cutoffs on the allowed values of the lattice edge lengths, restricting them to the interval $[0, 1]$. This choice ensures that the most probable configurations of lengths lie within the integration domain (see Fig. 4.1). The interval is then discretized into 70 equally spaced subintervals, allowing us to approximate the integrals as finite sums over discrete length values.

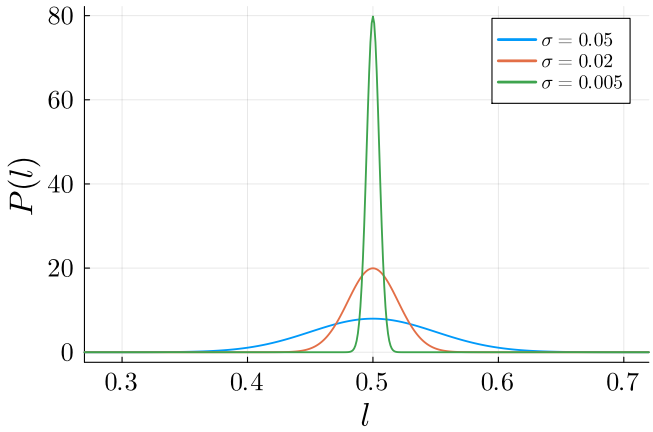

Figure 4.1: Normal distributions $P(l)$ for different values of σ. In all cases $\mu = 0.5$.

4.2.1.1 Relational correlation: $\langle\phi\phi(R)\rangle$

The results of the evaluation of the relational correlation function $\langle\phi\phi(R)\rangle$ are presented in Figures 4.3 and 4.4. In our setup, the geodesic distance R between two vertices is defined as the sum of the edge lengths along the shortest path connecting them. Due to the periodic boundary conditions imposed on the lattice, the path calculation must account for this topology.

Figure 4.3 explores the impact of varying σ on the length distribution while keeping the scalar field mass M fixed. As σ decreases, the distribution $P_v(l)$ becomes more sharply peaked around its mean $\mu = 0.5$, favoring edge lengths close to this value. As a result, $\langle\phi\phi(R)\rangle$ exhibits sharp local maxima (depending on σ) at distances that are approximately integer multiples of μ. This reflects the increased probability of geodesic paths composed of nearly identical edge lengths which are close to the mean value μ. We provide more details about how this process takes place below.
We also explore the impact of different mass values M. Figure 4.4 shows that increasing the mass M of the scalar field leads to a suppression of the overall amplitude of $\langle\phi\phi(R)\rangle$, consistent with the behavior of two-point functions in lattice field theory. As the mass increases, the correlation length decreases, resulting in more rapid decay of field correlations with distance.

Across both figures, a consistent qualitative trend emerges: $\langle\phi\phi(R)\rangle$ displays local maxima that lie approximately at integer multiples of μ and the width of which varies with σ. At the same time, these maxima decay as R increases. This trend, departs from the well know exponential decay of the correlation functions in lattice field theory. This behavior can be traced to the interplay between two key factors in the definition of the correlator (see eq. (4.6)): the inverse of the matrix K, K^{-1}_{ab}, which encodes the matter field correlations, and the product $\prod_{v\in\star\sigma_0} P_v(\{l_i\})$, which determines the statistical weight of each geometric configuration.

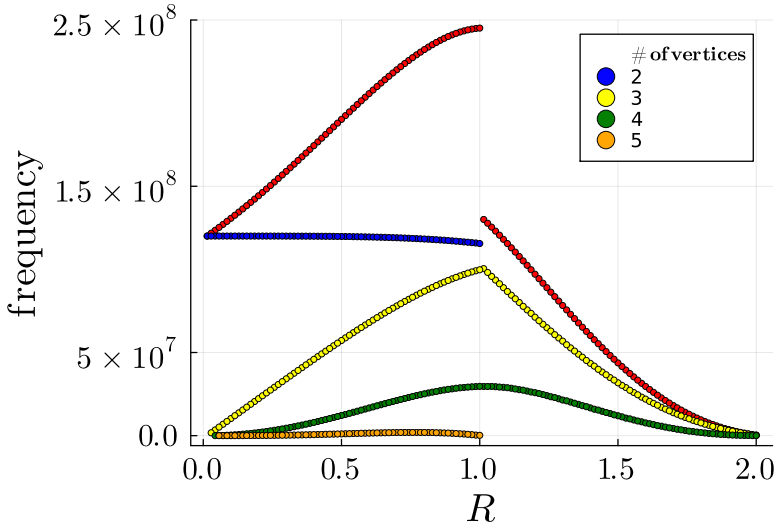

Figure 4.2: Distribution of geodesic distances R (shown as red points) across a one-dimensional lattice with five edge lengths and periodic boundary conditions. Each edge length is discretized over the interval $[0, 1]$, which is subdivided into 70 equally spaced subintervals for numerical integration. Thus, each distance R is composed of contributions from different numbers of vertices (or equivalently, edges of different sizes). For example, the blue points represent distances computed from vertex pairs connected by a single edge (i.e., two vertices), while the yellow points correspond to distances composed of two edges (three vertices), and so on across the lattice. The red points, therefore, represent the total distribution of R, obtained by summing over all possible realizations of geodesic distances for different vertex separations. Remarkably, the resulting distributions resemble that of a sum of k uniformly distributed variables, where in our case, k corresponds to the number of edges involved. This is expected, as the process of measuring R follows a similar logic of summing edge lengths sampled from the uniform distribution given by the discretization of the interval $[0, 1]$. Thus, as k increases, the resulting distribution converges to a normal distribution as stated by the central limit theorem. In our particular system, given the periodic boundary conditions, we observe that the maximum number of edges a distance is composed is 4, which contributions are the lowest of all.

The inverse matrix K^{-1}_{ab} contributes an exponential decay with distance, typical of a massive scalar field. Meanwhile, the weight of a given geodesic distance R is shaped by how the corresponding path is constructed, that is, how many edges it includes and how close those edge lengths are to the mean value μ. For example, a path consisting of a single edge with length close to μ will have a maximal amplitude and thus contribute substantially to $\langle\phi\phi(R)\rangle$. Similarly, paths constructed with k edges, each near the mean μ, also contribute significantly. In contrast, paths composed of edge lengths far from the mean are exponentially suppressed, and their contribution to $\langle\phi\phi(R)\rangle$ is negligible, this is reflected in the regions between the local maxima of $\langle\phi\phi(R)\rangle$.

At first glance, one might expect that the distances R between any two vertices are equally distributed. However, a careful analysis reveals that some distance occur more frequently than others. This analysis is presented in Figure 4.2, where we plot the distribution of all

paths between any two vertices in the dynamical lattice, grouped by the number of edges they contain (or equivalently, the number of vertices, since #vertices = #edges + 1). For instance, we observe that paths consisting of one edge, i.e., between neighboring vertices, are the most common. This is expected, as these are the shortest possible paths, given by the smallest possible non-vanishing length defined by the discretization of the interval $[0, 1]$. Additionally, as the number of edges in a path increases, the distribution of resulting distances becomes increasingly Gaussian. This behavior arises because measuring this observable is equivalent to summing k random variables drawn from a uniform distribution. Hence, as k increases, the central limit theorem ensures that the resulting distribution approaches a normal distribution. Finally, the overall suppression of $\langle\phi\phi(R)\rangle$ at larger R results from both the exponential decay of field correlations and the reduced number of configurations that realize longer geodesic distances. As R increases, both the number of contributing realizations and the field correlations diminish, leading to the observed suppression in the amplitude of $\langle\phi\phi(R)\rangle$.

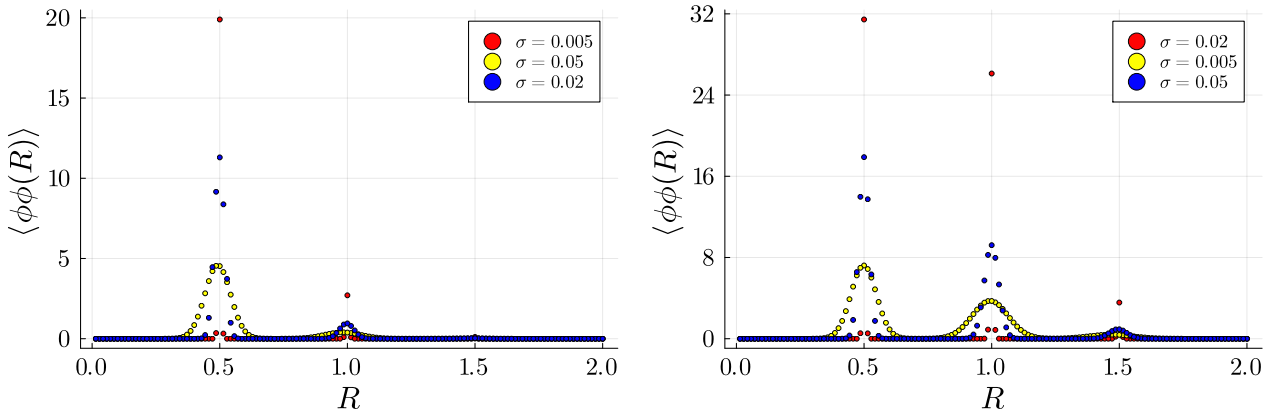

(a) $M = 5.0$ (b) $M = 0.5$

Figure 4.3: Comparasion of $\langle\phi\phi(R)\rangle$ for different values of σ. Decreasing the value of σ leads to narrower peaks around local maxima of $\langle\phi\phi(R)\rangle$. In all plots $\mu = 0.5$.

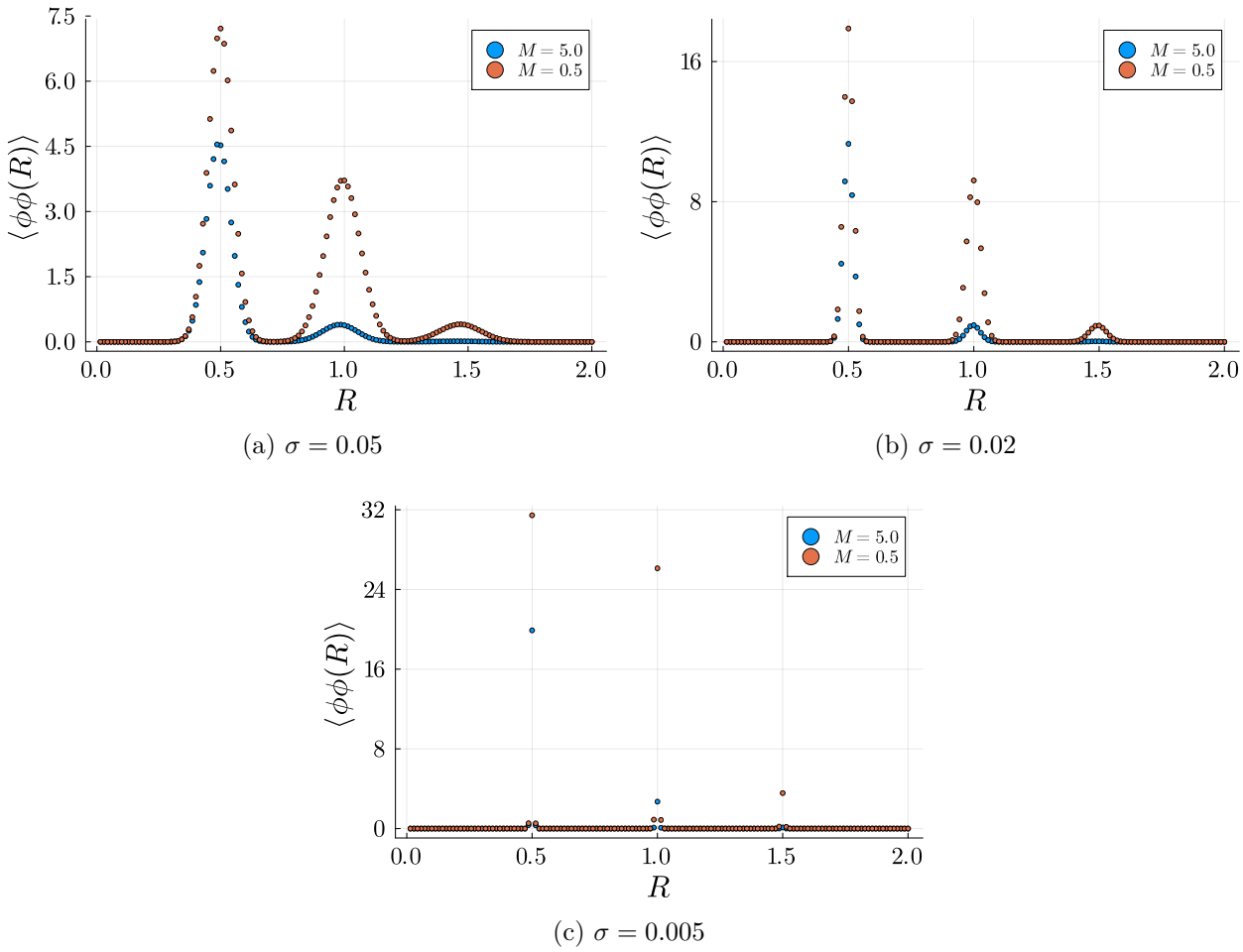

(a) $\sigma = 0.05$

(b) $\sigma = 0.02$

(c) $\sigma = 0.005$

Figure 4.4: Comparasion of $\langle\phi\phi(R)\rangle$ for different values of M. Increasing the mass M of the scalar field suppresses the amplitude of $\langle\phi\phi(R)\rangle$. In all plots $\mu = 0.5$.

4.2.1.2 Total Volume

In Figure 4.5, we present the results for the total volume $\langle V\rangle$. The average volume is close to 2.5, which we understand as each edge length in the lattice (made of 5 edges) being close to the mean value $\mu = 0.5$ from the distribution $P_\nu(l)$. The error bars indicate the standard deviation of $\langle V\rangle$. For sharply peaked distributions (e.g., $\sigma = 0.005$), the volume is tightly concentrated around 2.5. As σ increases, the length distribution becomes broader, resulting in a larger standard deviation for the average volume. We also observe that increasing the scalar field mass M reduces the total volume of the lattice. This behavior can be understood from the expression for $\langle V\rangle$ given in eq. (4.5). In this expression, the scalar field mass enters through the determinant of the matrix K, thus increasing M enlarges this determinant, which appears in the denominator of the expectation value, thus slightly suppressing the overall value of $\langle V\rangle$.

At the same time, this shows that defining our system only in terms of the set of lengths $\{l_i\}$ (see eq. (4.4)) effectively encodes the matter information of the fields.

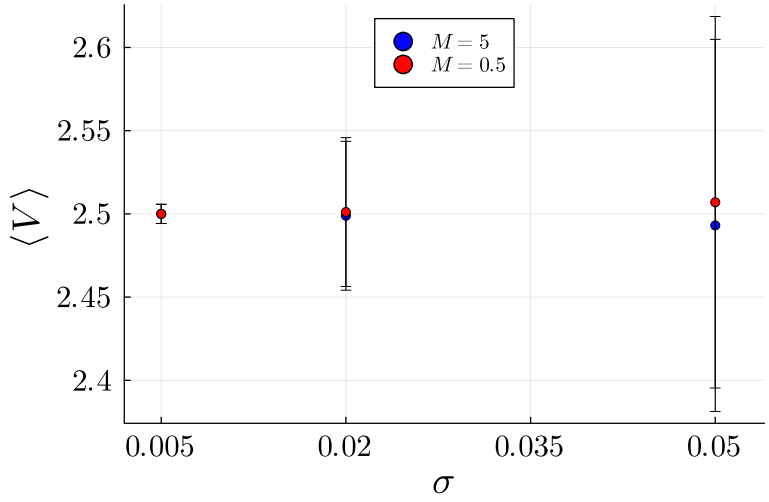

Figure 4.5: $\langle V \rangle$ for lattice size 5 and $\mu = 0.5$.

4.2.1.3 Cutoff dependency of $\langle \phi\phi(R) \rangle$

As a consistency check, we examine how the relational correlation $\langle \phi\phi(R) \rangle$ depends on the upper cutoff imposed on the edge lengths. In this context, the cutoff is not merely a technical choice to delimit the range of numerical integration, something that, given the form of $P_v(\{l_i\})$, one could implement over a finite set. Rather, as indicated by the distance distributions R in Fig. 4.2, one can ask if this cutoff influences the shape of this distribution. Given that this information directly enters the definition of $\langle \phi\phi(R) \rangle$, its impact must be explicitly investigated. Thus, here we study three different cutoff intervals for the edge lengths: $l_i \in [0, 1]$, $[0, 1.5]$, and $[0, 2]$, for $i = 1, \ldots, 5$, while keeping all other parameters fixed: $M = 5.0$, $\mu = 0.5$, and $\sigma = 0.05$. Each interval is discretized into 70, 105, and 140 subintervals, respectively, to maintain consistent resolution and numerical accuracy when approximating $\langle \phi\phi(R) \rangle$ by discrete sums. The results of these evaluations are presented in Figure 4.6a. We observe that increasing the cutoff leads to an increasing amplitude of $\langle \phi\phi(R) \rangle$. This behavior can be understood by examining the histogram of geodesic distances R across the lattice in Fig. 4.6b. For a fixed R, increasing the cutoff enlarges the set of admissible edge lengths, thereby increasing the number of possible realizations of that distance. Since the amplitude of $\langle \phi\phi(R) \rangle$ is determined by the total number of such realizations contributing to it, a larger cutoff results in more contributions for each R, and thus a higher overall amplitude of this object.

Remarkably, the total volume $\langle V \rangle$ and its standard deviation remain unchanged across all three cutoff values. In all cases, we find $\langle V \rangle = 2.49306381$ and $\sigma_{\langle V \rangle} = 0.11178090$. This outcome is

expected, as the computation of $\langle V \rangle$ depends solely on the distribution of edge lengths and not on the distribution of geodesic distances R across the lattice.

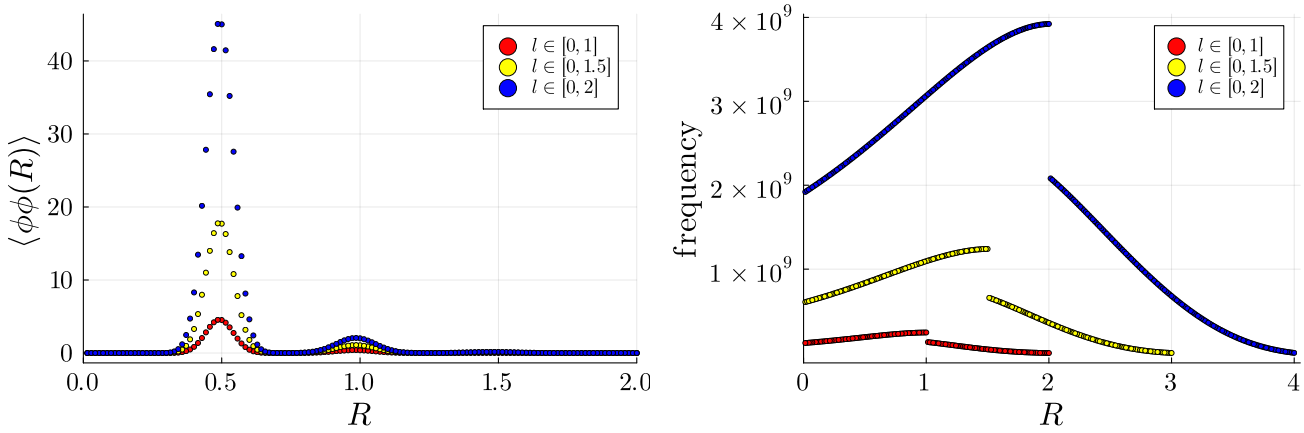

(a) (b)

Figure 4.6: Cutoff dependency of $\langle \phi\phi(R) \rangle$. a) $\langle \phi\phi(R) \rangle$. b) Distribution of R for the three different cutoffs of lengths. Increasing the cutoff leads to a bigger number of possible realizations of a given R which has a direct impact on the evaluation of $\langle \phi\phi(R) \rangle$, as for a given R more contributions are added to $\langle \phi\phi(R)$ as the cutoff increases.

4.2.2 Importance Sampling

Given the exponential complexity of the computations of our model Z_{1D}, we proceed now with a different computational approach, that allows us to explore bigger lattices.
Importance sampling is a numerical method that allows to approximate integrals or sums by sampling the most probable configurations of the system, especially in high-dimensional settings, where evaluating integrals of the form:

$$I = \int_{\Omega} f(x)\, dx \tag{4.7}$$

is analytically intractable or numerically expensive. One approach to approximating such integrals is the Monte Carlo method, where samples x_i are drawn uniformly from Ω, and the integral is estimated by the sample average:

$$I \approx \frac{1}{N} \sum_{i=1}^{N} f(x_i). \tag{4.8}$$

However, uniform sampling is often inefficient, especially when $f(x)$ is sharply peaked in certain regions of Ω. In such cases, a more suitable approximation is obtained via *importance sampling*.

In this approach, samples are drawn from a *proposal distribution* $p(x)$, which is chosen to approximate the shape of $f(x)$, with $p(x) > 0$ wherever $f(x) \neq 0$. Thus, we can rewrite the integral (4.7) using the probability density function $p(x)$ as:

$$I = \int_\Omega \frac{f(x)}{p(x)} p(x)\, dx = \mathbb{E}_p \left[\frac{f(x)}{p(x)} \right]. \tag{4.9}$$

where $\mathbb{E}_p[\cdot]$ is the expectation value with respect to p. This allows us to approximate I using samples $\{x_i\}_{i=1}^N$ drawn from $p(x)$ instead of the uniform distribution as:

$$I \approx \frac{1}{N} \sum_{i=1}^{N} \frac{f(x_i)}{p(x_i)}, \quad x_i \sim p(x). \tag{4.10}$$

where $x_i \sim p(x)$ indicates that the sample x_i is drawn from the probability distribution $p(x)$. It is also important that note, that $p(x)$ must be easy to sample from and should resemble the shape of $f(x)$. Ideally, one should choose $p(x) \propto |f(x)|$ to minimize variance.
Importance sampling can be implemented to evaluate the partition function of our model. In this case, given the form of our partition function (eq. (4.4)), p is *already* contained in this expression, which we choose as (see eq. (4.2)) :

$$p(\{l_i\}) = \prod_v P_v(l_i) \quad , \tag{4.11}$$

with this choice, we approximate Z_{1D} (see eq. (4.4)) as:

$$Z_{1D} \approx \frac{1}{N} \sum_{\{l_i\}} \frac{1}{\sqrt{\det K}} \quad , \quad \{l_i\} \sim p \tag{4.12}$$

where N is the total number of samples drawn from p. In a similar manner we can approximate the expectation values of observables. For instance, $\langle V \rangle$:

$$\langle V \rangle \approx \frac{1}{Z_{1D}} \frac{1}{N} \sum_{\{l_i\}} \frac{V}{\sqrt{\det K}} \quad , \quad \{l_i\} \sim p \tag{4.13}$$

Similarly, the relational correlation function is approximated as:

$$\langle \phi\phi(R) \rangle \approx \frac{1}{Z_{1D}} \frac{1}{N} \sum_{\{l_i\}} K^{-1}_{ab}\, \delta(d(i,j) - R) \quad , \quad \{l_i\} \sim p \tag{4.14}$$

4.2.2.1 Lattice size 5

We begin our analysis by comparing the results from the previous subsection, obtained through full computations on a one-dimensional lattice with five edge lengths, with those obtained via importance sampling. Specifically, we focus on the case with parameters $\sigma = 0.05$, $\mu = 0.5$, and scalar field masses $M = 0.5$ and $M = 5.0$, as shown in Figure 4.7.
As a reminder to the reader, the full computations were performed by discretizing each edge length l_i (with $i = 1, \ldots, 5$) into 70 equally spaced subintervals over the range $[0, 1]$, resulting in a total of 70^5 function evaluations to approximate the integrals over lengths. In contrast, the results shown in Figure 4.7 were obtained using the importance sampling method, drawing 3×10^6 samples from the distribution $p = \prod_v P_v(\{l_i\})$. The sampling was performed using built-in statistical libraries in Julia, which allow direct generation of random numbers from a normal distribution with mean μ and standard deviation σ. Thus, samples of l were repeatedly drawn according to $P_\nu(l)$. In this sense, the computational advantage of importance sampling is notorious.
Before presenting the results obtained via importance sampling, we first discuss a preliminary numerical consideration that proves essential when drawing edge lengths from the distribution $P_\nu(l)$. Specifically, it is necessary to implement a binning strategy to classify the sampled lengths. In practice, a minimum bin width δl must be defined to group sampled lengths into intervals of the form $[l, l + \delta l]$, otherwise, the histogram of sampled lengths fails to reconstruct the expected normal distribution. An alternative and easy approach is to round the sample lengths to a fixed number of decimal places, but this method was found to be too coarse and inflexible for accurately classifying the data. In contrast, binning allows one to explicitly control the resolution at which two lengths are considered statistically indistinguishable. A similar binning procedure is applied when computing geodesic distances R (which is simply the sum of k edge lengths), as previously discussed in Chapter 3. Distances are grouped into bins of size $[R, R + \delta R]$, which is crucial for robust statistical estimation. Without this step, even small numerical differences between distances would lead to artificially sparse statistics, thereby distorting the computed correlator $\langle \phi\phi(R) \rangle$. Thus, binning serves a dual purpose, it ensures accurate reconstruction of the sampled distributions and defines a consistent resolution for aggregating contributions to our relational correlation function.

In Figure 4.7a, we observe that the results obtained via importance sampling closely follow those of the full computation. However, a limitation arises due to the small lattice size: since most sampled lengths cluster around the mean $\mu = 0.5$, it becomes difficult to realize larger geodesic distances, as such configurations are less probable. Furthermore, this bias arises because the majority of sampled distances are composed of two edge lengths, which are more probable given

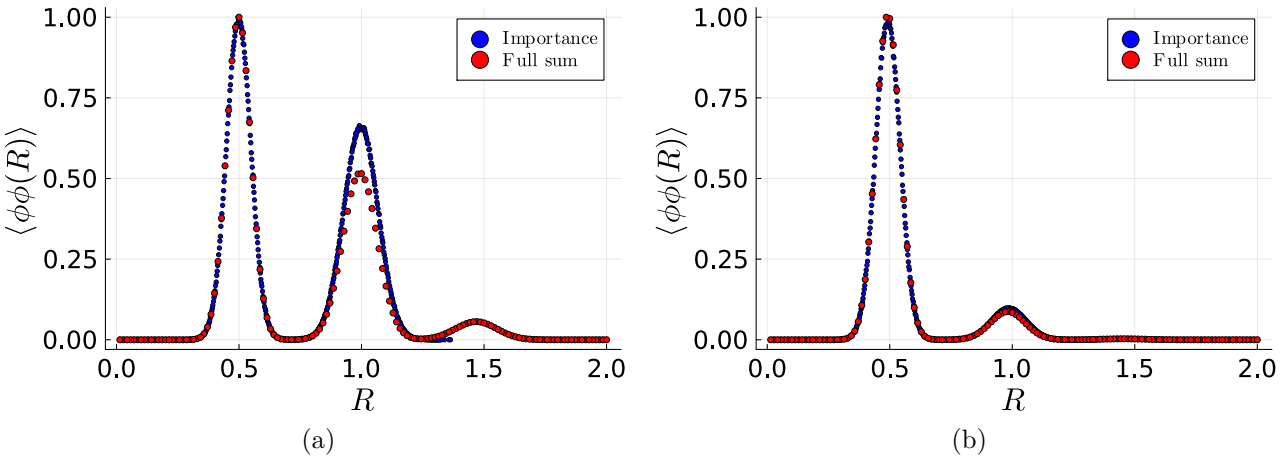

Figure 4.7: $\langle\phi\phi(R)\rangle$ using importance sampling and the full summation. In all cases $\sigma = 0.5$ and $\mu = 0.5$. In these figures, we have normalized $\langle\phi\phi(R)\rangle$ to the first maxima.

the peaked nature of $P(l)$ and the periodic boundary conditions. Consequently, configurations contributing to longer distances (involving three or more edge lengths) are underrepresented. As a result, the third local maximum seen in the full computation plot is not reproduced by the importance sampling method. Additionally, given the periodic boundary conditions, the second local maximum is overestimated, as explained above, many more contributions cluster around this regions, since on average this corresponds of distances make up of two edges, since these are shorter than ones make up of three edges or more (which occur less often given the periodic boundary conditions). However, these lattice artifacts have less impact in larger lattices (as we discuss in the following subsections).
In contrast, Figure 4.7b shows an almost perfect agreement between importance sampling and the full computation. In this case, all local maxima are accurately captured. This improved match is likely due to the larger scalar field mass $M = 5.0$, which suppresses long-range correlations and compensates for the overestimation of the contributions to the second local maxima of $\langle\phi\phi(R)\rangle$ around this region.

In Figure 4.8, we compare the expectation value of the total volume $\langle V\rangle$ computed using both importance sampling and the full sum evaluation. Across all tested values of the mass M and the parameter σ, we observe excellent agreement between the two methods. This expected, as $\langle V\rangle$ does not depend on the statistics of R, but only on the distribution of lengths $P_\nu(l)$ and the mass M of the matter field.
These results show in particular, that defining the coupled system only in terms of lengths effectively contains all the information of the system and different numerical tools can be employed to evaluate it. This is a substantial difference from the model studied in Chapter

3, where the coupled model was defined in terms of fields and lengths, which computationally gets more involved.

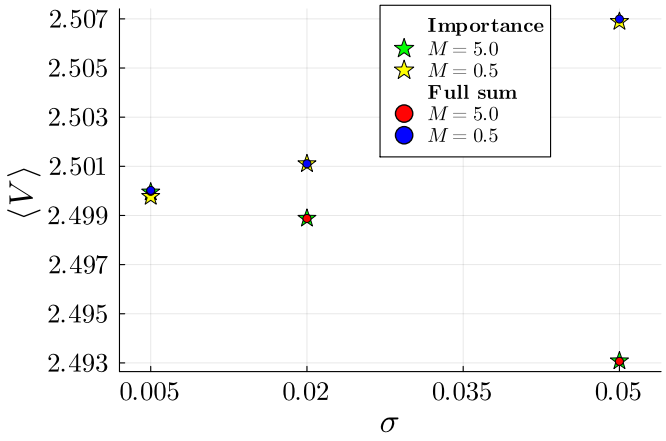

Figure 4.8: $\langle V \rangle$ computed using both importance sampling and full numerical integration.

4.2.2.2 Lattice size 20

Importance sampling enables the exploration of larger lattice sizes. In this section, we consider a one-dimensional lattice with 20 edges. For this system, 5×10^5 samples were extracted from $p = \prod_\nu P_\nu(l)$ to approximate all evaluations presented in this subsection.

As in Chapter 3, we begin by analyzing the distribution of geodesic distances R realized across the superposition of lattices. We recall that the frequency with which a given R occurs plays a crucial role in evaluating the relational correlation $\langle \phi\phi(R) \rangle$, since the delta function in equation (4.14) effectively weights the contribution of each sample according to how frequently that specific geodesic distance is realized in the ensemble of lattices. Figure 4.9a displays the histogram of R for two different values $\sigma = 0.05, 0.02$, with the mean fixed at $\mu = 0.5$. In this setup, the geodesic distance R is computed as the sum of edge lengths along the shortest path between any two vertices, with periodic boundary conditions imposed. It is also important to mention that the binning strategy described in the previous subsection is also implemented in this and all subsequent analyses, where we have grouped R into bins of size $[R, R + \delta R]$, which ensures correct statistical estimations, since in practice one encounters that without this step, even small numerical differences between distances would lead to artificially sparse statistics, thereby distorting the computed correlator $\langle \phi\phi(R) \rangle$.

From Figure 4.9a, we observe that the distribution of R exhibits multiple local maxima, occurring approximately at integer multiples of the mean value μ.

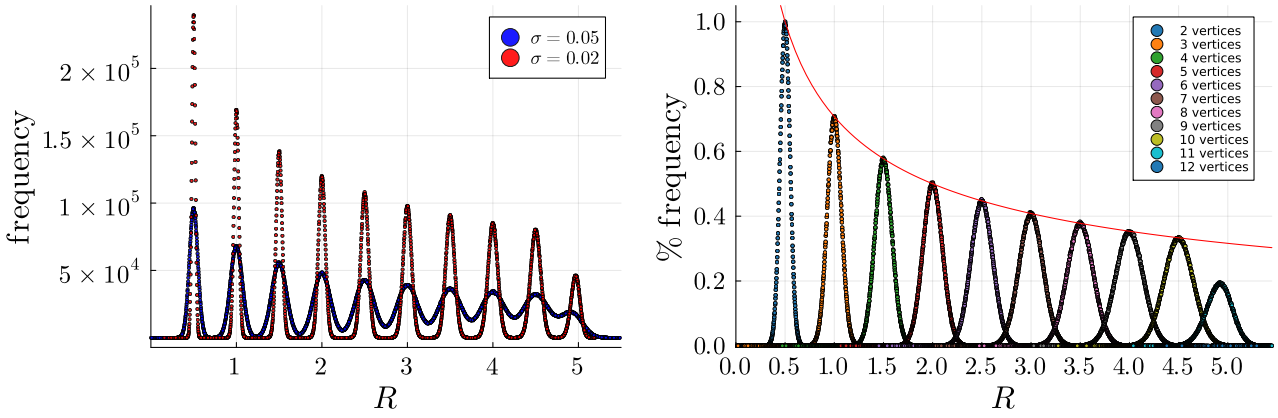

(a) (b)

Figure 4.9: Distribution of geodesic distances R across a superposition of one-dimensional lattices with 20 edges and periodic boundary conditions. These distances are grouped into bins of size $[R, R+\delta R]$. a) Histogram of R for fixed mean edge length $\mu = 0.5$, shown for two different values of $\sigma = 0.05, 0.02$. b) Histogram of R ($\mu = 0.5$, $\sigma = 0.05$) group by the number of edges composing each geodesic path. Each group is labeled by the number of vertices involved, where the number of vertices equals the number of edges plus one: #vertices = #edges + 1. The red curve represents the decay $\frac{1}{\sqrt{R}}$. We observe that the very last distribution on this figure gets smaller than predicted from this decay. This is due to the periodic boundary conditions of the lattice, since is really unlikely to realize paths with 11 edges or more in a lattice with 20 total edges.

This behavior can be understood by grouping the contributions to R according to the number of edges that constitute the shortest path, as illustrated in Figure 4.9b (shown here for the case $\sigma = 0.05$). If a given distance R is composed of k edges, and each edge length is independently sampled from the Gaussian distribution $P_\nu(l)$, then the sum of these k normally distributed variables is itself normally distributed, with parameters $\mu_T = k\mu$ and $\sigma_T^2 = k\sigma^2$. Therefore, the histogram of R can be interpreted as a superposition of several Gaussian distributions, each corresponding to a different number of edges k in the geodesic path. The observed peaks in Figure 4.9a can thus be interpreted as the dominant contributions from paths of fixed edge count k, centered around $R \approx k\mu$. Equally important is the decay rate of the frequency with which a given geodesic distance R is realized. Since each peak arises from the sum of k independent, normally distributed edge lengths, the height of the peak is controlled by the normalization factor of the resulting distribution, given by $\frac{1}{\sqrt{2\pi k\sigma^2}}$. Noting that $R \approx k\mu$, this implies the envelope of the peak amplitudes decays as $\sim \frac{1}{\sqrt{R}}$. This behavior is illustrated by the red curve in Figure 4.9b, which tracks the decay of the peak maxima as a function of R. It is worth noting that the distribution of distances R obtained via importance sampling exhibits an overall shape that differs from that of the full computations shown in Figure 4.2. This difference is expected,

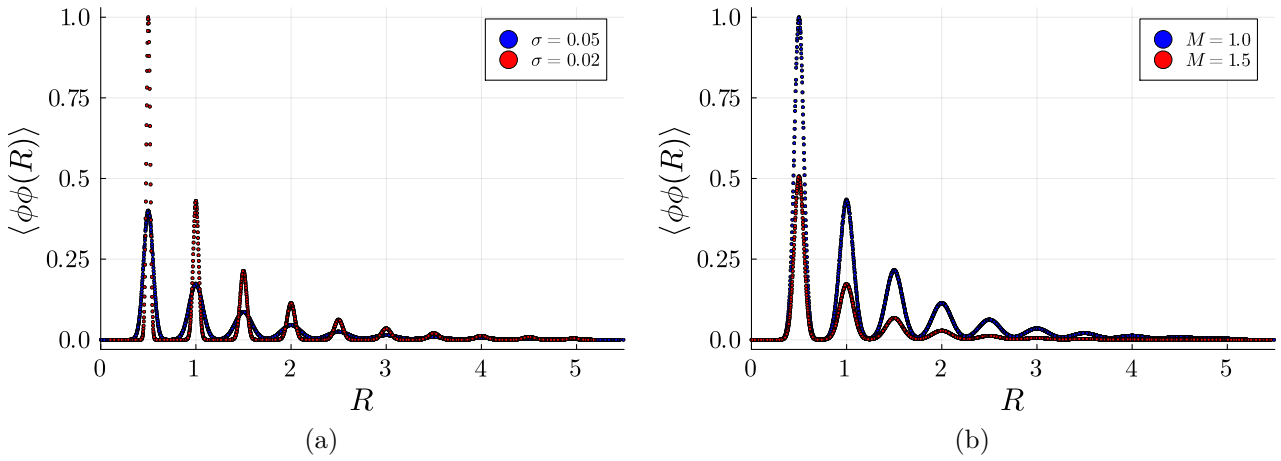

Figure 4.10: $\langle\phi\phi(R)\rangle$ in a superposition of lattices with 20 edges and periodical boundary conditions. a) Comparison of $\langle\phi\phi(R)\rangle$ for $\sigma = 0.05$ and $\sigma = 0.02$, with fixed $\mu = 0.5$ and $M = 1.0$. b) $\langle\phi\phi(R)\rangle$ for $M = 1.0$ and $M = 1.5$ with fixed $\sigma = 0.05$ and $\mu = 0.5$.

as the lattice sizes in the two cases are not the same, and the procedure for constructing the allowed edge lengths on the lattice also follows different prescriptions.

We now turn to the analysis of the relational correlation function $\langle\phi\phi(R)\rangle$. In Figure 4.10a, we compare the behavior of $\langle\phi\phi(R)\rangle$ for a fixed scalar field mass $M = 1.0$ and two different values of $\sigma = 0.05$ and $\sigma = 0.02$. We observe that reducing σ leads to a sharpening of the local maxima, which are located at multiples of the mean length $\mu = 0.5$. This behavior can be understood by examining the distribution of geodesic distances R shown in Figure 4.9a. For $\sigma = 0.02$, the distribution of edge lengths is more sharply peaked, resulting in a more concentrated and pronounced frequency of specific geodesic distances. As a result, more contributions are added to $\langle\phi\phi(R)\rangle$ at these distances compared to the broader distribution with $\sigma = 0.05$. Additionally, we observe a general decay in $\langle\phi\phi(R)\rangle$ as the geodesic distance R increases. This decay arises from two key factors: (i) the decreasing frequency with which larger values of R are realized across the ensemble of sampled lattices, and (ii) the exponential suppression of correlations encoded in the matrix K^{-1}_{ab}. As discussed earlier, the delta function in the definition of $\langle\phi\phi(R)\rangle$ weights the contributions according to how frequently each geodesic distance R appears. Consequently, local maxima in $\langle\phi\phi(R)\rangle$ correspond to the most probable distances, which coincide with the peaks in the histogram of R. At the same time, the field correlator K^{-1}_{ab} decays exponentially with increasing distance between vertices a and b, further suppressing contributions from larger separations.

In Figure 4.10b, we compare the relational correlation function $\langle\phi\phi(R)\rangle$ for fixed parameters $\sigma = 0.05$ and $\mu = 0.5$, considering two scalar field masses: $M = 1.0$ and $M = 1.5$. We observe that increasing the mass M results in a suppression of the overall amplitude of $\langle\phi\phi(R)\rangle$. This

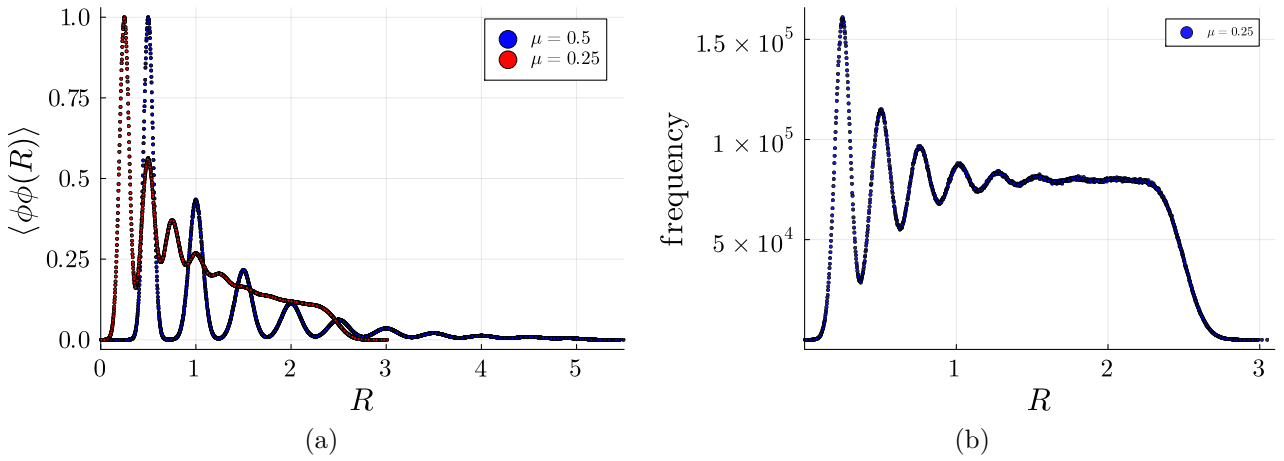

Figure 4.11: $\langle\phi\phi(R)\rangle$ for different values of μ. a) Comparasion of $\langle\phi\phi(R)\rangle$ for $\mu = 0.5$ and $\mu = 0.25$, with fixed $\sigma = 0.05$ and $M = 1.0$. b) Histogram of distances R for $\mu = 0.25$ and $\sigma = 0.05$.

behavior is due to the structure of K^{-1}_{ab}, which encodes the field correlations between vertices a and b. As the mass increases, these correlations decay more rapidly with distance, leading to an overall suppression in the correlation function.

We also examine the behavior of $\langle\phi\phi(R)\rangle$ as the mean value μ of the length distribution decreases. The results are shown in Figure 4.11a, where we fix $\sigma = 0.05$ and $M = 1.0$, and compare $\mu = 0.5$ and $\mu = 0.25$. We observe that the range of attainable geodesic distances R is significantly reduced in the case $\mu = 0.25$, due to the fact that the average edge length is now smaller. Consequently, the total physical size of the lattice shrinks on average. This behavior is further clarified by analyzing the distribution of geodesic distances R, shown in Figure 4.11b for $\mu = 0.25$. As the mean of the length distribution shifts toward smaller values (while keeping $\sigma = 0.05$ fixed), the local maxima of the histogram broaden, and the overall distribution flattens for intermediate distances. As a result, the frequency of geodesic distances around $R \sim 1.5$ becomes nearly uniform. Notably, the profile of $\langle\phi\phi(R)\rangle$ in Figure 4.11a resembles that observed in Chapter 3, particularly in Figure 3.20b.

Finally, we compute $\langle\phi\phi(R)\rangle$ in the limit $\sigma \to 0$, in which every edge length in the lattice is fixed to the mean value $\mu = 0.5$. The result, shown in Figure 4.12, effectively recovers the standard exponential decay of correlations known from lattice field theory. In this limit, the frequency of geodesic distances R becomes uniform across all values, and each R receives an equal number of contributions. The green curve in Figure 4.12 represents the exponential decay $\exp(-M \cdot R)$, as expected from a massive scalar field on a regular lattice. For comparison, we also show in Figure 4.12 the case with $\sigma = 0.05$, $\mu = 0.5$, and $M = 1.0$. The red curve in this

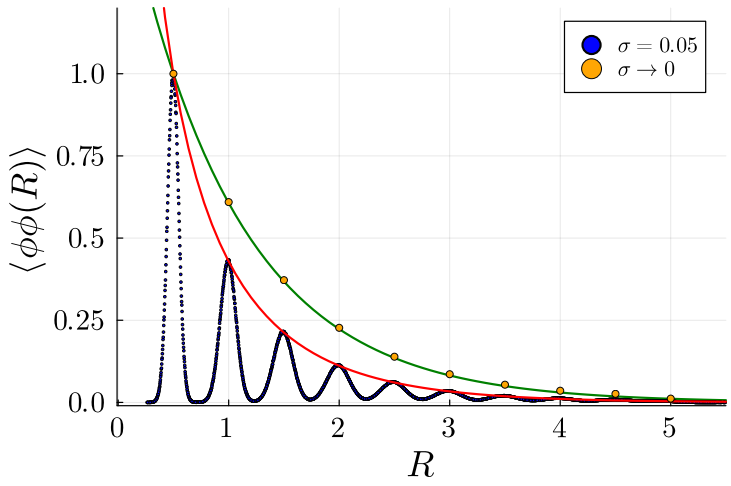

Figure 4.12: $\langle \phi\phi(R) \rangle$ in the limit $\sigma \to 0$, with fixed parameters $\mu = 0.5$ and $M = 1.0$. In this limit, all edge lengths are sharply peaked at the mean value μ, resulting in a fixed lattice spacing. Consequently, $\langle \phi\phi(R) \rangle$ reduces to the standard two-point correlation function from lattice field theory. The green curve in Figure 4.12 illustrates the exponential decay of these correlations, given by $\exp(-M \cdot R)$. For comparison, we also plot $\langle \phi\phi(R) \rangle$ for $\sigma = 0.05$, with the same values $\mu = 0.5$ and $M = 1.0$. The red curve represents the decay $\sim \frac{\exp(-M \cdot R)}{\sqrt{R}}$, which encodes both geometric and matter information.

figure captures the combined suppression due to both the frequency of R (as seen in Figure 4.9, which scales as $\sim \frac{1}{\sqrt{R}}$) and the exponential decay from the matter correlations. This combined behavior is well approximated by:

$$\frac{\exp(-M \cdot R)}{\sqrt{R}} \,. \tag{4.15}$$

The above scaling accurately describes the amplitude envelope of the relational correlation and shows explicitly how $\langle \phi\phi(R) \rangle$ encodes both geometric and matter-related information given by the interplay between the exponential suppression from the matter correlations and the statistical distribution of geodesic distances across the superposition of lattices.

On the purely geometric side, we evaluate the expectation value of the total volume, $\langle V \rangle$, as shown in Figure 4.13a. This figure compares $\langle V \rangle$ for different values of the scalar field mass M and distribution width σ, while keeping the mean length fixed at $\mu = 0.5$. As expected, the total volume is approximately 10, since the lattice contains 20 edges, each on average close to the mean length $\mu = 0.5$. However, a general trend emerges, since increasing the mass M leads to a slight reduction in the total volume. This behavior can be understood from the expression for $\langle V \rangle$ in eq. (4.13), where the mass M enters in the denominator through $\det K$. As M increases, $\det K$ grows, which in turn slightly suppresses the expectation value

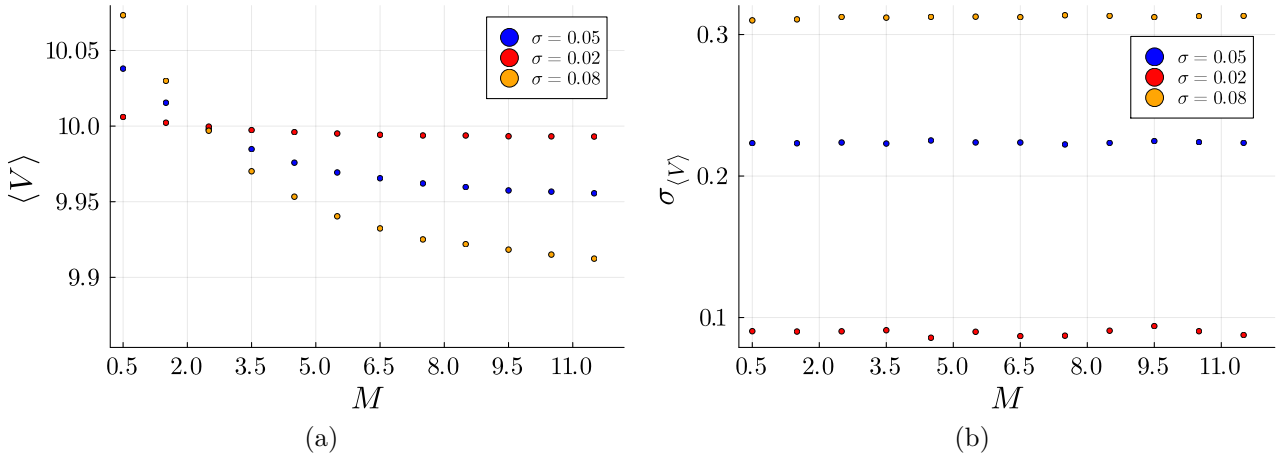

Figure 4.13: $\langle V \rangle$ for different values of σ and M. a) $\langle V \rangle$ for $\mu = 0.5$. b) Variance of $\langle V \rangle$.

$\langle V \rangle$. Furthermore, Figure 4.13a shows that smaller values of σ result in volumes that are more tightly peaked around the expected value of 10. This is because narrower distributions concentrate the edge lengths closer to the mean $\mu = 0.5$. In contrast, broader distributions (larger σ) allow for a wider range of length values, increasing variability in the total volume. To quantify this variability, Figure 4.13b displays the standard deviation of $\langle V \rangle$. We observe that varying the mass M has negligible impact on the standard deviation. However, increasing σ significantly enlarges the spread, since a broader distribution introduces more fluctuation in the sampled edge lengths, and thus in the total volume across the ensemble of lattices.

4.3 Discussion on numerical results

In this chapter, we investigated a toy model: a free massive scalar field defined on a dynamical lattice. This system serves as an analogue to the one explored in Chapter 3, where the probability of a given lattice configuration is determined by the semiclassical amplitude of the restricted spin foam model. The main motivation for constructing this toy model was twofold. First, it allowed us to develop and test computational tools suited to systems whose evaluation suffers from exponential complexity. Second, it provided a controlled setting to tackle a key challenge in background-independent systems: how to define and extract *meaningful* observables without a fixed geometry. Thus, at the heart of our investigation lies the definition and evaluation of the *relational* correlation function $\langle \phi\phi(R) \rangle$. Its appeal lies in its seemingly natural definition: correlating field values as a function of geodesic distance rather than coordinate labels. This definition makes it a promising candidate for capturing physically relevant information in background-independent frameworks. Being the first explicit evaluation of such an object, we approached it from different computational perspectives, aiming to probe its individual compo-

nents and better understand its structure. A priori, the only guidelines for interpreting $\langle\phi\phi(R)\rangle$ come from its two building blocks: (i) the two-point correlations encoded in the matrix K, and (ii) the distribution of lengths, which determines the probability of different geometries. From this perspective, we expect the relational correlations to reflect two intertwined effects: On one hand, the decay of field correlations with distance, as in standard lattice field theory, although in our case this is not guaranteed since the lattice spacing is not fixed. On the other hand, some distances across the lattices are more probable than other, given the nature of the underlying distribution of lengths that favor those around the mean value. Thus, this alone, suggests that $\langle\phi\phi(R)\rangle$ should be enhanced in regions where R is more probable, and suppressed otherwise.
To test the above ideas, the one-dimensional model proved especially useful. Its limited number of degrees of freedom allows explicit evaluations on small lattices and comparison with the more complex system of Chapter 3. For instance, in this simplified system, we could include *all* admissible distances R in the full summation, which provides a clearer picture of how probability weighting of the underlying geometry influences the relational correlations. These effects became particularly transparent in the importance sampling approach, where distances R with higher geometric probability were explicitly sampled more often, and correspondingly, the relational correlator was observed to be larger in those regions. Moreover, the explicit evaluations agreed closely with the importance sampling results for both geometric and matter observables, indicating that importance sampling is a powerful numerical strategy for this type of system. Thus, these findings open the door to applying similar techniques in higher-dimensional, more complex models.
As another important lesson from the importance sampling study was the necessity of binning the sampled lengths. Defining a minimal resolution for when two lengths are considered indistinguishable is essential, without it, the measured distribution of lengths fails to reproduce the expected sampling distribution.
Through this numerical analysis, we have gained valuable insights into both the strengths and limitations of the relational correlation function, which we now summarize:

- **Cutoff dependence of $\langle\phi\phi(R)\rangle$**
  Our definition of the relational correlator $\langle\phi\phi(R)\rangle$ involves integrating over all distances (metrics) and all pairs of vertices (coordinates), effectively removing any dependence on coordinate labels and averaging only over correlators separated by a fixed geodesic distance R. While conceptually appealing, this definition introduces a subtle but significant issue: the frequency with which a given geodesic distance R appears across the ensemble of geometries becomes a key factor in the final result. Given that the underlying geometries are directly linked to the amplitudes given by the underlying spacetime model, then some configurations are naturally favored over others. In practice, this introduces a

form of cutoff dependence. This is particularly evident in the full numerical evaluations, where upper and lower bounds on edge lengths directly affect the distribution of geodesic distances and, consequently, the number of contributions to $\langle\phi\phi(R)\rangle$. As a result, this observable in its current form is sensitive to arbitrary cutoff choices, and refining its definition is essential to ensure well-posed, cutoff independent results.

- **Distribution of geodesic distances**
  Closely related to the above, we stress the importance of the distribution of geodesic distances R, which plays a critical role in determining the behavior of the relational correlator. When using importance sampling, the shape of this distribution differs markedly from that observed in the full computations. Although importance sampling offers a clearer geometric interpretation of how these distances arise, it also reveals that different sampling strategies can yield significantly different R-distributions, thereby affecting the resulting correlations. Thus, potential artifacts due to the choice of sampling method are not discard, although in our study explicit evaluations and importance sampling show close agreement. Closely related, given that the sampling procedure is not unique, one can try for instance random (uniform) sampling as an alternative. However, preliminary attempts to use this method (unreported on this work) suggested a stronger cutoff dependency, similar to the one we reported in this work on the explicit evaluation case: in the uniform sampling case, the range over which samples are drawn effectively acts like a hidden integration boundary, which reproduces similar cutoff dependent results. This outcome is traced from a similar R distribution as in the case of the explicit evaluations. Hence, both full numerical and sampling approaches expose a dependence of $\langle\phi\phi(R)\rangle$ on how the geodesic distances are realized, which highlights the need for a more robust definition.

- **Emergence of new scaling behavior**
  On a more positive note, our studies in the particular model we explored, uncovered a novel behavior in the relational correlator. Specifically, we found that $\langle\phi\phi(R)\rangle$ effectively captures both geometric and matter content, exhibiting a characteristic scaling of the form:
  $$\sim \frac{\exp(-M \cdot R)}{\sqrt{R}}\,.$$
  This form reveals how the correlator simultaneously reflects the exponential decay expected from a massive scalar field and the statistical weight of geometries contributing to a given distance R. This contrasts with standard lattice field theory, where the lattice structure is fixed and the correlator decays purely exponentially. Furthermore, in the limit where the superposition of geometries reduces to a single, regular lattice (i.e.,

fixed lattice spacing), the relational correlator smoothly reduces to the familiar two-point function of lattice field theory. Thus, this shows the potential of this object to capture meaningful information in background independent systems.

Finally, our findings underscore both the promise and the challenges of defining observables in background independent frameworks. Naturally, going forward, requires refining the definition of relational observables and extending these techniques to more realistic spin foam models.

Conclusions and Outlook

In this work, we explored the coupling of a free massive scalar field to a restricted spin foam model in the semiclassical limit and a *toy model*, defined as a free massive scalar field on an irregular, dynamical one-dimensional lattice. The main motivation to explore such systems in this project is to tackle the challenge of defining *meaningful* observables in background-independent settings. In such a scenario, the two-point correlation from lattice field theory lacks a meaningful interpretation, since, in a background-independent framework, the vertices of the underlying lattice are merely labels without intrinsic spatial meaning, and their separation is not predetermined but integrated over as part of a superposition of geometries in the spin foam path integral. In this context, the shift to *relational* observables becomes essential. In this framework, meaningful physical quantities arise not from evaluating a field at a fixed coordinate location (which is inherently diffeomorphism-dependent), but from specifying the value of one dynamical variable when another takes a given value. Thus, given that it makes little sense to talk about the behavior of $\langle\phi(x)\phi(y)\rangle$ as a function of the *coordinate* distance between x and y, since these quantities lack a diffeomorphism-invariant meaning, we proposed a *relational* correlation function $\langle\phi\phi(R)\rangle$ in *relation* to the geodesic distance R. This object circumvents the challenges of the standard two-point correlation function by integrating the correlation of fields for all possible realizations of the geodesic distance R, i.e., for all pairs of coordinates and all metrics. To test the consequences, strengths, and limitations of our proposed *relational* correlation function, in this work we proceed as follows:

In Chapter One, we defined the discrete exterior calculus techniques that allow us to define a free massive scalar field on irregular settings. Thus, discrete exterior calculus serves as a versatile framework that allows us to go beyond regular discrete settings. In Chapter Two, we defined our restricted EPRL-FK model in the semiclassical limit. This is achieved by restricting the EPRL-FK state sum to a particular set of intertwiners, namely, *quantum cuboid* intertwiners [34]. This restriction yields a superposition of flat, hypercuboidal lattices weighted by spin foam amplitudes. The resulting model has far fewer degrees of freedom and substantial symmetry, making the state sum significantly more tractable. In particular, the non-oscillatory nature of the semiclassical amplitude of this model allows the implementation of numerical

techniques such as Markov Chain Monte Carlo methods. In Chapter Three, we defined the coupling of the free massive scalar field with our restricted spin foam model. Using the dataset generated in [36], we revisited the geometric and matter observables of this system. Our analysis of geometric observables introduced a binning strategy for classifying lengths and distances R, an approach that departs from the treatment in [36]. This analysis reproduced outcomes similar to those reported in [36]: the total volume $\langle V \rangle$ remains finite where the parameter α (which takes part in the face amplitude of our restricted spin foam model) lies in the range $\alpha \in [0.63, 0.67]$. In this same region, the distribution of lengths shows a peak profile structure determined by the spin foam plus matter amplitude. On the matter side, in our numerical treatment, we found that the expectation value of the two-point correlation function behaves, to good approximation, like that of a scalar field on a regular lattice with a dynamical lattice spacing emerging from the peak structure of the coupled amplitude. Using both Euclidean and Manhattan metrics to compute distances R yielded similar values of the computed effective mass, extracted from the respective exponential fitting. Additionally, a close match between the effective mass and that of the scalar field M was observed. Although these results closely follow the findings in [36], our numerical treatment takes into account the frequency at which the geodesic distance is realized in the underlying geometry to average all correlators located at this geodesic distance; thereby, effectively turning the correlator into a genuine expectation value.

Furthermore, at the core of Chapter 3, we introduced and evaluated, for the first time, a *relational* correlation function $\langle \phi\phi(R) \rangle$, designed to provide diffeomorphism-invariant information by correlating field values in *relation* to the geodesic distance R. Our results clearly show that this observable captures the interplay between matter correlations and the probability of realizing a given distance R. Although we observe that, as the value of α increases and larger values of R are probed, the variance of the computations grows, indicating that additional data are needed to achieve convergence in most cases across all three lattice sizes explored in this work. Nonetheless, at this stage, our *relational* correlation function gives first insights into the nature of this object.

Despite these encouraging results, our analysis relies on several simplifying assumptions. The restriction to quantum cuboids and the semiclassical limit leaves out the full complexity of spin foam dynamics. Moving beyond these approximations will require tackling the oscillatory nature of spin foam amplitudes, a challenge for which standard Monte Carlo methods are often insufficient, although promising progress has been made [92, 93]. Looking ahead, two main research directions emerge. First, extending the matter-coupling framework to more general geometries and to spin foam amplitudes that allow curvature. Second, exploring interactions with richer matter sectors, such as gauge fields or fermions, while maintaining numerical tractabil-

ity. This present work should therefore be seen as a first step toward connecting simplified spin foam models with realistic, dynamically coupled matter systems.

To gain further insight into the relational correlation function and to test numerical strategies, we developed a *toy model* in Chapter Four: a free massive scalar field defined on a dynamical, irregular one-dimensional lattice. This model allows us to control the degrees of freedom by assuming a Gaussian amplitude for each edge length in the lattice. This simplification allows us to perform explicit evaluations on small lattices and directly test importance sampling methods. We found that importance sampling over lengths reproduces results consistent with full explicit evaluations, demonstrating that a purely length-based definition of the coupled system captures both matter and geometric information. This approach departs from [36], where the coupling was defined in terms of both fields and lengths, requiring more involved numerical computations. Moreover, the importance sampling method gave a clearer interpretation of $\langle\phi\phi(R)\rangle$: distances composed of edge lengths with higher probability occur more frequently and contribute more strongly to the correlator, thereby the correlations are higher at those distances that are more probable. Furthermore, the relational correlation function in this model exhibits a decay structure different from a pure exponential: it reflects both the standard matter-field decay and the statistical weighting of geometries contributing to a given R. Of particular relevance to our *relational* correlation function is the consistency check achieved by recovering the standard two-point correlation function in the limit of a lattice with constant spacing. At the same time, our *toy model* highlighted several limitations. The relational correlation function is sensitive to the choice of sampling strategy and, in its present form, depends on arbitrary cutoffs. Thus, these issues must be addressed to obtain well-posed, cutoff-independent results. Future work on this model should aim to generalize it to higher dimensions, particularly four-dimensional settings, and to investigate couplings with other matter types, such as gauge fields and fermions. The numerical efficiency of the importance sampling approach also opens the door to studying systems with significantly higher degrees of freedom, potentially bridging this laboratory model with the spin foam framework.

Appendix A

Intertwiners in a nutshell

In this appendix, we discussed briefly some mathematical properties of the intertwiners that take part on spin foam models.

Given two representations D_1 and D_2 of a group G, acting on vector spaces V and W respectively, an intertwiner between D_1 and D_2 is a linear operator $\iota : V \longrightarrow W$ which commute with G, in the sense that $\iota D_1(g) = D_2(g)\iota$ for all $g \in G$. The space of intertwiners, denoted $\mathrm{Hom}_G(V, W)$, is a subspace of the vector space of linear maps $\mathrm{Hom}(V, W)$. The intertwining linear maps play an important role in the description of the space of invariant elements of the support of a representation. Consider the projector:

$$\begin{aligned} P : V &\to \mathrm{Inv}_G(V) \\ v &\mapsto \left(\int_G dg\, \rho(g)\right) v \end{aligned} \tag{A.1}$$

where ρ is a unitary representation of G, dg is the bi-variant Haar mesuare [64] and

$$\mathrm{Inv}_G\,(V) := \{\psi \in V \mid g \cdot \psi = \psi \ \ , \forall g \in G\} \ \ ,$$

denotes the set of invariant elements of ρ. The image of P is in $\mathrm{Inv}(\mathcal{H})$ because the measure is bi-invariant :

$$\rho(h)\left(\int_G dg\, \rho(g)\right) v = \left(\int_G dg\, \rho(hg)\right) v = \left(\int_G dg\, \rho(g)\right) v.$$

Moreover, the map P is indeed a projector, since for the exact same reason it holds that $P^2 = P$.

A powerful and frequently used result is the relation between the space of intertwiners and the space of invariant elements given by the isomorphism [66]:

$$\mathrm{Hom}_G(V, W) \cong \mathrm{Inv}_G(V \otimes W^*)\,, \tag{A.2}$$

where W^* is the dual space of W .

If $\{|\iota\rangle\}$ is an orthonormal basis of $\mathrm{Inv}_G(V)$, then the projector admits the following resolution of identity:

$$P = \sum_{\iota} |\iota\rangle\langle\iota|\,.$$

That is, P can be expanded in terms of an orthonormal intertwiners basis $\{|\iota\rangle\}$. The explicit form of this basis can be constructed using recoupling theory [67].

Appendix B

Two-Point correlation (plots)

B.1 Lattice size $N_1 = 81$, Euclidean metric

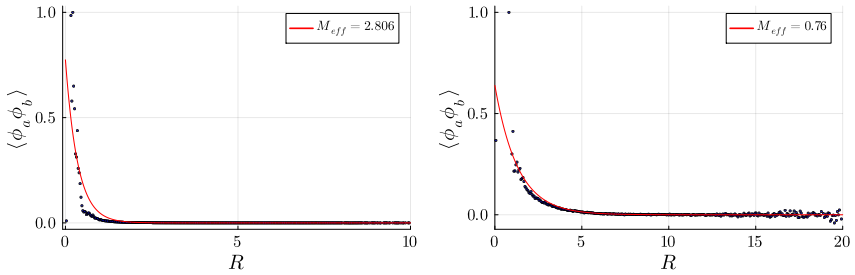

(a) $\alpha = 0.63$ (b) $\alpha = 0.64$

(c) $\alpha = 0.65$ (d) $\alpha = 0.66$

Figure B.1: Two-point correlation $\langle \phi_a \phi_b \rangle$ as function of the Euclidean geodesic distance R, for different values of α, $M = 0.5$ and lattice size $N_1 = 81$.

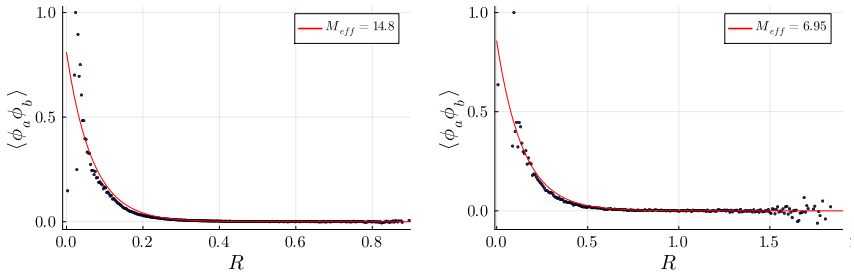

(a) $\alpha = 0.63$ (b) $\alpha = 0.64$

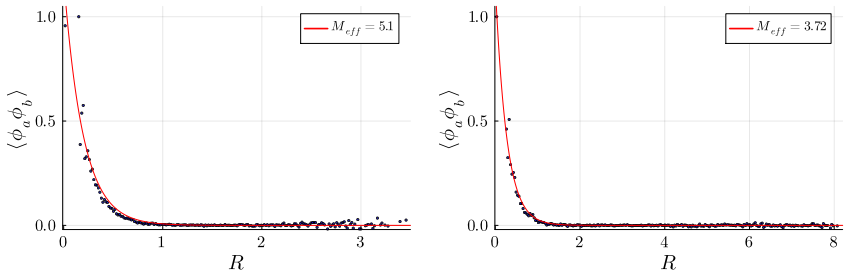

(c) $\alpha = 0.65$ (d) $\alpha = 0.66$

Figure B.2: Two-point correlation $\langle \phi_a \phi_b \rangle$ as function of the Euclidean geodesic distance R, for different values of α, $M = 5.0$ and lattice size $N_1 = 81$.

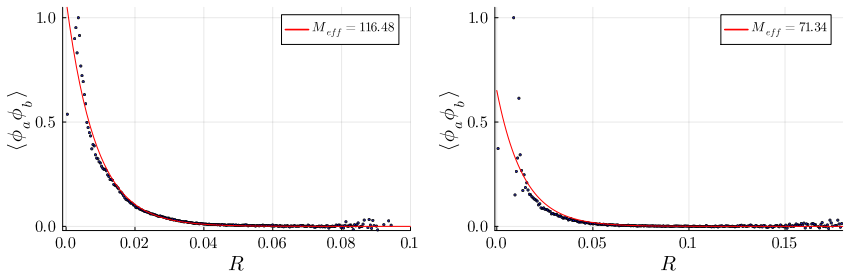

(a) $\alpha = 0.63$ (b) $\alpha = 0.64$

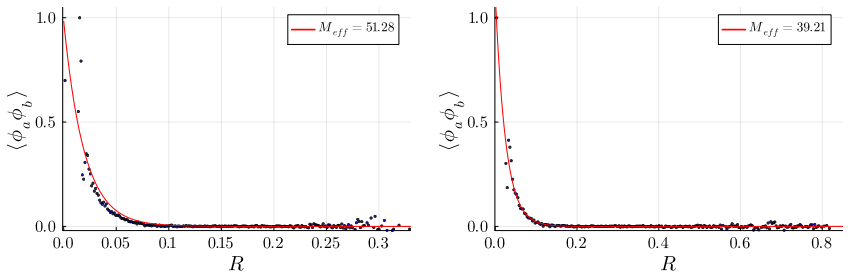

(c) $\alpha = 0.65$ (d) $\alpha = 0.66$

Figure B.3: Two-point correlation $\langle \phi_a \phi_b \rangle$ as function of the Euclidean geodesic distance R, for different values of α, $M = 50.0$ and lattice size $N_1 = 81$.

B.2 Lattice size $N_1 = 81$, Manhattan metric

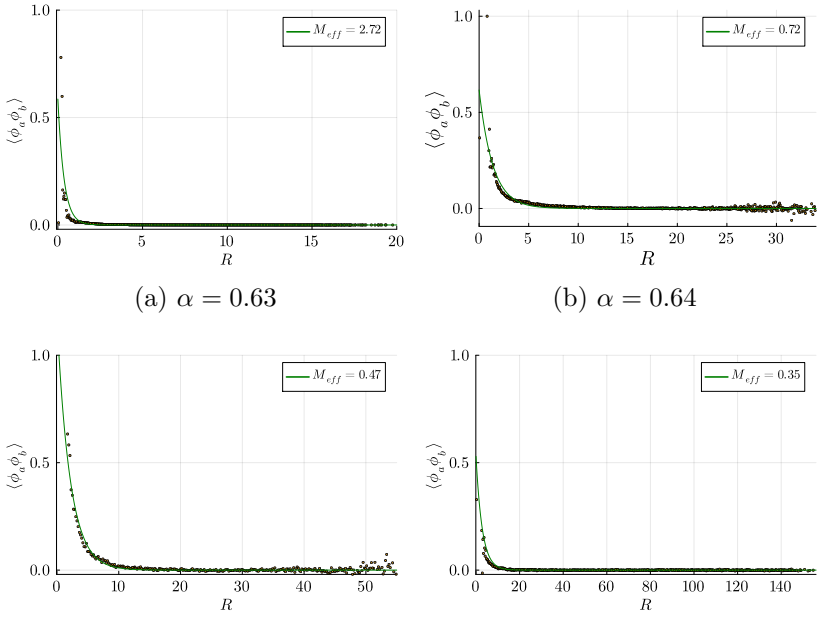

(a) $\alpha = 0.63$ (b) $\alpha = 0.64$

(c) $\alpha = 0.65$ (d) $\alpha = 0.66$

Figure B.4: Two-point correlation $\langle \phi_a \phi_b \rangle$ as function of the Manhattan geodesic distance R, for different values of α, $M = 0.5$ and lattice size $N_1 = 81$.

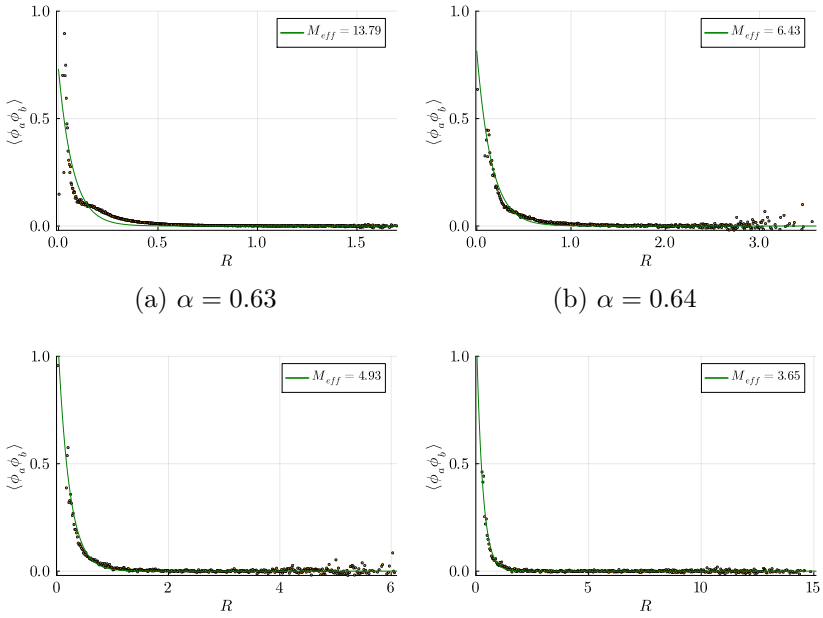

(a) $\alpha = 0.63$ (b) $\alpha = 0.64$

(c) $\alpha = 0.65$ (d) $\alpha = 0.66$

Figure B.5: Two-point correlation $\langle \phi_a \phi_b \rangle$ as function of the Manhattan geodesic distance R, for different values of α, $M = 5.0$ and lattice size $N_1 = 81$.

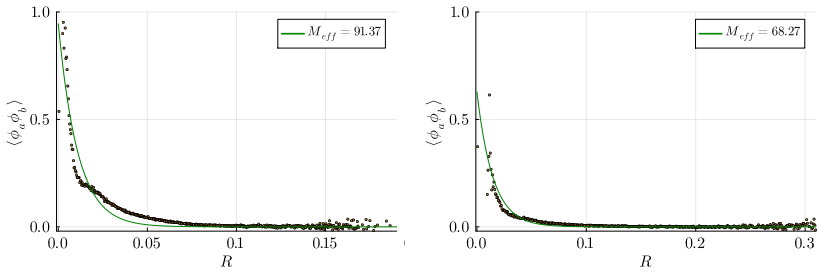

(a) $\alpha = 0.63$ (b) $\alpha = 0.64$

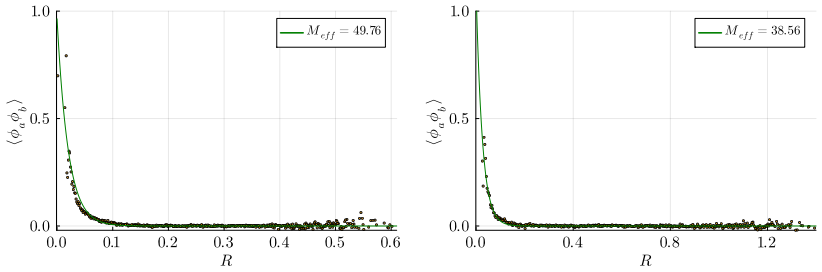

(c) $\alpha = 0.65$ (d) $\alpha = 0.66$

Figure B.6: Two-point correlation $\langle \phi_a \phi_b \rangle$ as function of the Manhattan geodesic distance R, for different values of α, $M = 50.0$ and lattice size $N_1 = 81$.

B.3 Lattice size $N_2 = 256$, Euclidean metric

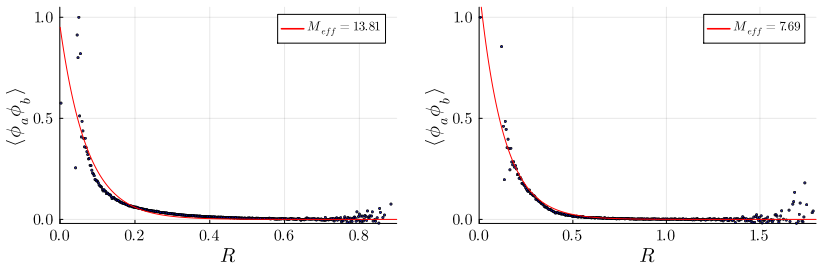

(a) $\alpha = 0.63$ (b) $\alpha = 0.64$

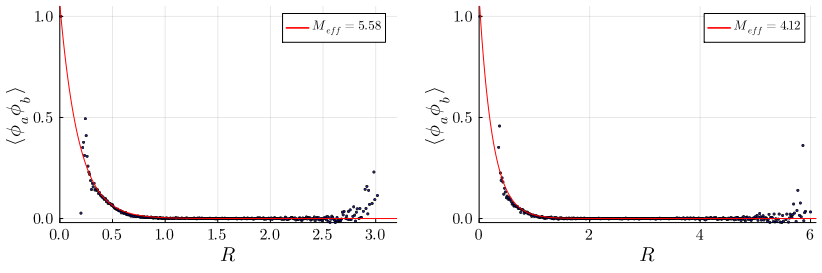

(c) $\alpha = 0.65$ (d) $\alpha = 0.66$

Figure B.7: Two-point correlation $\langle \phi_a \phi_b \rangle$ as function of the Euclidean geodesic distance R, for different values of α, $M = 5.0$ and lattice size $N_2 = 256$.

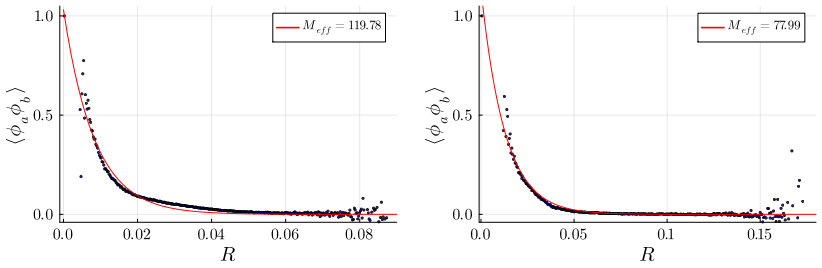

(a) $\alpha = 0.63$ (b) $\alpha = 0.64$

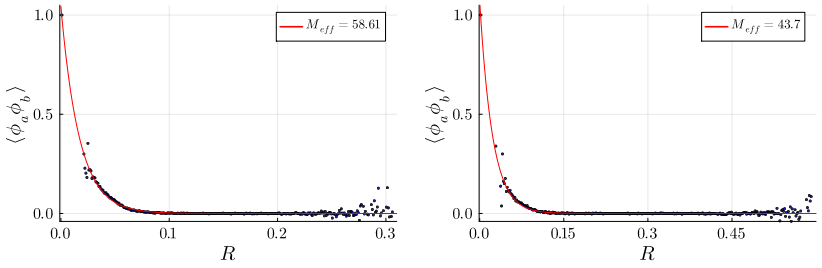

(c) $\alpha = 0.65$ (d) $\alpha = 0.66$

Figure B.8: Two-point correlation $\langle \phi_a \phi_b \rangle$ as function of the Euclidean geodesic distance R, for different values of α, $M = 50.0$ and lattice size $N_2 = 256$.

B.4 Lattice size $N_2 = 256$, Manhattan metric

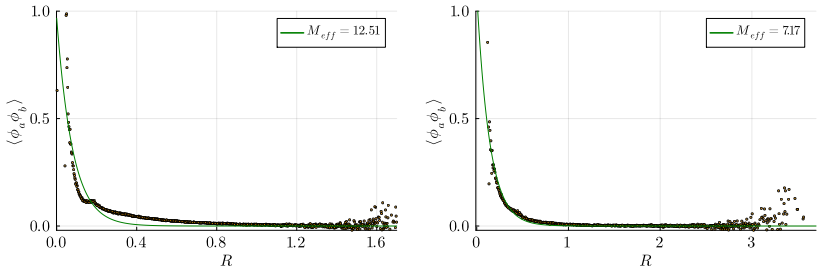

(a) $\alpha = 0.63$ (b) $\alpha = 0.64$

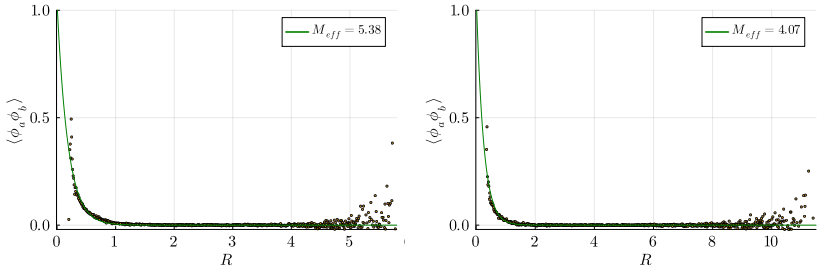

(c) $\alpha = 0.65$ (d) $\alpha = 0.66$

Figure B.9: Two-point correlation $\langle \phi_a \phi_b \rangle$ as function of the Manhattan geodesic distance R, for different values of α, $M = 5.0$ and lattice size $N_2 = 256$.

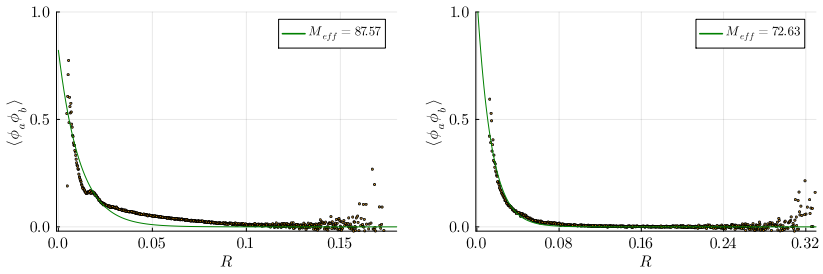

(a) $\alpha = 0.63$ (b) $\alpha = 0.64$

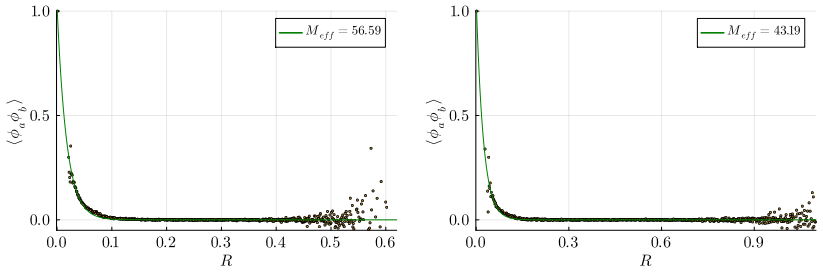

(c) $\alpha = 0.65$ (d) $\alpha = 0.66$

Figure B.10: Two-point correlation $\langle \phi_a \phi_b \rangle$ as function of the Manhattan geodesic distance R, for different values of α, $M = 50.0$ and lattice size $N_2 = 256$.

B.5 Lattice size $N_3 = 625$, Euclidean metric

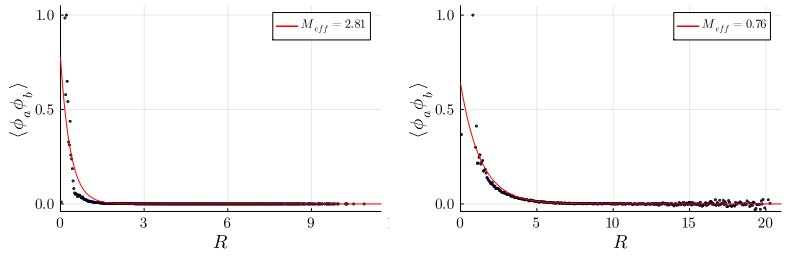

(a) $\alpha = 0.63$ (b) $\alpha = 0.64$

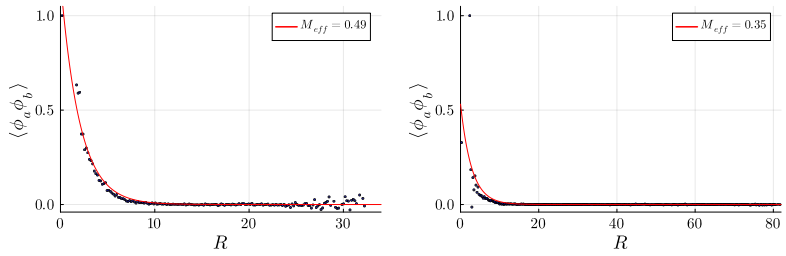

(c) $\alpha = 0.65$ (d) $\alpha = 0.66$

Figure B.11: Two-point correlation $\langle \phi_a \phi_b \rangle$ as function of the Euclidean geodesic distance R, for different values of α, $M = 0.5$ and lattice size $N_3 = 625$.

B.6 Lattice size $N_3 = 625$, Manhattan metric

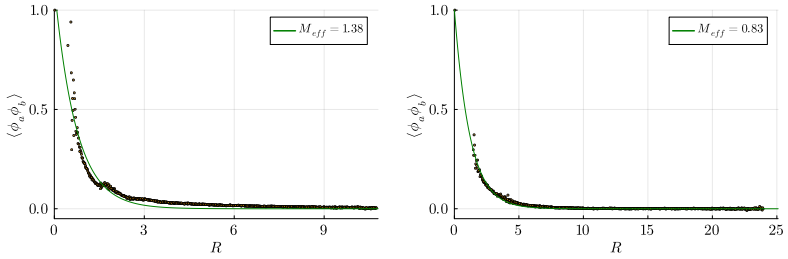

(a) $\alpha = 0.63$ (b) $\alpha = 0.64$

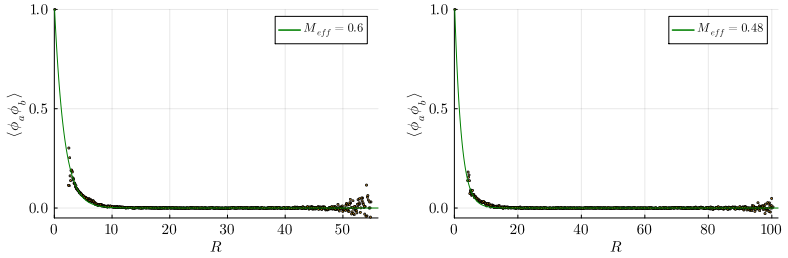

(c) $\alpha = 0.65$ (d) $\alpha = 0.66$

Figure B.12: Two-point correlation $\langle \phi_a \phi_b \rangle$ as function of the Manhattan geodesic distance R, for different values of α, $M = 0.5$ and lattice size $N_3 = 625$.

Appendix C

Distribution of R (plots)

C.1 Lattice size $N_1 = 81$

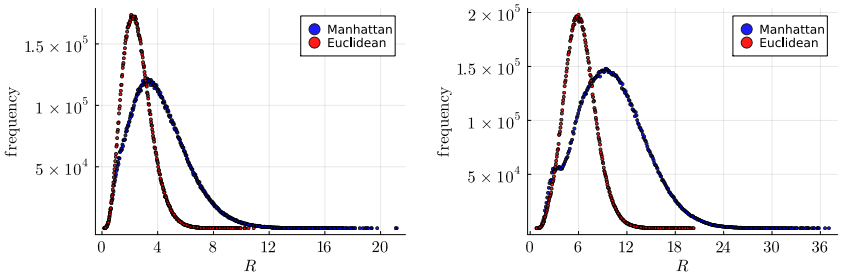

(a) $\alpha = 0.63$ (b) $\alpha = 0.64$

(c) $\alpha = 0.65$ (d) $\alpha = 0.66$

Figure C.1: Distribution of distances R, for different values of α. $M = 0.5$ and lattice size $N_1 = 81$.

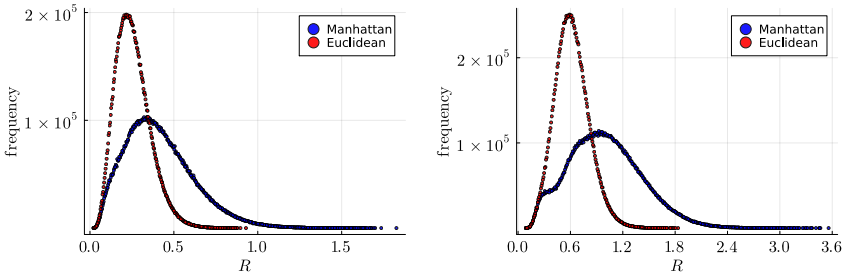

(a) $\alpha = 0.63$ (b) $\alpha = 0.64$

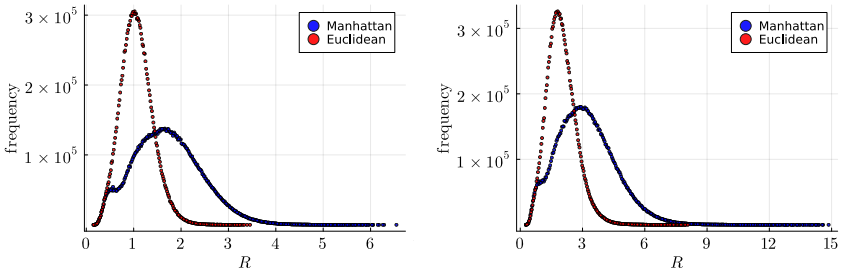

(c) $\alpha = 0.65$ (d) $\alpha = 0.66$

Figure C.2: Distribution of distances R, for different values of α. $M = 5.0$ and lattice size $N_1 = 81$.

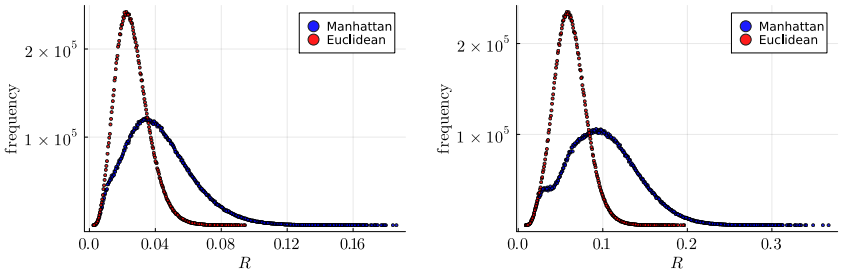

(a) $\alpha = 0.63$ (b) $\alpha = 0.64$

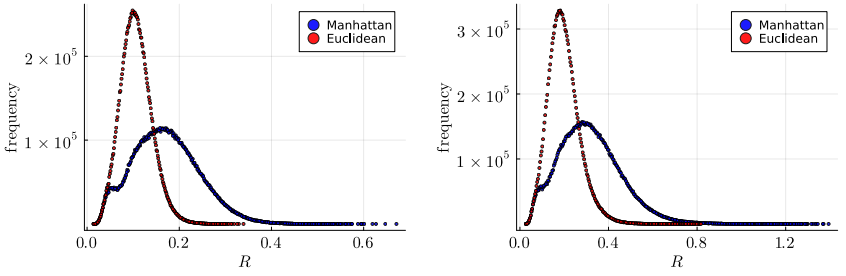

(c) $\alpha = 0.65$ (d) $\alpha = 0.66$

Figure C.3: Distribution of distances R, for different values of α. $M = 50.0$ and lattice size $N_1 = 81$.

C.2 Lattice size $N_2 = 256$

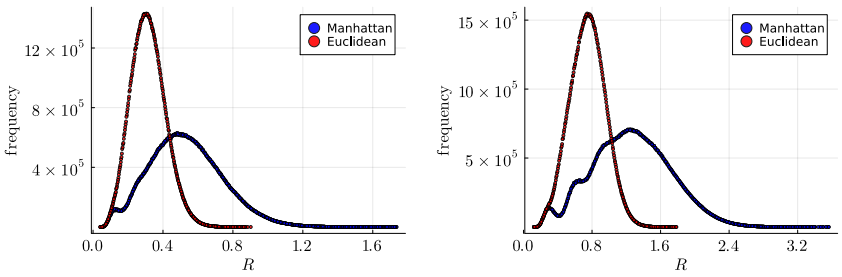

(a) $\alpha = 0.63$ (b) $\alpha = 0.64$

(c) $\alpha = 0.65$ (d) $\alpha = 0.66$

Figure C.4: Distribution of distances R, for different values of α. $M = 5.0$ and lattice size $N_2 = 256$.

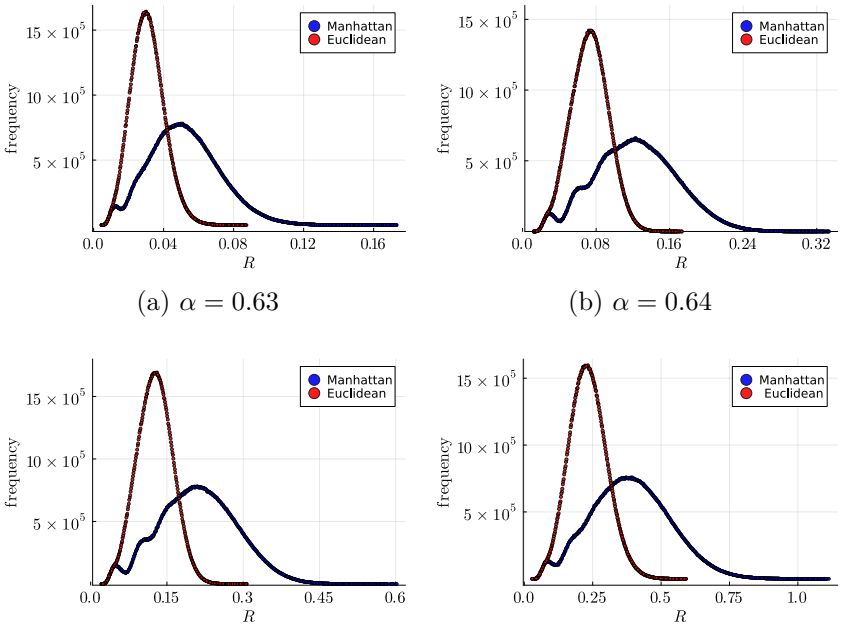

(a) $\alpha = 0.63$ (b) $\alpha = 0.64$

(c) $\alpha = 0.65$ (d) $\alpha = 0.66$

Figure C.5: Distribution of distances R, for different values of α. $M = 50.0$ and lattice size $N_2 = 256$.

C.3 Lattice size $N_3 = 625$

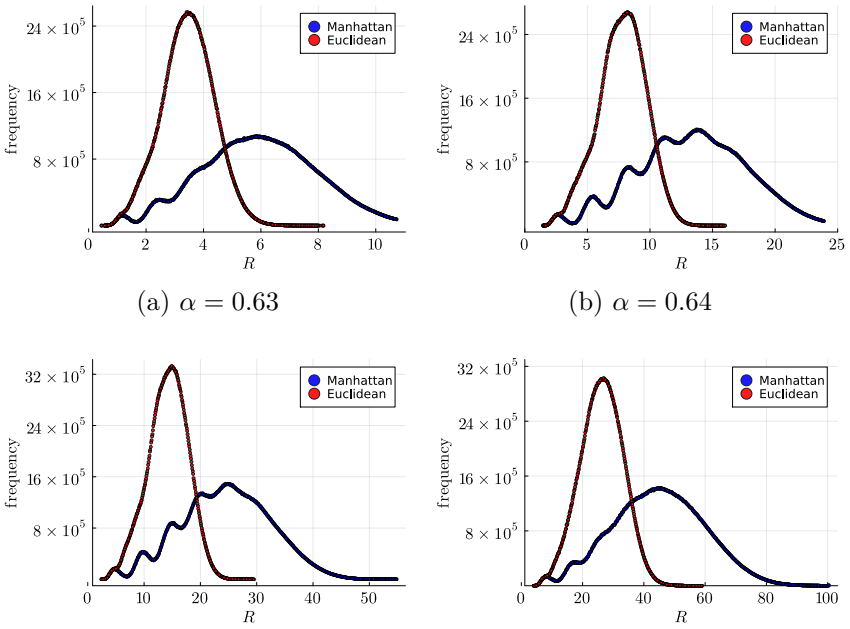

(a) $\alpha = 0.63$ (b) $\alpha = 0.64$

(c) $\alpha = 0.65$ (d) $\alpha = 0.66$

Figure C.6: Distribution of distances R, for different values of α. $M = 0.5$ and lattice size $N_3 = 625$.

Appendix D

Relational correlation: $\langle\phi\phi(R)\rangle$ (plots)

D.1 Lattice size $N_1 = 81$

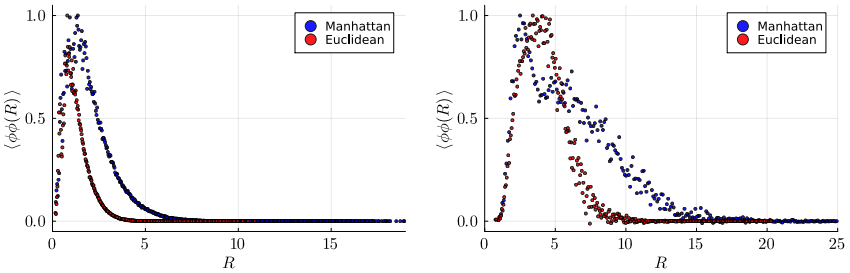

(a) $\alpha = 0.63$ (b) $\alpha = 0.64$

(c) $\alpha = 0.65$ (d) $\alpha = 0.66$

Figure D.1: Relational correlation function $\langle\phi\phi(R)\rangle$, for different values of α. $M = 0.5$ and lattice size $N_1 = 81$.

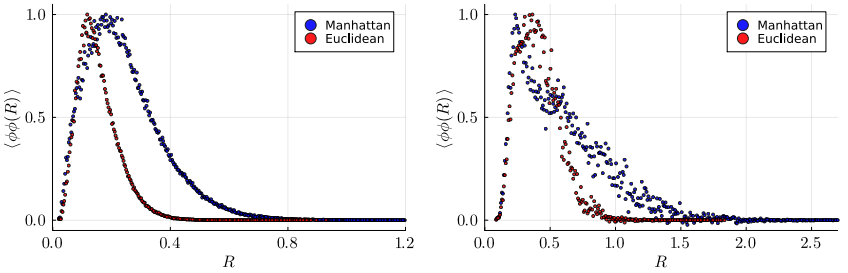

(a) $\alpha = 0.63$ (b) $\alpha = 0.64$

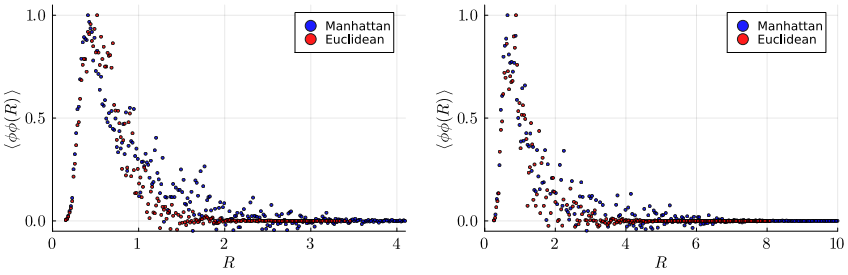

(c) $\alpha = 0.65$ (d) $\alpha = 0.66$

Figure D.2: Relational correlation function $\langle\phi\phi(R)\rangle$, for different values of α. $M = 5.0$ and lattice size $N_1 = 81$.

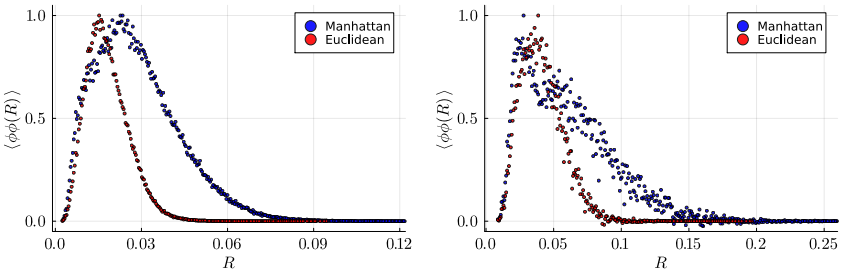

(a) $\alpha = 0.63$ (b) $\alpha = 0.64$

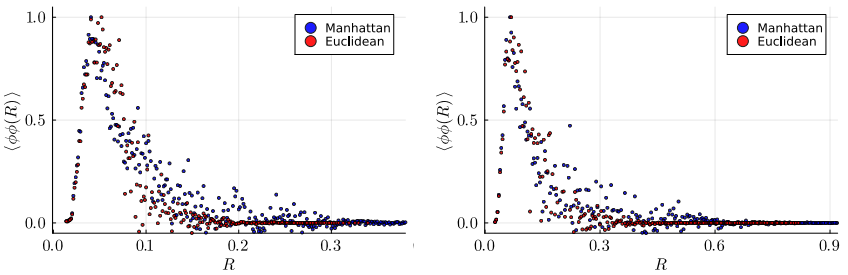

(c) $\alpha = 0.65$ (d) $\alpha = 0.66$

Figure D.3: Relational correlation function $\langle\phi\phi(R)\rangle$, for different values of α. $M = 50.0$ and lattice size $N_1 = 81$.

D.2 Lattice size $N_2 = 256$

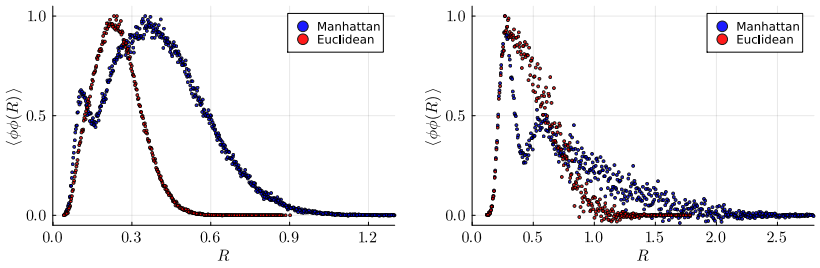

(a) $\alpha = 0.63$ (b) $\alpha = 0.64$

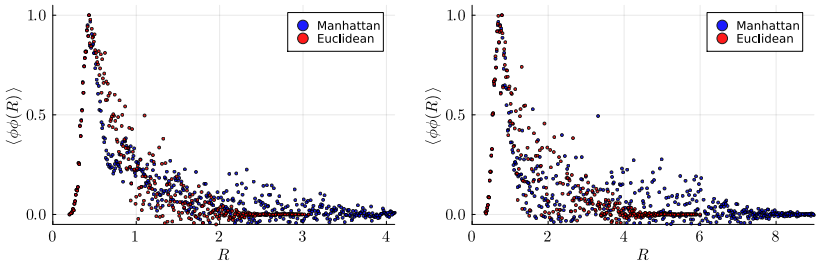

(c) $\alpha = 0.65$ (d) $\alpha = 0.66$

Figure D.4: Relational correlation function $\langle\phi\phi(R)\rangle$, for different values of α. $M = 5.0$ and lattice size $N_2 = 256$.

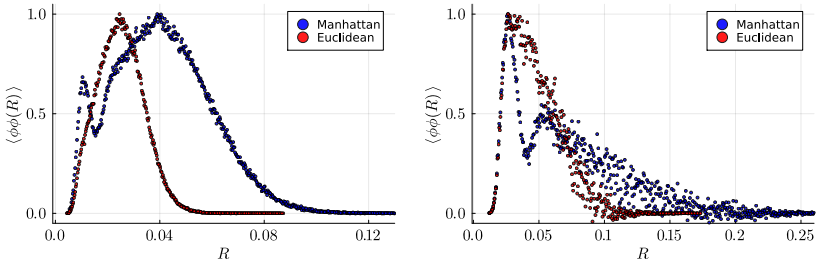

(a) $\alpha = 0.63$ (b) $\alpha = 0.64$

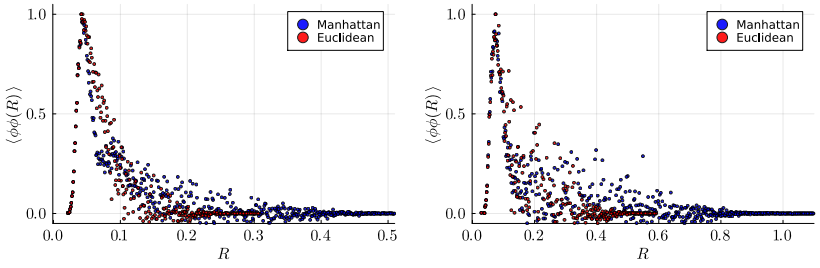

(c) $\alpha = 0.65$ (d) $\alpha = 0.66$

Figure D.5: Relational correlation function $\langle\phi\phi(R)\rangle$, for different values of α. $M = 50.0$ and lattice size $N_2 = 256$.

D.3 Lattice size $N_3 = 625$

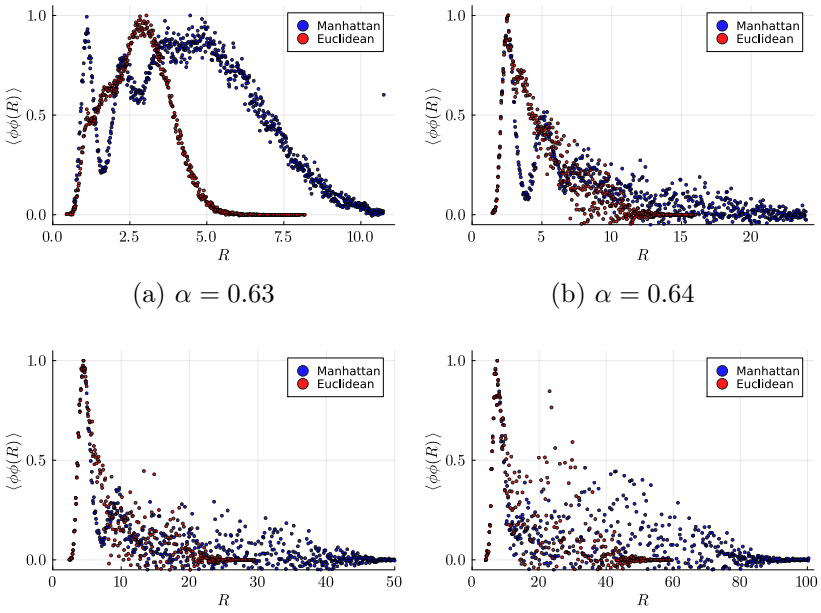

(a) $\alpha = 0.63$ (b) $\alpha = 0.64$

(c) $\alpha = 0.65$ (d) $\alpha = 0.66$

Figure D.6: Relational correlation function $\langle\phi\phi(R)\rangle$, for different values of α. $M = 0.5$ and lattice size $N_3 = 625$.

Bibliography

[1] C. Kiefer. "Quantum gravity: general introduction and recent developments". In: *Annalen der Physik* 15.1-2 (2005), pp. 129–148 (cit. on p. 1).

[2] S. D. Mathur. "The information paradox: a pedagogical introduction". In: *Classical and Quantum Gravity* 26.22 (2009), p. 224001 (cit. on p. 1).

[3] N. Arkani-Hamed, S. Dimopoulos, and G. Dvali. "The hierarchy problem and new dimensions at a millimeter". In: *Phys. Lett. B* 429 (1998), pp. 263–272 (cit. on p. 2).

[4] S. Weinberg. "The cosmological constant problem". In: *Rev. Mod. Phys.* 61.1 (1989), p. 1 (cit. on p. 2).

[5] K. G. Wilson. "The renormalization group: Critical phenomena and the Kondo problem". In: *Rev. Mod. Phys.* 47 (1975), p. 773 (cit. on p. 2).

[6] A. Eichhorn. *Status update: asymptotically safe gravity-matter systems.* preprint arxiv:2201.11543. 2022 (cit. on p. 2).

[7] P. Donà, A. Eichhorn, and R. Percacci. "Matter matters in asymptotically safe quantum gravity". In: *Physical Review D* 89.8 (2014), p. 084035 (cit. on pp. 2, 51).

[8] D. Oriti, ed. *Approaches to Quantum Gravity: Toward a New Understanding of Space, Time and Matter*. Cambridge University Press, 2009 (cit. on p. 2).

[9] J. F. Plebanski. "On the separation of Einsteinian substructures". In: *J. Math. Phys.* 18 (1977), pp. 2511–2520 (cit. on pp. 2, 21).

[10] J. C. Baez. "An Introduction to Spin Foam Models of BF Theory and Quantum Gravity". In: *Lect. Notes Phys.* 543 (2000), pp. 25–94 (cit. on pp. 2, 21).

[11] M. Dupuis. *Spin Foam Models for Quantum Gravity and semi-classical limit.* arXiv preprint arXiv:1104.2765. 2011 (cit. on pp. 2, 22).

[12] J. Engle et al. "LQG vertex with finite Immirzi parameter". In: *Nucl. Phys. B* 799 (2008), pp. 136–149 (cit. on pp. 2, 26).

[13] J. Engle, R. Pereira, and C. Rovelli. "Flipped spinfoam vertex and loop gravity". In: *Nuclear Physics B* 798 (2008), pp. 251–290 (cit. on p. 2).

[14] L. Freidel and K. Krasnov. "A New Spin Foam Model for 4d Gravity". In: *Class. Quant. Grav.* 25 (2008), p. 125018 (cit. on pp. 2, 26, 31).

[15] E. R. Livine. "Projected spin networks for Lorentz connection: linking spin foams and loop gravity". In: *Class. Quantum Grav.* 19 (2002), p. 5525 (cit. on p. 2).

[16] C. Rovelli and S. Speziale. "Lorentz covariance of loop quantum gravity". In: *Phys. Rev. D* 83 (2011), p. 104029 (cit. on p. 2).

[17] J. W. Barrett et al. "Asymptotic analysis of the EPRL four-simplex amplitude". In: *J. Math. Phys.* 50 (2009), p. 112504 (cit. on pp. 2, 38, 43).

[18] J. W. Barrett et al. "Lorentzian spin foam amplitudes: graphical calculus and asymptotics". In: *Class. Quantum Grav.* 27 (2010), p. 165009 (cit. on pp. 2, 38).

[19] P. Donà et al. "SU(2) graph invariants, Regge actions and polytopes". In: *Class. Quant. Grav.* 35.4 (2018), p. 045011 (cit. on pp. 3, 38).

[20] P. Donà et al. "Numerical study of the Lorentzian Engle-Pereira-Rovelli-Livine spin foam amplitude". In: *Phys. Rev. D* 100.10 (2019), p. 106003 (cit. on pp. 3, 38).

[21] F. Gozzini. "A high-performance code for EPRL spin foam amplitudes". In: *Class. Quant. Grav.* 38.22 (2021), p. 225010 (cit. on pp. 3, 38).

[22] L. Smolin. "The Plebanski action extended to a unification of gravity and Yang-Mills theory". In: *Phys. Rev. D* 80 (2009), p. 124017 (cit. on pp. 3, 50).

[23] J. D. Brown and K. V. Kuchar. "Dust as a standard of space and time in canonical quantum gravity". In: *Phys. Rev. D* 51 (1995), pp. 5600–5629 (cit. on pp. 3, 50).

[24] M. Domagala et al. "Gravity quantized: Loop Quantum Gravity with a Scalar Field". In: *Phys. Rev. D* 82 (2010), p. 104038 (cit. on pp. 3, 50).

[25] V. Husain and T. Pawlowski. "Time and a physical Hamiltonian for quantum gravity". In: *Phys. Rev. Lett.* 108 (2012), p. 141301 (cit. on pp. 3, 50).

[26] M. Han and H. Liu. "Semiclassical limit of new path integral formulation from reduced phase space loop quantum gravity". In: *Phys. Rev. D* 102.2 (2020), p. 024083 (cit. on pp. 3, 50).

[27] D. Oriti and H. Pfeifer. "A Spin foam model for pure gauge theory coupled to quantum gravity". In: *Phys. Rev. D* 66 (2002), p. 124010 (cit. on pp. 3, 5, 50, 51).

[28] A. Miković. "Spin foam models of matter coupled to gravity". In: *Class. Quant. Grav.* 19 (2002), pp. 2335–2354 (cit. on pp. 3, 5, 50).

[29] A. R. Mikovic. "Spin foam models of Yang-Mills theory coupled to gravity". In: *Class. Quant. Grav.* 20 (2003), pp. 239–246 (cit. on pp. 3, 50).

[30] S. Speziale. "Coupling gauge theory to spinfoam 3d quantum gravity". In: *Class. Quant. Grav.* 24 (2007), pp. 5139–5160 (cit. on pp. 3, 5, 50).

[31] E. Bianchi et al. "Spinfoam fermions". In: *Class. Quant. Grav.* 30 (2013), p. 235023 (cit. on pp. 3, 5, 50).

[32] M. Han and C. Rovelli. "Spin-foam Fermions: PCT Symmetry, Dirac Determinant, and Correlation Functions". In: *Class. Quant. Grav.* 30 (2013), p. 075007 (cit. on pp. 3, 50).

[33] M. Kisielowski and J. Lewandowski. "Spin-foam model for gravity coupled to massless scalar field". In: *Class. Quant. Grav.* 36.7 (2019), p. 075006 (cit. on pp. 3, 5, 50).

[34] B. Bahr and S. Steinhaus. "Investigation of the Spinfoam Path integral with Quantum Cuboid Intertwiners". In: *Phys. Rev. D* 93.10 (2016), p. 104029 (cit. on pp. 3, 38, 39, 42, 44, 48, 103).

[35] A. Maas. *Lecture on Lattice Quantum Field Theory*. KFU Graz. 2020 (cit. on pp. 3, 5).

[36] M. Ali and S. Steinhaus. "Toward matter dynamics in spin foam quantum gravity". In: *Phys. Rev. D* 106 (2022).
https://github.com/amoosam/CuboidSpinfoamScalarField
Dataset archived at https://doi.org/10.5281/zenodo.6838756 (cit. on pp. 3, 18, 39, 52, 54, 57–60, 63, 64, 67, 78, 81, 83, 104, 105).

[37] G. Calcagni, D. Oriti, and J. Thurigen. "Laplacians on discrete and quantum geometries". In: *Class. Quant. Grav.* 30 (2013), p. 125006 (cit. on pp. 3, 7, 10).

[38] J. Thurigen. "Discrete quantum geometries and their effective dimension". PhD thesis. Humboldt U., 2015 (cit. on pp. 3, 10).

[39] J. Tambornino. "Relational observables in gravity: a review". In: *SIGMA. Symmetry, Integrability and Geometry: Methods and Applications* 8 (2012), p. 017 (cit. on pp. 4, 7).

[40] J. Ambjørn et al. "Nonperturbative quantum gravity". In: *Physics Reports* 519.4-5 (2012), pp. 127–210 (cit. on pp. 4, 51, 56).

[41] B. Dittrich. "Partial and Complete Observables for Canonical General Relativity". In: *Class. Quantum Grav.* 23 (2006), p. 6155 (cit. on pp. 4, 7, 56).

[42] C. Rovelli. "Partial observables". In: *Phys. Rev. D* 65 (2002), p. 124013 (cit. on pp. 4, 7, 55).

[43] N. Metropolis and S. Ulam. "The Monte Carlo Method". In: *Journal of the American Statistical Association* 44.247 (1949), pp. 335–341 (cit. on pp. 4, 58).

[44] M. Creutz. *Quarks, gluons and lattices*. Cambridge University Press, 1983 (cit. on p. 5).

[45] M. Srednicki. *Quantum Field Theory*. Santa Barbara, CA: University of California, Santa Barbara, 2007 (cit. on p. 6).

[46] W. Kamiński, M. Kisielowski, and J. Lewandowski. "Spin-foams for all loop quantum gravity". In: *Classical and Quantum Gravity* 27.9 (2010), p. 095006 (cit. on p. 9).

[47] J. C. Baez and J. P. Muniain. *Gauge fields, knots and gravity*. Vol. 4. World Scientific Publishing Company, 1994 (cit. on p. 9).

[48] M. Desbrun et al. "Discrete Exterior Calculus". In: *Foundations of Computational Mathematics* 6.3 (2005), pp. 325–392 (cit. on pp. 10, 11, 14).

[49] D. Kozlov. *Combinatorial Algebraic Topology*. Berlin: Springer, 2008 (cit. on pp. 10, 11).

[50] M. Nakahara. *Geometry, Topology, and Physics*. London: Taylor and Francis, 2003 (cit. on p. 12).

[51] A. N. Hirani. *Discrete exterior calculus*. California Institute of Technology, 2003 (cit. on p. 14).

[52] A. Perez. "The Spin Foam Approach to Quantum Gravity". In: *Living Reviews in Relativity* 16.3 (2013) (cit. on pp. 20, 21, 30, 32).

[53] T. Thiemann. *Modern Canonical Quantum General Relativity*. Cambridge Monographs on Mathematical Physics. Cambridge University Press, 2007, pp. 141–156 (cit. on p. 20).

[54] E. R. Livine and S. Speziale. "Solving the simplicity constraints for spinfoam quantum gravity". In: *Europhysics Letters* 81.5 (2008), p. 50004 (cit. on p. 21).

[55] S. Holst. "Barbero's Hamiltonian derived from a generalized Hilbert-Palatini action". In: *Physical Review D* 53.10 (1996), p. 5966 (cit. on p. 21).

[56] E. Bianchi, F. Hellmann, et al. "The construction of spin foam vertex amplitudes". In: *SIGMA. Symmetry, Integrability and Geometry: Methods and Applications* 9 (2013), p. 008 (cit. on p. 21).

[57] E. R. Livine. "Spinfoam models for quantum gravity: Overview". In: *arXiv preprint arXiv:2403.09364* (2024) (cit. on p. 21).

[58] K. Krasnov. *Formulations of general relativity: Gravity, spinors and differential forms*. Cambridge University Press, 2020 (cit. on p. 22).

[59] M. Celada, D. González, and M. Montesinos. "BF gravity". In: *Classical and Quantum Gravity* 33.21 (2016), p. 213001 (cit. on p. 22).

[60] L. Freidel, S. Speziale, et al. "On the relations between gravity and BF theories". In: *SIGMA. Symmetry, Integrability and Geometry: Methods and Applications* 8 (2012), p. 032 (cit. on p. 22).

[61] S. Alexandrov and P. Roche. "Critical overview of loops and foams". In: *Physics reports* 506.3-4 (2011), pp. 41–86 (cit. on p. 22).

[62] V. Bonzom and E. R. Livine. "Lagrangian approach to the Barrett-Crane spin foam model". In: *Physical Review D—Particles, Fields, Gravitation, and Cosmology* 79.6 (2009), p. 064034 (cit. on p. 22).

[63] C. P. Rourke and B. J. Sanderson. *Introduction to piecewise-linear topology*. Springer Science & Business Media, 2012 (cit. on p. 23).

[64] A. A. Mele. "Introduction to Haar measure tools in quantum information: A beginner's tutorial". In: *Quantum* 8 (2024), p. 1340 (cit. on pp. 24, 106).

[65] R. Oeckl. *Discrete gauge theory: From lattices to TQFT*. Imperial College Press, 2005 (cit. on p. 25).

[66] P. Martin-Dussaud. "A primer of group theory for loop quantum gravity and spin-foams". In: *General Relativity and Gravitation* 51 (2019), pp. 1–70 (cit. on pp. 28, 107).

[67] I. Mäkinen. "Introduction to SU (2) recoupling theory and graphical methods for loop quantum gravity". In: *arXiv preprint arXiv:1910.06821* (2019) (cit. on pp. 28, 107).

[68] A. M. Perelomov. "Coherent states for arbitrary Lie group". In: *Communications in Mathematical Physics* 26 (1972), pp. 222–236 (cit. on p. 33).

[69] E. R. Livine and S. Speziale. "New spinfoam vertex for quantum gravity". In: *Physical Review D—Particles, Fields, Gravitation, and Cosmology* 76.8 (2007), p. 084028 (cit. on pp. 34, 35, 39, 40).

[70] H. Minkowski. "Allgemeine Lehrsätze über die convexen Polyeder". In: *Nachrichten von der Gesellschaft der Wissenschaften zu Göttingen, Mathematisch-Physikalische Klasse* 1897 (1897), pp. 198–220 (cit. on p. 35).

[71] C. Allen, F. Girelli, and S. Steinhaus. "Numerical evaluation of spin foam amplitudes beyond simplices". In: *Physical Review D* 105.6 (2022), p. 066003 (cit. on pp. 37, 39).

[72] B. Bahr, S. Klöser, and G. Rabuffo. "Towards a cosmological subsector of spin foam quantum gravity". In: *Physical Review D* 96.8 (2017), p. 086009 (cit. on pp. 38, 39).

[73] B. Bahr and S. Steinhaus. "Hypercuboidal renormalization in spin foam quantum gravity". In: *Physical Review D* 95.12 (2017), p. 126006 (cit. on pp. 38, 39, 42, 48).

[74] C. Rovelli and L. Smolin. “Discreteness of the area and volume in quantum gravity”. In: *Nucl. Phys. B* 442 (1995), pp. 593–734 (cit. on p. 38).

[75] T. Regge. “General relativity without coordinates”. In: *Il Nuovo Cimento (1955-1965)* 19 (1961), pp. 558–571 (cit. on p. 38).

[76] M. Vojinović. “Cosine problem in EPRL/FK spinfoam model”. In: *General Relativity and Gravitation* 46 (2014), pp. 1–35 (cit. on p. 38).

[77] F. Conrady and L. Freidel. “Semiclassical limit of 4-dimensional spin foam models”. In: *Physical Review D—Particles, Fields, Gravitation, and Cosmology* 78.10 (2008), p. 104023 (cit. on p. 38).

[78] V. Bonzom. “Spin foam models for quantum gravity from lattice path integrals”. In: *Physical Review D—Particles, Fields, Gravitation, and Cosmology* 80.6 (2009), p. 064028 (cit. on p. 38).

[79] F. Hellmann and W. Kaminski. “Holonomy spin foam models: Asymptotic geometry of the partition function”. In: *Journal of High Energy Physics* 2013.10 (2013), pp. 1–63 (cit. on p. 38).

[80] J. R. Oliveira. “EPRL/FK asymptotics and the flatness problem”. In: *Classical and Quantum Gravity* 35.9 (2018), p. 095003 (cit. on p. 38).

[81] F. Conrady and L. Freidel. “Quantum geometry from phase space reduction”. In: *Journal of mathematical physics* 50.12 (2009) (cit. on p. 40).

[82] M. Han and M. Zhang. “Asymptotics of Spinfoam Amplitude on Simplicial Manifold: Lorentzian Theory”. In: *Class. Quant. Grav.* 30 (2013), p. 165012 (cit. on p. 43).

[83] A. Ashtekar, M. Campiglia, and A. Henderson. “Casting loop quantum cosmology in the spin foam paradigm”. In: *Classical and Quantum Gravity* 27.13 (2010), p. 135020 (cit. on p. 50).

[84] A. Henderson et al. “Local spinfoam expansion in loop quantum cosmology”. In: *Classical and Quantum Gravity* 28.2 (2010), p. 025003 (cit. on p. 50).

[85] M. Niedermaier. “The asymptotic safety scenario in quantum gravity: an introduction”. In: *Classical and Quantum Gravity* 24.18 (2007), R171 (cit. on p. 51).

[86] A. Eichhorn and A. Held. “Towards implications of asymptotically safe gravity for particle physics”. In: *arXiv preprint arXiv:1907.05330* (2019) (cit. on p. 51).

[87] J. Ambjørn et al. “Matter-driven change of spacetime topology”. In: *Physical Review Letters* 127.16 (2021), p. 161301 (cit. on p. 51).

[88] J. Ambjorn et al. "Scalar fields in causal dynamical triangulations". In: *Classical and Quantum Gravity* 38.19 (2021), p. 195030 (cit. on p. 51).

[89] J. W. Barrett and L. Crane. "Relativistic spin networks and quantum gravity". In: *Journal of Mathematical Physics* 39.6 (1998), pp. 3296–3302 (cit. on p. 51).

[90] P. Dirac. *Lectures on Quantum Mechanics*. Vol. 2. Belfer Graduate School of Science Monographs Series. New York: Belfer Graduate School of Science, 1967 (cit. on p. 56).

[91] W. K. Hastings. "Monte Carlo sampling methods using Markov chains and their applications". In: (1970) (cit. on p. 58).

[92] P. Donà and P. Frisoni. "Summing bulk quantum numbers with Monte Carlo in spin foam theories". In: *Physical Review D* 107.10 (2023), p. 106008 (cit. on pp. 80, 104).

[93] S. Steinhaus. "Monte Carlo algorithm for spin foam intertwiners". In: *Physical Review D* 110.2 (2024), p. 026022 (cit. on pp. 80, 104).